UNIVERSIDADE
BEIRA INTERIOR

CFD Analysis of Alcohol-to-Jet Fuel Combustion in a CFM56-3 Combustor

Rafael Valente Fernandes

Dissertação para obtenção do Grau de Mestre em
Engenharia Aeronáutica
(Mestrado Integrado)

Orientador: Prof. Doutor Francisco Miguel Ribeiro Proença Brójo

Fevereiro de 2025

Declaração de Integridade

Eu, Rafael Valente Fernandes, que abaixo assino, estudante com o número de inscrição a43421 do Mestrado Integrado em Engenharia Aeronáutica da Faculdade de Engenharia, declaro ter desenvolvido o presente trabalho e elaborado o presente texto em total consonância com o **Código de Integridades da Universidade da Beira Interior**.

Mais concretamente afirmo não ter incorrido em qualquer das variedades de Fraude Académica, e que aqui declaro conhecer, que em particular atendi à exigida referenciação de frases, extratos, imagens e outras formas de trabalho intelectual, e assumindo assim na íntegra as responsabilidades da autoria.

Universidade da Beira Interior, Covilhã 18/02/2025

Rafael Valente Fernandes

To my beloved parents, Paulinha and Óscar,
and my dear sister, Lara,
who have always believed in me.

Acknowledgements

I would like to express my sincere appreciation to everyone who supported me throughout this challenging journey and helped me complete my master's thesis. First, I am deeply grateful to my supervisor, Professor Francisco Brójo, whose guidance, insightful advice, and valuable suggestions made this endeavour not only possible but also more manageable. His constant availability for discussions and the resources he provided for the simulations in this project were essential to the successful completion of this study.

Even though he was not my supervisor, Rafael Domingues provided invaluable support, often acting as one. He was always available to help me navigate the challenges of CFD analysis and answer all my doubts about it. His generosity in providing both the geometry and access to the computer cluster significantly accelerated the development of this project. For that, I will always be thankful.

I would not have made it this far without the support of the friends I met over these past five years. I especially want to thank Miguel, Erika, Rafael and Vasco, whose friendship, laughter, and shared moments often gave me the motivation to keep going. A special thanks goes to Rafael, RR, whose insights and expertise in LaTeX were essential in making this work look as clean and professional as possible.

Above all, I extend my deepest gratitude to my parents and my sister, who stood by me during my most difficult times. Their unwavering support, encouragement, patience, love, and strength were fundamental in helping me achieve this goal. Thank you!

Resumo

A forte dependência de combustíveis fósseis no sector da aviação contribui significativamente para as emissões poluentes, agravando o aquecimento global e degradando a qualidade do ar, o que torna urgente a necessidade de alternativas sustentáveis. Uma solução promissora é a utilização de combustíveis de aviação sustentáveis (SAF), que oferecem uma alternativa viável ao combustível para aviação convencional. Entre eles, o *Alcohol-to-Jet Synthetic Paraffinic Kerosene* (ATJ-SPK), um combustível de origem biológica, demonstrou potencial para reduzir o impacto ambiental da aviação. Este estudo apresenta uma análise de Dinâmica de Fluidos Computacional (CFD) da combustão do ATJ-SPK num combustor CFM56-3, utilizando o ANSYS Fluent, aplicando o modelo de tensões de Reynolds (RSM) como modelo viscoso. A investigação foca-se na comparação das emissões do ATJ-SPK com as do combustível Jet A convencional, ao mesmo tempo que avalia a viabilidade do ATJ-SPK como um substituto imediato. A análise foi realizada para os diferentes regimes de potência do ciclo de aterragem e descolagem (LTO) da ICAO, avaliando as principais caraterísticas de combustão, tais como a distribuição da temperatura, as emissões e a eficiência.

Os resultados indicam que o ATJ-SPK apresenta um comportamento na combustão semelhante ao do Jet A, demonstrando o seu potencial como combustível alternativo sustentável. Nomeadamente, as emissões de NOx registam uma redução em todos os regimes de potência, particularmente na potência máxima, o que sugere benefícios para o ambiente. As emissões de CO, no entanto, requerem validação adicional devido a tendências inconclusivas. Importa salientar que os resultados da simulação apresentam uma boa concordância com os dados experimentais, especialmente em parâmetros importantes como a temperatura de saída, reforçando a fiabilidade da abordagem CFD. Estes resultados sustentam a viabilidade do ATJ-SPK como substituto do combustível para aviação convencional, contribuindo para a transição do setor da aviação para a sustentabilidade.

Palavras-chave

Combustíveis de aviação sustentáveis, *Alcohol-to-Jet*, Análise CFD, CFM56-3, Emissões, *ANSYS Fluent*, Combustor

Abstract

The aviation industry's heavy reliance on fossil fuels significantly contributes to polluting emissions, exacerbating global warming and degrading air quality, prompting the urgent need for sustainable alternatives. One promising solution is the use of Sustainable Aviation Fuels (SAFs), which offer a viable alternative to conventional jet fuel. Among them, Alcohol-to-Jet Synthetic Paraffinic Kerosene (ATJ-SPK), a bio-derived fuel, has shown potential to reduce aviation's environmental impact. This study presents a Computational Fluid Dynamics (CFD) analysis of ATJ-SPK combustion in a CFM56-3 combustor using ANSYS Fluent, employing the Reynolds Stress Model (RSM) as the viscous model. The research focuses on comparing the emissions of ATJ-SPK with those of conventional Jet A fuel while assessing ATJ-SPK's viability as a drop-in replacement. The analysis was conducted across the power settings of the ICAO Landing and Take-Off (LTO) cycle, evaluating key combustion characteristics such as temperature distribution, emissions, and efficiency.

Results indicate that ATJ-SPK exhibits similar combustion behaviour to Jet A, demonstrating its potential as a sustainable alternative fuel. Notably, NOx emissions show a reduction across all power settings, particularly at full power, suggesting environmental benefits. CO emissions, however, require further validation due to inconclusive trends. Importantly, the simulation results align well with experimental data, particularly in key parameters like outlet temperature, reinforcing the reliability of the CFD approach. These findings support the feasibility of ATJ-SPK as a viable replacement for conventional jet fuel, contributing to aviation's transition toward sustainability.

Keywords

Sustainable aviation fuels, Alcohol-to-Jet, CFD analysis, CFM56-3, Emissions, ANSYS Fluent, Combustor

Contents

List of Figures

List of Tables

List of Acronyms

APU Auxiliary Power Unit

ASTM American Society for Testing and Materials

ATJ-SPK Alcohol-to-Jet Synthetic Paraffinic Kerosene

CAAFI Commercial Aviation Alternative Fuels Initiative

CAD Computer-Aided Design

CFD Computational Fluid Dynamics

CH-SK Catalytic-Hydrothermolysis-Synthesized Kerosene

CORSIA Carbon Offsetting and Reduction Scheme for International Aviation

CTL coal-to-liquid

DNS Direct Numerical Simulation

EIs emission indexes

ERF Effective Radiative Forcing

EVM Eddy Viscosity Models

FAME Fatty Acid Methyl Ester

FT-SPK Fischer–Tropsch Synthetic Paraffinic Kerosene

FT-SPK/A Fischer–Tropsch Synthetic Paraffinic Kerosene with Aromatics

GHG Greenhouse Gas

GTE Gas Turbine Engine

GTL gas-to-liquid

HEFA-SPK Hydroprocessed Esters and Fatty Acids Synthetic Paraffinic Kerosene

HFS-SIP Hydroprocessed Fermented Sugars to Synthetic Isoparaffins

HHC-SPK Hydroprocessed Hydrocarbons Esters and Fatty Acids Synthetic Paraffinic Kerosene

HHV higher heating value

HPC high pressure compressor

HPT high pressure turbine

IATA International Air Transport Association

ICAO International Civil Aviation Organization

ICE four-stroke internal combustion engine

LES Large Eddy Simulation

LHV lower heating value

LPC low pressure compressor

LPT low pressure turbine

LTO Landing and Take-off

NASA National Aeronautics and Space Administration

PDF Probability Density Function

PM Particulate Matter

RAM random access memory

RANS Reynolds Average Navier-Stokes

RSM Reynolds Stress Models

SAF Sustainable Aviation Fuel

SAFUG Sustainable Aviation Fuel Users Group

SAK Synthetic Aromatic Kerosene

SRS Scale-Resolving Simulation

TBC Thermal barrier coating

UHC unburned hydrocarbons

Nomenclature

Roman Symbols

$\bar{h}_i$	Absolute enthalpy of a substance i	$[\mathrm{J\,mol^{-1}}]$
Δh_c	Heat of combustion or heating value	$[\mathrm{MJ\,kg^{-1}}]$
ΔH_R	Enthalpy of combustion (or reaction)	$[\mathrm{J}]$
Δh_R	Specific enthalpy of combustion (or reaction)	$[\mathrm{J\,mol^{-1}}]$
$\Delta h^0_{f,i}$	Enthalpy of formation (or heat of formation) of a substance i	$[\mathrm{J\,mol^{-1}}]$
$\Delta h_{s,i}$	Sensible enthalpy change of a substance i	$[\mathrm{J\,mol^{-1}}]$
$\dot{m}$	Mass flow rate	$[\mathrm{kg\,s^{-1}}]$
$\dot{Q}$	Heat release rate	$[\mathrm{W}]$
A/F	Air-to-fuel ratio	
F/A	Fuel-to-air ratio	
A	Area	$[\mathrm{m^2}]$
c_p	Molar heat capacity at constant pressure	$[\mathrm{J\,mol^{-1}\,K^{-1}}]$
D_p	Mass of gaseous pollutant emitted	$[\mathrm{g}]$
F	Engine thrust	$[\mathrm{kN}]$
F_s	Specific thrust	$[\mathrm{kN\,s\,kg^{-1}}]$
F_{00}	Rated thrust	$[\mathrm{kN}]$
H	Enthalpy	$[\mathrm{J}]$
h	Specific enthalpy	$[\mathrm{J\,mol^{-1}}]$
LHV	Lower heating value	$[\mathrm{MJ\,kg^{-1}}]$
M	Molecular weight	$[\mathrm{kg\,mol^{-1}}]$
m	Mass	$[\mathrm{kg}]$
P	Pressure	$[\mathrm{Pa}]$
r_p	Pressure ratio	
T	Temperature	$[\mathrm{K}]$

T_{ad}	Adiabatic flame temperature	[K]
$TSFC$	Thrust specific fuel consumption	$[\mathrm{g\,kN^{-1}\,s^{-1}}]$
U	Compressor outlet velocity	$[\mathrm{m\,s^{-1}}]$
V	Volume	$[\mathrm{m^3}]$
v	Velocity	$[\mathrm{m\,s^{-1}}]$

Greek Symbols

Δ	Variation of the parameter	
η	Efficiency	
η_c	Combustion efficiency	
η_e	Energy conversion efficiency	
η_o	Overall efficiency	
η_p	Propulsion efficiency	
γ	Ratio of specific heats	
ϕ	Equivalence ratio	
π_{00}	Reference pressure ratio	
ρ	Density	$[\mathrm{kg\,m^{-3}}]$
ξ	Mixture fraction	

Subscripts

$1/4$	Value for a quarter section of the combustor
2	Combustor inlet stage
3	Combustor outlet stage
actual	Current value of the parameter
ref	Reference/standard value of the parameter
stoic	Stoichiometric value of the parameter
a	Air; Refers to the inlet conditions
c, jc	Refers to the cold stream
des	Design value of the parameter

f	Fuel; Formation value of substance
h, jh	Refers to the hot stream
i	Element/substance
j	Refers to the jet stream
max	Maximum value of the parameter
mr	Maximum circumferential mean value of the parameter
$prod$	Products
r	Circumferential mean value of the parameter
$reac$	Reactants
s	Indicates the term of sensible enthalpy change

Superscripts

0	Refers to substance in standard state

Chapter 1

Introduction

1.1 Motivation

The aviation industry has contributed to climate change more than it would be desirable, especially concerning global warming. The drastic increase of this industry over the last decades, from 310 million in 1970 to 4.3 billion passenger journeys in 2018, is the root of this problem [1]. This trend is expected to continue with a near-doubling of activity between now and 2035, as the International Air Transport Association (IATA) anticipates [2]. The aviation contribution is projected to reach a total of 0.1°C of warming by 2050, half of it already attained, and the other half over the next three decades, if a 3% annual growth in this sector continues [1].

The emissions resulting from the Gas Turbine Engine (GTE) present in the aircraft are the source of this problem. These emissions can be categorized into the CO_2 and the non-CO_2 type, where in the latter, nitrogen oxides (NO_x), water vapour (H_2O), sulphur dioxide (SO_2) and soot are included. To put it into perspective, between 2016 and 2019, aircraft engines were burning more than 1 billion litres of fuel per day, which emit, per kg of fuel, 3.16 kg of CO_2, 1.23 kg of H_2O, 15.14 g of NO_x, 1.2 g of SO_2 and 0.03 g of soot [1]. Regarding all of the worldwide anthropogenic carbon emissions, i.e., CO_2 emissions, aviation alone is responsible for approximately 2% or 12% if only the transportation carbon emissions are considered [3]. However, a more accurate analysis of the impact on surface warming can be made if the Effective Radiative Forcing (ERF) is calculated, because in this case the total impact is taken into account and not only the effect of the Greenhouse Gas (GHG) emissions. With this said, global aviation is estimated to be responsible for 3.5% of global warming [4].

Despite what most might think, in this industry sector, CO_2 is not the main responsible for this warming effect. In fact, non-CO_2 effects account for 66% of the warming [4]. In these non-CO_2 effects, the NO_x-driven changes in the chemical composition of the atmosphere and the contrail formations can be highlighted as the main responsible [5]. The mentioned chemical changes are due to NO_x altering the radiative balance of other gases like methane (CH_4), ozone (O_3) and stratospheric water (H_2O) [1]. In turn, the water vapour and soot emissions, that can result in contrail formation [5], are also a source of warming because they can lead to cirrus clouds that reflect and absorb radiation [1].

Taking into account all of the above and in alignment with the Paris Agreement goal for global warming not to exceed 1.5°C, the IATA 77^{th} Annual General Meeting approved a resolution for the global air transport industry to achieve net-zero carbon emissions by 2050 [6]. This will be a big challenge for the aviation industry because it must reconcile emissions reduction with the constant growth in flying demand [6]. For this to be accomplished, in 2050, with 10 billion people expected to fly that year, at least 1.8 gigatons of carbon must be abated, however, the net-zero commitment also implies that a cumulative total of 21.2 gigatons of carbon will be abated between now and 2050 [6]. An important and immediate measure is the International Civil Aviation Organization (ICAO) Carbon Offsetting and Reduction Scheme for International Aviation (CORSIA) which limits net CO_2 aviation emissions at 2020 levels until 2035 [3, 6].

ICAO has been taking measures to address aviation's environmental impacts, e.g., a global CO_2 standard to regulate fuel efficiency for new aircraft since 2020 and an ambitious goal of a 2% annual fuel efficiency improvement [2]. However, these improvements in fuel efficiency, from 4.4 L/100 passenger-km in 2005 to 3.4 in 2017 in Europe (-24%), are not enough to cover the sector's rapid growth, so some alternative options have emerged [2]. These can be new propulsion options, e.g., electric and hybrid systems, or new types of jet fuels, e.g., liquid natural gas and hydrogen. Still, they present several unsolved technical problems and have been only tested at a small-scale [2]. When it comes to electric-powered aircraft, a breakthrough in battery chemistry is needed to overcome the one order of magnitude lower volumetric and mass energy densities compared to the fossil kerosene's energy density. This means that only small full-electric aircraft will likely be commercialized soon since the requirements for medium and long-haul flights (weight, seat capacity, speed and range) cannot be satisfied [7]. On the other hand, despite being a very appealing fuel due to its renewable and clean energy sources with carbon capture and storage, hydrogen probably presents the bigger challenges to defeat. The low volumetric energy density of hydrogen requires highly insulated tanks capable of storing it in liquid form. Its use in medium and long-haul flights demands a deep redesign of not only the aircraft engines and airframes but also the fuel supply chain (on-the-ground storage and refuelling), forcing it to be a long-term solution [7].

While other technologies evolve, the answer to decarbonisation in aviation as an immediate measure seems to be drop-in Sustainable Aviation Fuel (SAF) [2]. This solution presents several advantages: aircraft airframe, engine and refuelling infrastructure compatibility [3, 7]; compared with the conventional Jet A, 100% SAF has the potential to reduce GHG emissions by up to 94% [3], due to the CO_2 uptake of biomass feedstocks during photosynthesis [2]; and more flexibility of feedstocks and production technologies [3]. Despite still being produced in low volumes for use in commercial flights [7], as of January 2022, seven production pathways for this kind of fuel had already been approved by American Society for Testing and Materials (ASTM) [8]. Investing in the production of SAF will increase supply and reduce costs, making the net zero an achievable reality by 2050 [6].

1.2 Main Goals

The main focus of this work is to compare the combustion of SAFs and Jet A fuel in a CFM56-3 combustor during ICAO's Landing and Take-off (LTO) cycle. This will be done through a numerical analysis in a Computational Fluid Dynamics (CFD) software, in this case, ANSYS Fluent. The geometry of the CFM56-3 combustor that will be used was developed by de Oliveira [9] during his master's thesis. The selection of the SAFs to be analysed will be discussed later in this thesis considering several aspects. As comparison elements, the pollutants emitted and the performance of the combustion will be analysed. This way, the present work will allow to conclude on the possibility and viability of using unmixed SAF as the main fuel for commercial aviation.

1.3 Thesis Structure

The thesis is divided into five chapters. The present chapter includes the motivation that moved the author to choose this theme and the objectives for this work. It also presents a historical and bibliographical review to give context. In such a manner, the work and experiments done so far are introduced. This chapter was written with the intention of briefly explaining the topic of the thesis to anyone with the minimum scientific knowledge.

The second chapter will give some basic considerations regarding turbofan engines, especially the CFM56-3 engine. There will also be a special focus on the combustor operation and the chemical reactions occurring inside it.

The third chapter will address the properties of the several SAFs and the aspects taken into account to select the ones to be analysed while comparing with the Jet A fuel characteristics.

In the fourth chapter, the whole CFD process will be explained, i.e., the problem set-up, the mesh generation, the boundary conditions applied, the numerical set-up and the combustion model used will be thoroughly detailed.

The fifth chapter will comprise all the results obtained and its consequent discussion

Finally, the sixth chapter will present the conclusions that can be drawn and proposals for future studies.

1.4 Historical Review

Despite only accounting for less than 0.1% of jet kerosene consumption [10], SAF is not a recent technology since studies for developing alternatives to petroleum-based jet fuel started long back. Back then, economic and supply concerns were the main motivators for the research. Still, efforts were only significant when the climate change crisis started to be the biggest concern of the century [10]. This started in 2006 when several aircraft manufacturers, U.S. commercial airlines and the U.S. government established the Commercial Aviation Alternative Fuels Initiative (CAAFI) [11]. Later, other initiatives started, like the Sustainable Aviation Fuel Users Group (SAFUG) in 2008 that gathers commercial airlines and aircraft manufacturers to accelerate the development and commercialization of SAF [11]. In that same year, the first-ever flight test using a blend of conventional jet fuel and biofuel was performed by Virgin Atlantic. This flight connected London to Amsterdam, it was done on a Boeing 747 and the mix of fuel consisted of 80% petro-jet and 20% biofuel made from tropic oils [11].

These concerns with the environmental issues and the initiatives for research led to the first ASTM approved conversion process for SAF production in 2009. It is listed as Annex A1 of D7566[1] and it's called Fischer–Tropsch Synthetic Paraffinic Kerosene (FT-SPK). The blending limit is 50% and the sustainable feedstock options include municipal solid waste, agricultural and forestry residues, algal biomass, and woody energy crops. The Fischer-Tropsch synthesis was developed by Franz Fischer and Hans Tropsch in the 1920s to produce liquid hydrocarbon from coal and is a proven and well-established pathway [10]. This approval allowed, in that year, the first flight carrying passengers. KLM did it on a 50% traditional kerosene and 50% biofuel blend of camelina (oilseed from the mustard family) in one engine. [11, 12]. In the next year, the U.S. Navy did a flight demonstration with the strike fighter F/A-18, named "Green Hornet", on a 50/50 blend of conventional kerosene and camelina-based biofuel. This demonstration was an important milestone in the certification and use of camelina fuels in military aircraft since the aircraft performed as expected in its whole flight envelope, including supersonic speeds [11, 13].

Hydroprocessed Esters and Fatty Acids Synthetic Paraffinic Kerosene (HEFA-SPK) was approved as the second pathway for SAF production by ASTM two years later, in 2011, in a 50% maximum blending ratio. Feedstock options of this process are more limited than the FT-SPK ones because they need to be a triglyceride, usually a solid fat or oil. In this category animal fats (tallow), used cooking oil and oil from algae or plants like camelina and jatropha are included. However, despite this limitation, HEFA-SPK powered over 95% of the SAF flights due to its ease of integration into an oil refinery, since it includes a single additional step [10]. This certification allowed, in that year more than 1,000 flights between Hamburg and Frankfurt made by Lufthansa in a blend that included fuel made of camelina, jatropha and tallow. Alaska Airlines also benefited from this certification by making 75 flights between Seattle and Portland on an 80/20 blend of petroleum-based fuel and biofuel from cooking oil [11].

After this, new pathways for the production of SAFs started to be approved at a faster

---

[1] ASTM D7566 is the Standard Specification for Aviation Turbine Fuel Containing Synthesized Hydrocarbons and it dictates fuel quality standards for non-petroleum-based jet fuel and outlines approved SAF-based fuels and the percent allowable in a blend with Jet A [3].

pace. In 2014, Hydroprocessed Fermented Sugars to Synthetic Isoparaffins (HFS-SIP) was approved and listed as Annex A3 of D7566. This process does not produce synthesized paraffinic kerosene, differently to FT-SPK and HEFA-SPK, and so blending mixtures are limited to a 10% ratio, although some test flights done with a 20% ratio were successful. The main feedstock of this process is sugar cane, however, other cellulose-based sugars are preferred to avoid food-feed-fuel conflicts [10]. One year later, a variation of the FT-SPK was approved by the name Fischer–Tropsch Synthetic Paraffinic Kerosene with Aromatics (FT-SPK/A). The difference is that in this process the end product hydrocarbon has an aromatic content, making it even more compatible with current engines when it comes to fuel leakage avoidance. Despite having a 50% maximum blend ratio, fuels resulting from this process have the most potential of being certified as 100% conventional fuel replacement [10]. The fifth process to be approved was Alcohol-to-Jet Synthetic Paraffinic Kerosene (ATJ-SPK), in 2016, once again, with a maximum blending ratio of 50%. As the name suggests, the fuel is derived from an alcohol. As of now, only isobutanol and ethanol are accepted as feedstocks, though all five carbon alcohols are expected to be certified in the future. These alcohols can be obtained from the typical sugar/starch options, like sugar cane and sugar beet, or, from other more sustainable options, like lignocellulosic biomass and wastes [10]. The most recent pathways approved by ASTM are Catalytic-Hydrothermolysis-Synthesized Kerosene (CH-SK) and Hydroprocessed Hydrocarbons Esters and Fatty Acids Synthetic Paraffinic Kerosene (HHC-SPK), both in 2020. The former is accepted in a maximum blending ratio of 50% and its feedstocks are similar to the HEFA-SPK ones [10]. The latter has two notable features: it was the first process to be approved through the standard specification ”fast track”, which means it's only accepted with a 10% blending ratio, and the oil found in specific algae is the sole feedstock source accepted for this process[10].

After all these certifications, two important test flights can be highlighted because they demonstrate the viability of 100% SAF in commercial flight. The first one occurred in December 2021 and was performed by United Airlines. This was the first-ever flight to be done with 100% SAF in one of the aircraft's engines. It was proved that there are no operational differences in powering an engine with biofuels compared with conventional jet fuel since this aircraft carried the same amount of both fuels on each side. The Boeing 737 MAX 8 flew from Chicago to Washington DC and had more than 100 passengers including several partners of this project, like Boeing, CFM International, Virent and World Energy [14]. The other, more recent, demonstration flight, happened in November 2023 and was held by Virgin Atlantic, as mentioned before, one of the pioneer airlines in the decarbonization of the industry. This flight went further than the one performed by United Airlines because it used 100% SAF in both engines. It was the first commercial airline to fly across the Atlantic, from London to New York, in these conditions. The aircraft was a Boeing 787 equipped with Rolls-Royce Trent 1000 engines fueled with a blend of 88% HEFA-SPK supplied by AirBP and 12% Synthetic Aromatic Kerosene (SAK) supplied by Virent. Since the flight used 100% SAF, there was the need for SAK in this blend, because, as mentioned above, current engines require a percentage of aromatics in the fuel to avoid leakages. This project had the objective of proving that SAF is a safe drop-in fuel replacement, that it is the only mid-term viable solution for decarbonising long-haul aviation and there should be a scale-up in production by investing more in this technology [15].

1.5 Bibliographical Review

Over time, several authors have published their studies regarding either experiments or simulations of the combustion of SAF compared to conventional jet fuel. These studies aimed at analysing emissions, performance and energy conversion of the combustion of some alternative fuels. With this in mind, this section will review the most important literature on this topic.

One of the first to analyse alternative fuels on jet engines was French [16] who conducted an experimental analysis of the SR-30 gas turbine performance run on biodiesel fuels. The two biodiesel fuels were made of new canola oil and used cooking oil. The ignition in the engine was not affected by either of the biofuels and the exhaust jet color and size were visually not different from the Jet A. The results also showed that thrust and angular acceleration with the biodiesel fuels was proportionally less than the Jet A.

Corporan et al. [17] investigated the emissions characteristics of two combustion systems, a T63 turboshaft engine and an atmospheric pressure swirl-stabilized combustor, fueled with conventional military kerosene (JP-8), a Fischer-Tropsch synthetic jet fuel and blends of the two. The goal was to evaluate the impact of the aromatic and sulfur-free FT fuel in the combustion by analysing nonvolatile Particulate Matter (PM) and gaseous emissions. The tests demonstrated that neither neat FT fuel nor its blends had significant impacts on the engine performance, furthermore, no fuel leaks were observed during operation. The FT fuel and the blends proved beneficial since a greater than 90% reduction in PM mass and number and an over 80% reduction in engine smoke number were observed when using it relative to the JP-8. This reduction can be, this way, related to the reduced aromatic content of the alternative fuels studied. Despite the reduction in sulfur oxide and a slight increase in water vapour, a negligible impact on gaseous emissions was detected.

The performance and emission characteristics of a small-scale gas turbine engine running on biofuels were studied by Habib et al. [18]. The biofuels used were soy methyl ester, canola methyl ester, recycled rapeseed methyl ester, hog-fat biofuel aswell as 50% blends with Jet A and they were compared with neat Jet A fuel. Biofuels produced a slightly reduced static thrust and thrust-specific fuel consumption compared to Jet A, however, the numbers are still comparable. On the other hand, pure biofuels significantly increased thermal efficiency compared to Jet A and the blends. Another benefit of using biofuels was a decrease in the CO and NO emission concentrations. These study results suggest that an optimum mix can be achieved to reduce emissions while producing the desired thrust.

Timko et al. [19] conducted an experimental analysis where the NO_x, CO and nonvolatile PM size distribution, number and mass emissions were measured in a CFM56-7 gas turbine engine running on alternatives to petroleum-based fuel. The fuels chosen were a natural gas-derived Fischer-Tropsch synthetic fuel, a 50/50 blend of this synthetic fuel with Jet A and a 20/80 and a 40/60 blend of Fatty Acid Methyl Ester (FAME) with jet fuel due to their low aromatic content and high oxygen content (for FAME blends). Generally, the results were positive since the emissions performance improved or stayed the same when the alternative fuels were used. The neat FT fuel and the two FAME blends combustion allowed a CO reduction. The NO_x emissions were also reduced, 10% with the neat FT fuel and 5% with its blend compared to Jet A. The FAME blends got even better results in this regard, a 29% reduction with the 40/60 blend and 23% with the 20/80 blend. A PM reduction was also achieved with the alternative fuels, however, this reduction declined as the power was increased.

The previous experiment on the CFM56-7B also allowed a more precise PM characterization by Lobo et al. [20]. The engine operated in several power settings, including the ones specified in the ICAO's LTO cycle. This cycle allows an understanding of the effects on the local air quality once it simulates the aircraft engine operations at idle/taxi, approach, climb-out, and take-off. Except for the 20% FAME blend, all the other fuels got smaller or equal PM geometric mean diameter, emphasizing the bigger reduction accomplished by the neat FT fuel and its blend. The alternative fuels reduced both the number and the mass-based emission indices compared to conventional jet fuel. These PM emission reductions were greater the greater the percentage of alternative fuel used and they were also found to decrease with decreasing aromatic content. These measured reductions peaked at idle and reduced with increased engine power.

Lobo et al. [21] evaluated the gaseous and PM emissions of an Auxiliary Power Unit (APU), a small gas turbine engine, burning alternative fuels compared to conventional Jet A-1. The alternative fuels were obtained through the FT process, one from coal (coal-to-liquid (CTL)) and the other from gas (gas-to-liquid (GTL)). While the CTL fuel was only used in its neat form, the GTL was also tested in a 50% blend with Jet A-1. The results showed that for both the GTL fuels no difference was found in the NO_x emission, but the CTL combustion achieved a 5% reduction of this pollutant compared to the Jet A-1 at full power. For the CO emissions, on the other hand, all the alternative fuels got a reduction ranging from 5% to 10%. The best results, however, were observed for nonvolatile PM emissions. The neat GTL fuel got a 99% reduction in the number-based emission index at the idle condition, while the blend got a 60% reduction and the CTL fuel a 42% reduction. At full power, these numbers decreased but followed the same trend, 85% reduction for GTL, 20% for the blend and no difference for the CTL compared to Jet A-1. Following the same order, the reductions in mass-based emission index ranged from 90% to 65% and the smoke number ranged from 95% to 70%.

Talib et al. [22] analyzed, through experiments and simulations, the performance of an Armfield CM4 turbojet engine running on palm oil methyl ester biodiesel and its blends with conventional Jet A-1 fuel. The experimental analysis included the Jet A-1 and the 20% blend, while the 50%, 70% and 100% fuels were simulated using GasTurb 11 software. The experimental part of this study revealed that the 20% biodiesel blend performed comparably with the conventional Jet A-1 since the biggest difference in thrust was 4%, which decreased with power increasing. The oxygen presence in the biodiesel allowed a completeness of the combustion process leading to a combustor's efficiency rise of 2%. The usage of this blend led to a higher fuel-air ratio and specific fuel consumption, however, these value increases were minimal, ranging from 0% to 5%. The simulation part of the study showed that increasing biodiesel volumes in the blends led to decreased thrust production. Only the 20% and 50% biodiesel blends were considered viable for conventional jet fuel replacement.

The particle emissions of an unblended ATJ-SPK fuel and an unblended CH-SK fuel were studied by Schripp et al. [23] in a CFM56-5C4 engine. The results showed that the particle number and mass increased when using the CH-SK fuel compared to the reference kerosene contrarily to the ATJ-SPK fuel that achieved a reduction in these particle characteristics. Due to the correlation of the hydrogen and aromatic content with particle emissions, this was expected by the authors. Compared to conventional kerosene, the lower hydrogen and higher aromatic content in the CH-SK fuel increases particle mass and number. This way, the study proved that alternative jet fuels are not always associated with decreasing non-CO2 emissions.

The effect of fuel aromatics and hydrogen content on nonvolatile particle number and mass emissions was investigated, in an A320 equipped with V2527-A5 engines, by Schripp et al. [24]. The engines burned two reference kerosene and three blends with HEFA-SPK. The experiment showed that an increase in the hydrogen content leads to a decrease in particle emissions, not only comparing the fuel blends but also the fossil fuels between them. This study proves the importance of choosing the fossil fuel to use in an alternative fuel blend, since its properties, namely the hydrogen content, affect the particle emissions. The low aromatic content of a fuel also helps reduce soot formation. However, it is only noticeable at low power conditions, since at high power the parameters of the engine are more important than the chemical composition of the fuel.

Kroyan et al. [25] introduced a state-of-the-art mathematical model that allows, for the first time, a prediction of the fuel consumption in jet engines considering the most significant fuel properties. The developed model contains the effects of viscosity, density and calorific content in fuel consumption prediction. It presented a very high accuracy, which in validation presented errors below 0.68%. The fuels simulated were FT-SPK, HEFA-SPK, FT-SPK/A, HFS-SIP and ATJ-SPK, all of them certified in ASTM D7566. Compared to standard fuel kerosene, the results showed oscillations of fuel consumption between -0.85% and +3.72% and reductions in CO_2 emissions ranging from -3.22% and +0.42%.

HEFA-SPK and ATJ-SPK presented the best results in CO_2 emissions reduction compared to the other SAF, but due to their low density, the volume-based fuel consumption increased. On the other hand, these two fuels had the lowest mass-based fuel consumption. HFS-SIP had the highest mass-based fuel and energy consumption. This was due to its exceptionally high viscosity which is a sign of inefficient energy conversion and resulted in a blending wall limit of 10% with Jet A-1. This study concluded that SAFs have the potential to outperform conventional kerosene fuel not only from the environmental perspective but also in fuel and energy consumption.

Chapter 2

Turbofan Basic Principles

2.1 Gas Turbine Engine

The GTE is basically a heat engine that uses the surrounding air as a working fluid to provide thrust. The working principle of this type of engine is based on Newton's third law of motion which states that "for every force acting on a body there is an opposite and equal reaction". This thrust is achieved thanks to the acceleration of the air through the engine since the force needed for this acceleration has an equal effect with the opposite direction acting on the engine [26]. The GTE has three main components, as shown in Figure 2.1, that lead to the air's acceleration - a compressor and a turbine, the only two rotating parts, and a combustor. First, the air is sucked into the front of the engine by a fan. After, the compressor raises the air pressure. The compressor consists of a set of blades spinning at high speed, which squeezes the air. The compressed fluid is then sprayed with fuel into the combustor and a spark plug lights up the mixture. The temperature rise will cause an expansion of the burning gases through the turbine. This will result in a work output since the turbine also consists of a group of blades, that when spinning, will drive the compressor, attached to the same shaft. Finally, the heated air is expelled through the nozzle at the back of the engine. As the jets of gas shoot backwards, the engine is thrust forward [27, 28].

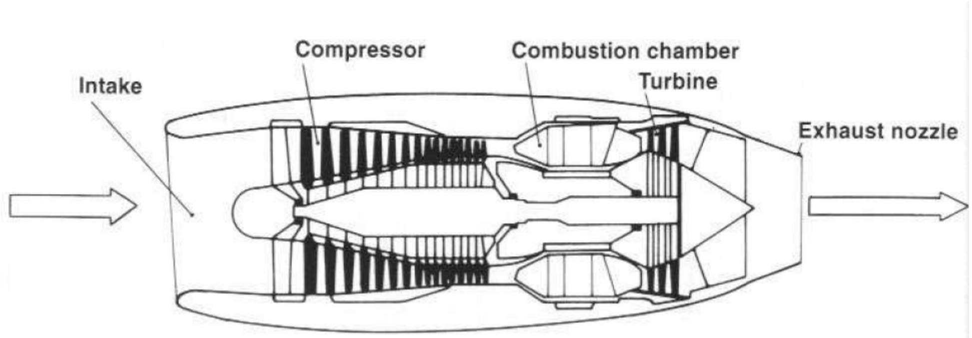

Figure 2.1: Components of a GTE [29].

2.1.1 Thermodynamic Cycle

All GTE's, where the turbofan engine is included, work using the same thermodynamic cycle. It is called the Brayton Cycle and is similar to that of the four-stroke internal combustion engine (ICE). Both engine cycles can be summarized in four main steps: induction, compression, combustion and exhaust. There are, however, two main differences between these two: in the GTE combustion occurs at constant pressure, while in the ICE it occurs at constant volume; and in the ICE the four strokes of the process take place in the concerned cylinders, making the engine cycle intermittent, whereas in the GTE different components have different steps of the process associated, making its cycle a continuous one [26, 29]. These differences and the fact that the GTE combustion chamber is not an enclosed space allow the air's pressure to be kept low during combustion when compared to ICE. This means that there are no peak or fluctuating pressures to be withstood allowing for a more light fabrication of the GTE's combustion chamber and the use of low-octane fuels [26].

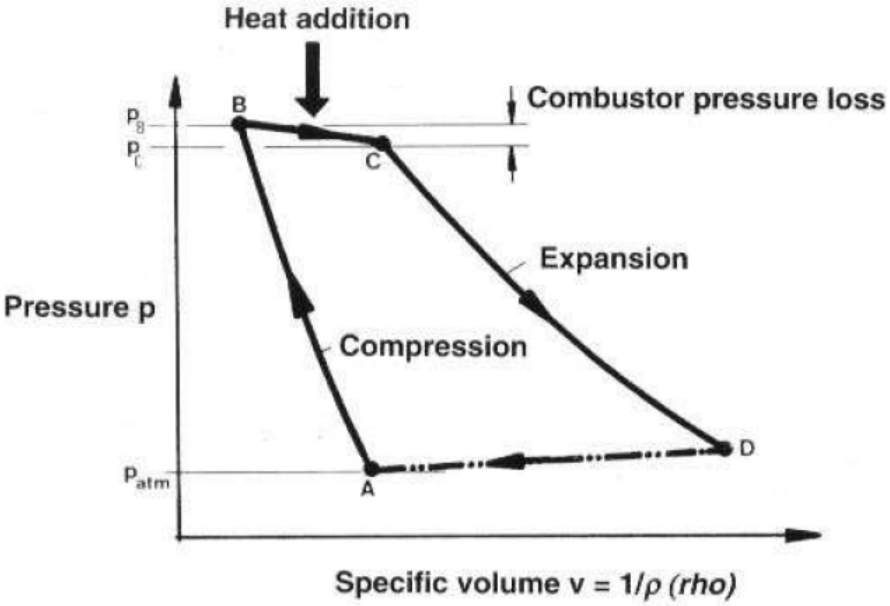

Figure 2.2: Brayton Cycle in pressure-volume diagram [29].

The Brayton Cycle, in its simplest form, can be graphically displayed in a pressure-volume diagram, as shown in Figure 2.2. This graphical representation allows a better understanding of the fluctuation of the state variables to which the gas is subjected when passing through the engine. The area enclosed by the four curves represents the heat added to the gas that will be used for work, either for shaft power to drive the compressors or for propulsive thrust [29]. The whole cycle can be described in the following steps [26, 29, 30]:

- Point A in the diagram represents the air being admitted into the engine at atmospheric pressure. From there, along line AB, the air is compressed and decelerated by the inlet and the compressor. Part of the flow's kinetic energy is converted into an increase in static pressure and temperature of the air. Point B represents the air being discharged from the compressor.
- From B to C the combustion process takes place. There, heat is added to the air by

introducing and burning fuel at, ideally, constant pressure. In reality, however, fluid dynamic friction and turbulence will lead to a small pressure drop, represented by the inclined BC line in the diagram. The sudden increase in the air's temperature will considerably increase the gas's volume.

- The expansion of the hot gases back to the atmosphere's pressure through the turbine and the exhaust nozzle is represented by the CD line in the diagram. In this step, the turbines use part of the energy present in the gas expansion to create mechanical power to drive the compressor, while the rest of the energy provides the propulsive jet necessary for thrust.

As mentioned before, the turbofan is a heat engine which means that the higher the temperature attained in the combustion, the greater the expansion of the gases and consequently the efficiency. There is, although, a limitation for the maximum temperature of the combustion because the gases' temperature entering the turbine should be suitable with the design and materials of the turbine [26].

2.2 Gas Turbine Engine Components

This section will succinctly describe the main components of a GTE. Following the flow's path, this description will start in the engine intake or inlet, then the compressors, followed by the turbines and it will finish in the nozzle or exhaust system. Since this work will analyse the combustion in the engine, the combustor description and its principles will have a dedicated section further in this chapter.

2.2.1 Engine Intake (or inlet)

The engine intake is basically a fluid flow duct whose main requirement is, under all operating conditions, to deliver airflow to the engine achieving the minimum loss of energy. The intake sits upstream of the compressors so, it must be able to provide the appropriate amount of airflow and additionally, this flow should be uniform, stable and of high quality. Although the inlet does no work on the flow, its performance is of high importance for the engine's net thrust and the overall aircraft performance, and for this reason, the intake design responsibility sits on the aircraft manufacturer, not the engine manufacturer [26, 29, 31].

Depending on the aircraft speed, engine intakes come in various shapes and sizes, so that the intake operates efficiently in the intended aircraft mission. This work, however, focuses on the CFM56-3 turbofan which flies under sonic speed, and therefore only subsonic air intakes will be mentioned. For aircraft with this type of engine, that fly at subsonic speeds or at low supersonic speeds, the ideal intake is a pitot-type circular intake as shown in Figure 2.3. These intakes are flow ducts whose cross-sectional area increases in the flow direction (divergent ducts) and, because they can reduce the flow speed and convert its kinetic energy into pressure, they are called diffusers. The diffuser's action in the flow helps to pressurize the air, considerably reducing the mechanical energy necessary from the compressor [26, 29].

The surface of this type of intake is characterized by a continuous smooth curve from outside to inside with some thickness from inside to outside. The uppermost portion of the inlet is called the inlet lip and, in this kind of intake, it is relatively thick to help reduce the risk of flow separation. The smoothed interior surface, with no steps or kinks, also prevents the sensitive boundary layer from separating. The flow's separation along the walls would lead to an unwanted conversion of the kinetic energy into heat, i.e., friction [26, 29, 31].

Figure 2.3: Pitot-type intake [26].

2.2.2 Compressors

Despite the variety of GTE, all have some parts in common. One of those is the compressor, which is responsible for increasing the pressure of the air coming to the combustor. It is one of the most important components of this type of engine since its performance greatly influences the overall performance [32].

There are two basic types of compressors: centrifugal and axial. In the centrifugal compressors, the flow is turned perpendicular to the axis of rotation, while in the axial compressors, the flow always travels parallel to the axis of rotation. The first GTE ever made only used centrifugal compressors, due to their simplicity and ruggedness, however, nowadays they are only used in smaller turbojet and turboshaft engines since axial compressors have far more advantages. For instance, axial compressors can deliver higher mass flow rates together with larger pressure ratios while using the same frontal area as a centrifugal compressor. These two advantages allowed modern engines to go from medium to high-thrust engines since these features have an important role in determining the amount of thrust the engine can provide. Besides, the fact that, in this type of compressor, the air flows in a single direction eliminates the need to turn the flow. So the cross-sectional area will be smaller than the corresponding centrifugal compressor and the aerodynamic drag of the engine nacelle can be reduced [29, 32]. For these reasons, and taking into account that the CFM56-3 employs an axial compressor, this section will have a special focus on this type of compressor.

An axial compressor, as shown in Figure 2.4, consists of alternate rows of moving and fixed blades with an airfoil section. The moving blades are called rotors and are fixed to a central shaft that rotates at high speed. On the other hand, the fixed ones are called stators and are fixed on the outer casing. A set of a rotor followed by a stator is called a stage and it increases the pressure of the air by a factor between 1.1 and 1.2. This is a small increase in the pressure hence the use of a multistage unit, because the increase in the pressure is multiplied from row to row, e.g., a 10-stage compressor at 1.2 per stage gives a total pressure ratio of 6.2. The use of these multistage axial compressors minimizes losses and results in higher efficiencies and lower fuel consumptions [26, 27, 32].

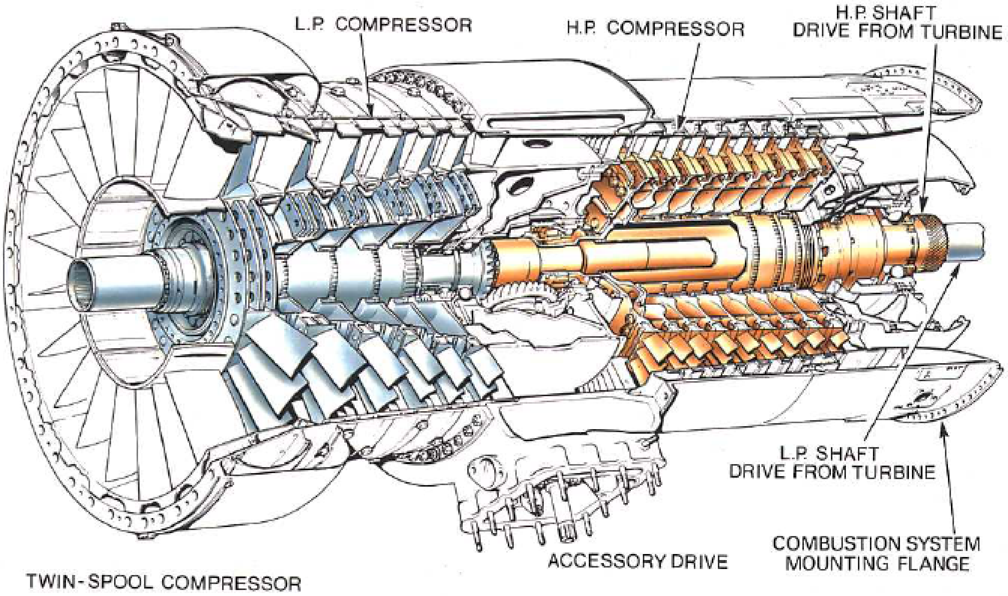

Figure 2.4: Typical twin-spool axial compressor [26].

When entering the compressor, the air is accelerated by the rotor and then decelerated by the stator converting the kinetic energy into static pressure. The stator is also responsible for guiding the air into the next stage with the correct angle and preventing it from spiralling around the axis, bringing it back parallel to the axis. The last stator straightens the air by removing possible air swirls before entering the combustion chamber. Both the stator and the rotor contribute to the pressure rise along the compressor. As the pressure of the air increases from the front to the rear of the compressor, the volume of air must decrease to keep the velocity constant from stage to stage. So the annulus area between the rotor shaft and the stator casing, as well as the blade height, suffer a gradual decrease along the axis of the compressor [26, 27, 32]. To have a better visualization, in Figure 2.5 a graphic represents the pressure and velocity variation along the compressor.

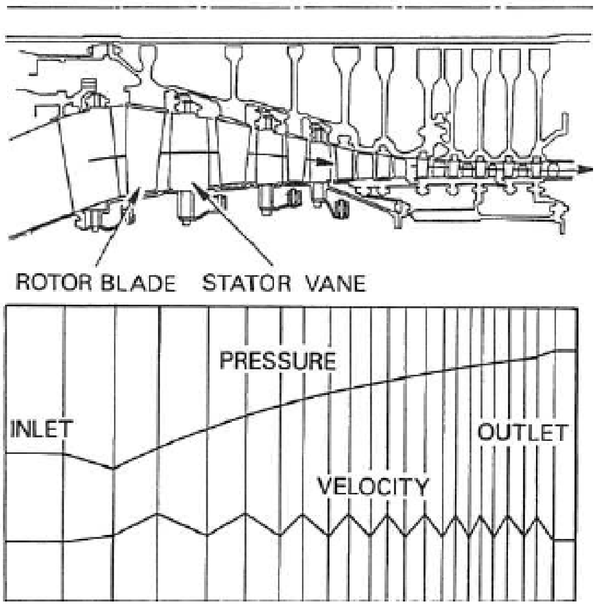

Figure 2.5: Pressure and velocity variation through an axial compressor [26].

Although the first turbojet engines only had a single spool, i.e., a single rotor assembly, with as many stages necessary, connected to the turbine through a single drive shaft, modern turbofan engines, like the CFM56-3, require multi-spool arrangements. In these multi-spool arrangements, more than one drive shaft connects the compressor to the turbine, e.g., in a twin-spool engine the low pressure compressor (LPC) is connected to the low pressure turbine (LPT) and the high pressure compressor (HPC) to the high pressure turbine (HPT). This way, each rotor assembly is driven by its turbine at an optimum speed to achieve higher pressure ratios and to give greater operating flexibility [26].

Besides the typical stages in the compressor, turbofans have a fan as the first compression stage right after the inlet. This fan compresses the air at a high-pressure ratio at the tip and normal pressure ratio values at the inner radius. Then, in high bypass ratio turbofans, like the CFM56-3, most of the flow is expanded through its own coaxial nozzle, and the remainder, the smaller part, goes to the engine's core. This way, a single rotating blade row achieves high flow per unit of frontal area, high efficiency and high pressure ratio. Turbofans get a big part of their thrust just from the fan and the rest from the core, this way for nearly the same amount of fuel, this engine generates far more thrust than a turbojet, meaning they are more fuel efficient [26].

2.2.3 Turbine

The turbine's main task in a GTE is to provide the necessary power to drive the compressors and possible accessories. In the case of turboprops and turboshafts, its main task is to give power to the propeller and the rotor blades, respectively. Contrary to what happens in the compressor, the turbine absorbs the required energy from the combustor's hot gases, expanding them to lower pressure and temperature conditions. This way the energy is converted into mechanical shaft power or torque. As in compressors, there are also two basic types of turbines, radial flow and axial flow, however, in this case, except for a few, almost all engines employ the axial flow type of turbine since the radial option is not as practical [26, 29].

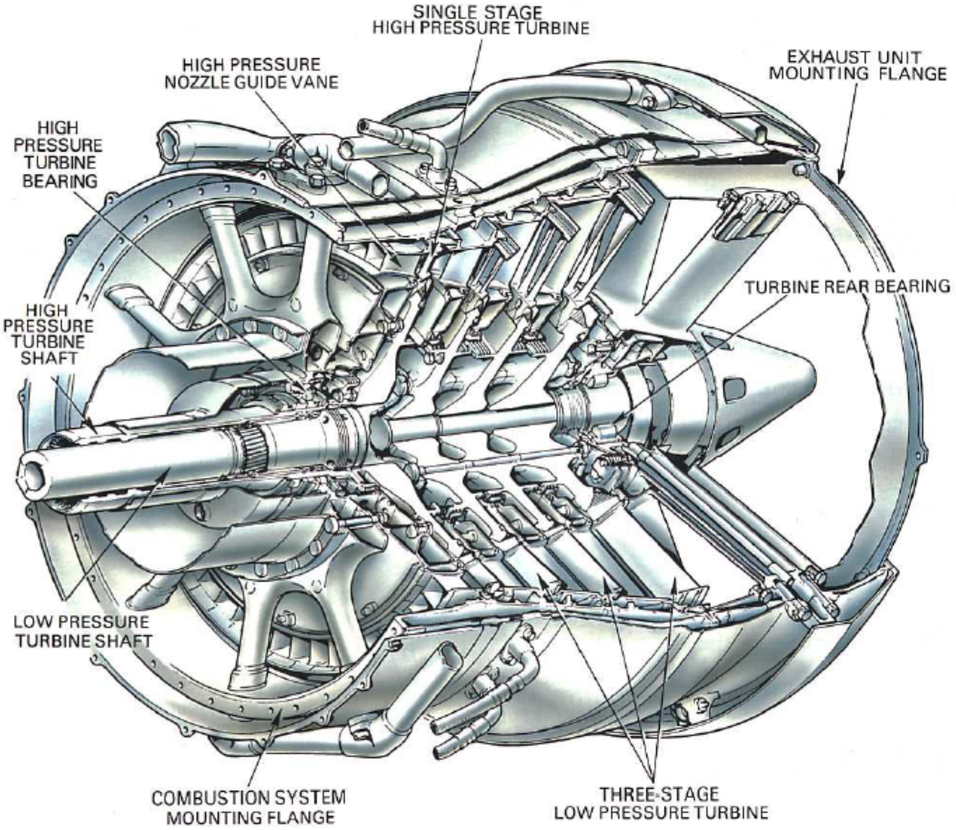

Figure 2.6: Typical twin turbine [26].

Again, similarly to the compressors, an axial flow turbine consists of a single or a set of stages. Each stage comprises a row of stationary nozzle guide vanes followed by a row of rotating blades (rotor), thus the order is inversed when compared with a compressor stage. Modern engines, with high compression ratios, require turbines to be multistage, but the number of stages in the turbine is much lower than the ones in the compressor. This happens because the flow's pressure is decreasing across the turbine, and so, the pressure gradient helps the boundary layer to stay attached to the surface of the turbine blades. Since the boundary layer is less likely to detach, the pressure drop in one turbine stage can be much greater than in a corresponding compressor stage. Hence one turbine stage can drive multiple compressor stages [29, 33]. Typically in turbofans (like the CFM56-3), similarly to compressors, the turbines are divided into two sections, the high-pressure and the low-pressure, like the one in Figure 2.6. As said in 2.2.2, two shafts connect separately the LPC to the LPT and the HPC to the HPT. The HPT appears upstream of the LPT.

The nozzle guide vanes and the rotor blades are designed predominantly on aerodynamic considerations, and so its sections have basic airfoil shapes. The amount of energy converted in the stator and rotor defines the type of turbine stage, which can be an impulse turbine, a reaction turbine or a mix of both (impulse/reaction turbine). Pure impulse or pure reaction turbines are not usually used, so only the working principle of the impulse/reaction turbine will be explained here [26, 29].

The nozzle guide vanes, responsible for the impulse part, have two main tasks. First, due to the convergent cross-sectional area between adjacent blades, potential energy (heat and pressure) is converted into kinetic energy. This way, the flow is accelerated to almost sonic speeds and its impact on the rotor blades will create an impulse force. Second, the nozzle guide vanes also give the flow a spin in the direction of the turbine's rotation, maximising the shaft power produced. The rotor section, responsible for the reaction part, allows for the expansion of the hot gases to be continued because between adjacent blades the flow path cross-sectional area is also narrowed. Due to the airfoil shape of the rotor blades, an aerodynamic force is generated on the blades which, allied with the impulse force, helps the turbine to rotate faster [26, 29]. Figure 2.7 helps to illustrate the design of impulse/reaction turbines.

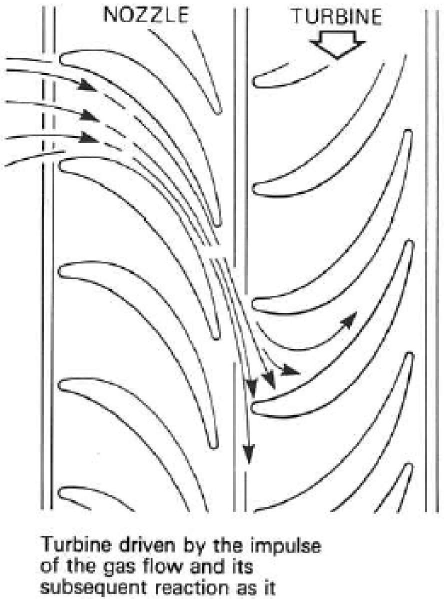

Turbine driven by the impulse
of the gas flow and its
subsequent reaction as it
accelerates through the
converging blade passage

Figure 2.7: Impulse/reaction turbine [26].

It is noteworthy that turbine blades are exposed to much more hostile conditions than compressor blades. Because the turbine is placed exactly downstream of the combustor, turbine blades experience temperatures between 850 and 1700°C. To help prevent the blades from melting heat resistant materials like nickel alloys with ceramic coatings are used, however, this is not enough, and so blades must be actively cooled. To accomplish this, the blades must be hollow and part of the compressor delivery air must be passed through them [26, 33].

2.2.4 Exhaust Nozzle

All GTE have an exhaust system usually called a nozzle, that passes the discharged gases from the turbine back into the free stream at the desired velocity and direction so that thrust is produced. That is to say, the main task of the nozzle is to convert the gas potential energy into kinetic energy, i.e. gas velocity, to provide the necessary thrust. This is achieved simply with the geometrical shape of the nozzle, which is a pipe with varying cross-sectional area. Depending on the type of mission assigned to the aircraft, there can be several types of nozzles with different shapes and sizes. Typically, turbojet and turbofan engines employ convergent nozzles. Usually, high-bypass turbofan engines have separate nozzles for the hot and the cold streams. The two nozzles are generally co-axial and the area of each is designed to obtain maximum efficiency [26, 29].

The gas coming from the turbine and entering the exhaust system still comes at a high velocity, which can result in high friction losses. Thus, there is a need to reduce the flow speed by diffusion. This is done with the use of an exhaust cone that promotes the increases in the passage area between it and the outer wall. To reduce the losses due to possible whirls coming from the turbine, the turbine's rear support struts are designed in such a way that the flow is straightened before reaching the jet pipe. After this, the gas is then accelerated thanks to the reduction of the cross-sectional area in the streamwise direction, i.e., the convergent duct. In almost all conditions, the flow reaches the sonic speed, a condition at which the propelling nozzle is said to be choked. This means that it is not possible to increase the jet velocity further. However, if the upstream total pressure is increased above the value at which the nozzle is choked, the gas static pressure at exit will be higher than the atmosphere pressure. This pressure difference results in an additional fraction of thrust called pressure thrust [26].

2.3 Combustor

The combustor, or burner, is located between the compressor and the turbine. Its goal is to introduce heat energy to the extensive volumes of air coming from the compressor by burning large quantities of fuel so that the gases resulting from the combustion can be expanded to get work output that drives the turbines [26, 27]. In other words, it can be said that the combustor's task is to convert the chemical energy of the fuel into thermal energy. To achieve this task the combustor must [34]:

- Mix the air and fuel entering the combustor;
- Ignite the mixture of fuel and air;
- Accommodate the mixture during the combustion reaction;
- Tailor the temperature distribution of the hot gases exiting.

The design of a GTE combustor is a rather difficult task due to the high continuous combustion temperature, large continuous flow and high heat energy release that it must endure. So, most of the combustors are empirical, i.e., based on experience and previous systems, resulting from years of development work. Despite various types of combustor designs, generally, all combustors incorporate the same key parts like the air casing, diffuser, liner, fuel injector, and spark plug [27, 29, 35].

The combustor is one of the most critical components of the GTE because it must operate reliably at extreme temperatures and provide a suitable temperature distribution for the turbine while creating the least amount of pollutants possible so that the effects of the rapid increase in commercial aviation are mitigated [26, 36].

2.3.1 Combustor Performance Characteristics and Requirements

The GTE combustor must satisfy a set of requirements to achieve optimum combustion at the aircraft operation conditions. Although their importance varies from engine to engine, the key requirements and characteristics of the combustor can be listed as follows [27, 29, 35, 36]:

1. High combustion efficiency, i.e., all the fuel injected into the combustion chamber should be burnt to convert all its chemical energy into heat. This is not fully achievable because it is difficult to apportion the exact amount of air for complete combustion for all the aircraft operating conditions;
2. Stable and smooth combustion range to prevent the flame from going extinct in the combustion chamber from idle to max thrust and from sea-level pressure to high altitude pressure. This means the flame should be alight over a wide range of air/-fuel ratios and pressures. The flame is also sensitive to high entry velocities in the combustor since the flame can become extinct;
3. Reliable and smooth ignition over a wide range of operating conditions, especially at very low ambient temperatures on the ground and at high altitudes in the event of a flameout;

4. Minimum pressure losses, as this can reduce the work output of the engine;
5. Uniform exit temperature distribution (pattern factor) so that no hot spots exist and the turbine blades and nozzle guide vanes' lives are maximized. This uniform distribution of the temperature can be achieved through a more intense mixing of the fuel and the airflow;
6. Low emissions of smoke, gaseous pollutant species and carbon deposits. Rich fuel/air ratios, i.e., insufficient oxygen for the complete combustion lead to the formation of carbon deposits that may erode and damage the turbine blades or block cooling air passages;
7. Minimum size and weight;
8. Design for minimum cost and ease of maintenance;
9. Easy to dismantle and service, i.e., maintainability.

The requirements given above are sometimes incompatible or contradictory. For example, as mentioned in point 5, a high degree of turbulence leads to a more uniform temperature distribution as well as a more efficient combustion, however, this also leads to higher pressure losses in the combustor, making these factors mutually incompatible. This means that the combustor design requires careful assessment of contradictory factors and it is an exercise of compromise. Usually, low fuel consumption, low pollutant emissions, and size and weight are the main considerations for aircraft GTE combustor designers.

2.3.2 Combustor Basic Design Characteristics

Before getting into the full details of the combustor working principles, it is interesting to briefly analyse the aspects that determine the basic geometry design characteristics of a typical GTE combustor. These aspects will be presented as modifications in the simplest possible combustor to meet its basic performance requirements.

The simplest possible combustor is represented in Figure 2.8 (a) and it is basically formed by a straight long duct connecting the compressor to the turbine. This configuration, however, presents a big problem, the pressure loss during combustion would be excessive, up to 25% of the compressor pressure [27]. This is induced by the high inlet velocity of the flow since the pressure drop is proportional to the square of the air velocity [35]. To solve this, the velocity should be reduced by using a diffuser, as shown in Figure 2.8 (b). This solution will reduce the incoming air velocity to about one-fifth, reducing the pressure loss during combustion [27, 35]. Despite the pressure loss problem being solved, the continuous airflow still causes another problem, it is too high for the flame to be anchored and combustion to be stabilized. So, a flow reversal should be created to lower the velocity to almost stagnant. One way of doing this is by using a plain baffle, as shown in Figure 2.8 (c).

There is only one shortcoming in this last combustor disposition. To get the desired temperature rise in the combustor, the air/fuel ratio should be around 30-40 and these values are way outside the flammability ratios. So a local air/fuel ratio of about 13-15 should be created in the primary combustion region of the chamber. This can be done using an inner chamber, as shown in Figure 2.8 (d), with various holes that will apportion the air along the combustor. The first set of holes will deliver only the necessary air for a near stoichiometric air/fuel ratio, while the others will deliver the rest of the air downstream so that the temperature is decreased to an acceptable level for the turbine. The secondary air entering the chamber is thoroughly mixed so that the temperature is uniform at the exit [27, 35].

This way Figure 2.8 represents the development of a conventional combustor with all its basic components: air casing, diffuser, liner and fuel injector [35].

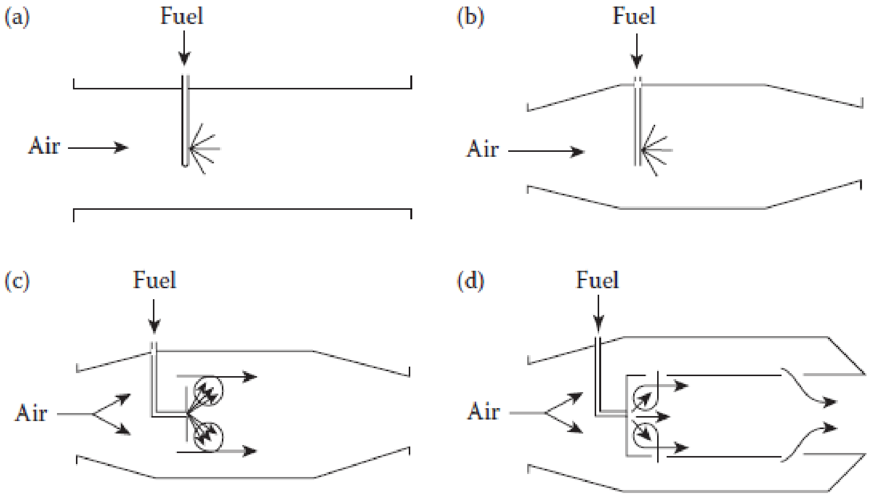

Figure 2.8: Development of a GTE combustor: (a) straight duct, (b) added diffuser, (c) added plain baffle, (d) final combustor geometric iteration with inner chamber [35].

2.3.3 Types of Combustor

The aircraft's requirements, the overall engine design and available space in the engine determine the combustor type and layout choice. The combustor types can be classified according to their geometrical characteristics. Although there is a wide number of configurations, all combustors can be classified into three basic types:

- Can or tubular combustor;
- Annular combustor;
- Can-annular or tubo-annular combustor.

2.3.3.1 Can or tubular combustor

This type of combustor consists of a set of tubular liners each mounted concentrically inside its cylindrical casing, ranging from 6 to 16, arranged in parallel around the engine's axis. Each burner has a supply of airflow coming from the compressor by separate air ducts [27, 29, 35]. However, all burners are interconnected enabling the flame to be spread to all of them. It also ensures that combustion occurs simultaneously and that pressure is equalized between burners, thus reducing asymmetric turbine loading [29]. This type of combustor, like the one shown in Figure 2.9, was featured in early engines but it's not used in modern aircraft. It is no longer an option for modern aircraft engines because it uses inefficiently the available space, making them too large in frontal area, volume and weight. The main advantages of this type of combustor, which made it the primary choice of the earlier GTE, were: the little time and money involved in the development since tests could be made in only one of the burners, and the mechanical robustness and resistance to warping [27, 35].

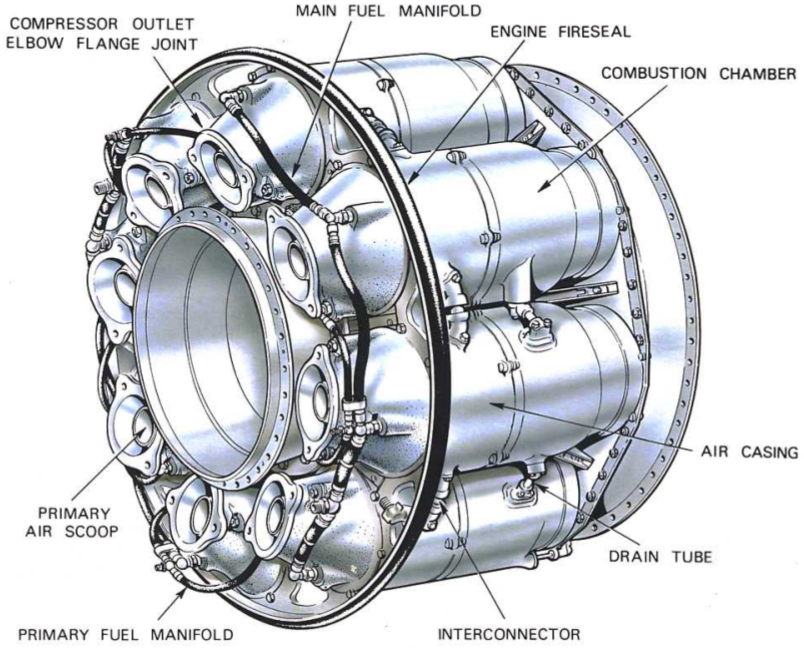

Figure 2.9: Can type combustor [26].

2.3.3.2 Annular combustor

An annular combustor consists of a single concentric flame tube mounted around the spools of the engine, as shown in Figure 2.10. The combustion chamber is contained between the inner and outer casing forming a completely annular form [26, 29]. This type of combustor has, in many ways, an ideal form of chamber due to its clean aerodynamic layout which results in lower pressure losses when compared to other configurations [35]. It is also the ideal configuration in terms of space usage making it 25% lighter compared to a similar tubular combustor [29]. There is also a circumferential pressure equalizing enhancement, compared to a can combustor, because this combustor configuration consists of a single combustion chamber. All these advantages make this type of combustor the chosen one for modern GTE, like the CFM56-3, the engine studied in this thesis.

There are, however, some disadvantages associated with this configuration. High cost of developing, because unlike can combustors it's not possible to test only a part of the combustor, and serious buckling problems in the outer chamber are some of the disadvantages that led to the development of can combustors before the annular ones [27, 35, 36]. The evolution of computational analysis, like CFD, and the evolution in materials science and structural analysis, made these problems surpassable through the years. Some disadvantages remain, e.g., it is more difficult to obtain an even fuel/air distribution and an even outlet temperature distribution and is more sensitive to flow velocity variations [27, 36].

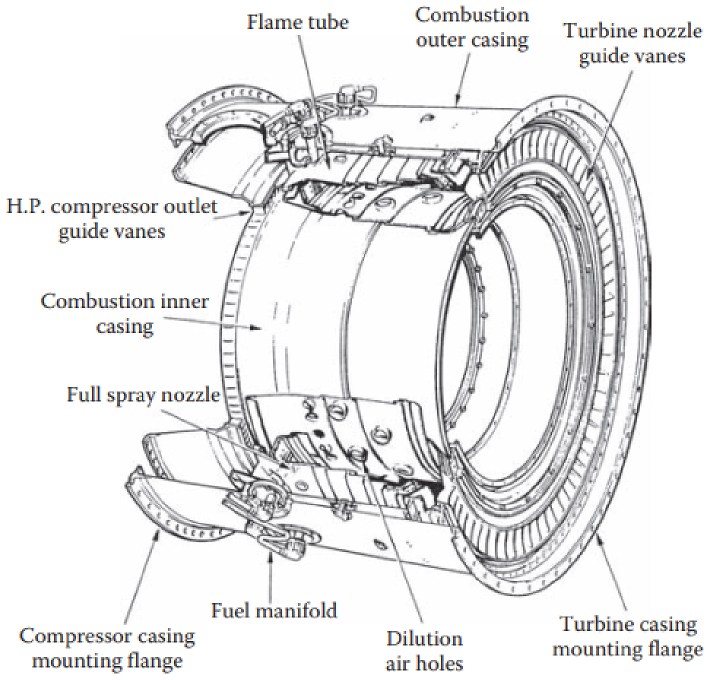

Figure 2.10: Annular type combustor [35].

2.3.3.3 Can-annular or tubo-annular combustor

The can-annular combustor makes the evolutionary connection between the can combustor and the annular combustor, i.e., it was the intermediate solution towards the annular combustor that is the best suited for modern jet engines [26, 29]. It consists of a set of tubular liners, usually from 6 to 10, inside a singular and common annular air casing. The primary air is supplied through individual air intakes, like the can combustor, but the secondary air is provided to the flame tubes by the common air casing [29, 35].

This type of arrangement combines the benefits of both the previous types of combustors.

Like the can combustor, this configuration benefits from the ease of overhaul, robustness and mechanical strength hence resistance to warping. On the other hand, it shares the compactness and efficient use of space as well as the low-pressure loss with the annular system [26, 27, 35]. It still has some drawbacks, however, e.g., the need for interconnections persists and has difficulties in achieving consistent and satisfactory airflow patterns [35].

2.3.4 Combustion Chamber Design Description

This subsection will focus on the combustion chamber because it is responsible for restricting the flame zone inside it hence one of the most important combustor components. The combustion chamber's basic design features in charge of creating the best combustion environment will be described here. These features include not only the several zones to which the combustion chamber is divided, i.e., the primary zone, the secondary zone and the dilution zone but also some components like the swirler and the various wall jets. To better understand the combustion chamber zone separation, Figure 2.11 presents where each zone is located.

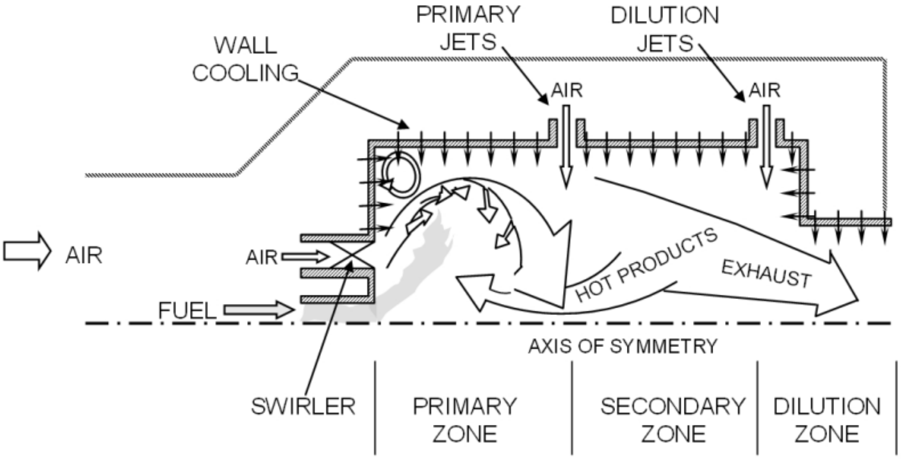

Figure 2.11: Combustion chamber basic features and zones subdivision [34].

2.3.4.1 Primary zone

The primary zone is the upstream section of the combustion chamber. Its function is to anchor the flame, i.e., prevent it from being put out, and give enough time, temperature and turbulence to achieve an almost complete combustion of the incoming air and fuel mixture. This section of the combustor is usually characterized by a fuel rich mixture to promote reaction stability and prevent blow-out [34]. Despite the many different flow pattern types that a combustion chamber can have in the primary zone, all of them create a toroidal flow reversal. This flow feature helps a portion of the hot gases to be entrained and recirculated with the incoming air and fuel thus providing a continuous ignition [35].

The air coming from the compressor enters the combustor through four main points and each point injects approximately 25% of the total airflow. Two of these points, swirler and primary air wall jets, control and sustain the structure and mixing within the primary zone. Both swirling air and primary air jets are capable of creating a flow reversal, so earlier combustors had no swirlers and relied only on wall jets, however, the use of the two is beneficial since the two separate modes of air injection complement and strengthen each other [34, 35].

2.3.4.2 Swirlers

The swirlers are the first entry points of the combustion chamber for the incoming compressed air. They are positioned at the beginning of the combustor and usually surround the fuel injection port, represented by the ”X” in Figure 2.11. Their function is to generate a circumferential velocity component in the air and as a result, the air moves radially outwards as it enters the combustion chamber. This creates a pressure void at the centerline which in turn incites a backflow to fill the pressure deficit. The turbulence created by the air passing through the swirler vanes also enhances the fuel and air mixing. This mixture is then mixed with the hot gases from combustion pulled downstream into the recirculation zone which provides an ignition source for the fresh mixture. Effectively, this zone acts as a ”blender” and ”spark plug” at the same time. The recirculation flow created extends approximately one duct diameter downstream and defines the primary zone section [34].

2.3.4.3 Primary air jets

Usually, combustors have two air wall jets, one at the end of the primary zone (primary jets) and one at the end of the secondary zone (dilution jets). They affect the mixing, stoichiometry and structure of the flows. The primary wall jets serve two main functions. Firstly, because they are positioned at the end of the primary zone, they prevent the recirculation flow from getting out of its section by providing a strong force against which the flow can't penetrate. Without them, aerodynamic fluctuations would occur, resulting in pressure losses, undesirable noise and higher pollutant emissions. Secondly, the primary air jet bifurcates with a substantial percentage directed upstream hence helping the swirler air attain the overall primary zone stoichiometry. The remainder will mix downstream in the secondary zone [34].

The chemical energy transformation present in the fuel into heat occurs in a two-step process. The first step of this process is held within the primary zone. The chemical bonds between the hydrogen and the carbon are converted through a series of reactions, at a relatively fast pace, into CO and H_2O. In this first phase, approximately two-thirds of the fuel chemical energy is converted into heat energy. The remaining one-third is present in the CO and it can't be converted in the primary zone due to the relatively slow kinetic rate of CO oxidation into CO_2, the short residence time in the recirculation zone, and the rich stochiometry of the primary zone [34].

2.3.4.4 Secondary zone

The secondary zone's main objective is to promote the CO oxidation into CO_2, i.e., finish the fuel chemical energy conversion into heat referred to in 2.3.4.3. To achieve this as fast as possible and expedite the slow reaction, an overall lean mixture ratio should be established using the bifurcated primary air jet; the temperature must be kept high; and enough residence time for the oxidation should be provided [34]. This way incomplete combustion and the presence of CO and unburned hydrocarbons (UHC) in the GTE emissions are prevented.

2.3.4.5 Dilution zone

The dilution zone is the last section inside the combustion chamber. Its main objective is to admit the remaining air after combustion and mix it with the resultant hot products so that the outlet flow temperature is suitable for the turbine. This is done using the dilution air jets, the second major set of air jets referred to in 2.3.4.3. As mentioned, it accounts for approximately one-quarter of the total airflow from the compressor. This amount of air added will bring the air-fuel mixture into a very lean condition, i.e., very high air concentrations compared with the stoichiometric ratio [34].

To prevent damaging the turbine, it is not enough to reduce the mean temperature of the outlet airflow, since the radial and circumferential variation of temperature can create hot spots and damage the various turbine components. So, the temperature profile at the exit plane must meet design criteria. This temperature profile is usually described and characterized by various indices like the Pattern Factor, the Profile Factor and the Turbine Profile Factor [34]. Theoretically, achieving any temperature traverse quality is possible using a long dilution zone. In practice, however, it is proven that the mixedness initially improves quickly with the increase in length, but progressively slows after. This is the reason why the length/diameter ratios of dilution zones typically range between 1.5 and 1.8 [35].

Combustor designers will work together with turbine designers to define the outlet temperature design profile, like the one shown in Figure 2.12. As presented in Figure 2.12, the temperature design profile is typically characterized by a reduced temperature at the root to protect the blade attachment to the shaft, where stresses are higher, and a reduced temperature at the tip to manage clearance at the wall and to protect seal materials [34, 35]. A large part of the combustor development is taken by attaining the desired pattern factor, due to its importance and severity [35]. The actual temperature profile, however, may slightly change compared to the design one.

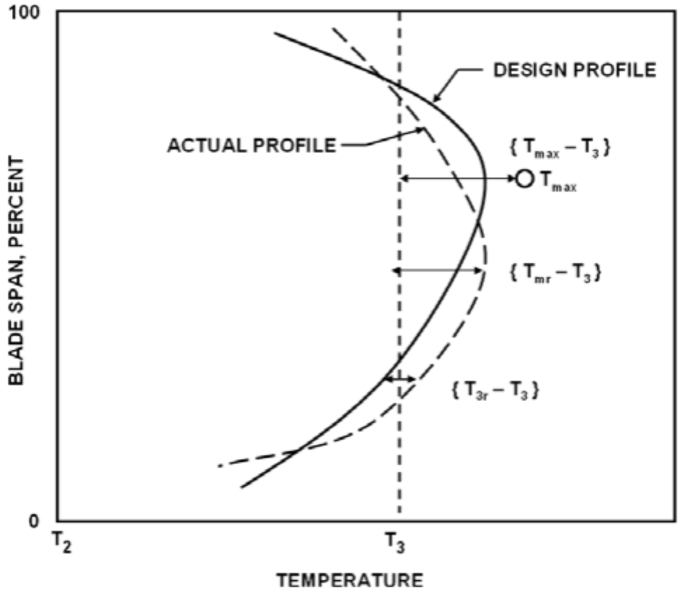

Figure 2.12: Exit plane temperature profiles [34].

The index with the most importance for the nozzle guide vanes is the pattern factor that characterizes the extent to which the maximum temperature, T_{max}, deviates from the average temperature rise (or mean exit temperature), T_3, across the combustor, defined by Equation 2.1 [34, 35].

$$\text{Pattern factor } = \frac{T_{max} - T_3}{T_3 - T_2} \tag{2.1}$$

where T_2 is the inlet air temperature in the combustor.

On the other hand, the temperatures with the most significance for the turbine blades are the ones that constitute the mean radial or circumferential profile. So, in this case, the profile factor is used and it characterizes the extent to which the maximum circumferential mean temperature, T_{mr}, deviates from the average temperature rise across the combustor, presented by Equation 2.2 [34, 35].

$$\text{Profile factor } = \frac{T_{mr} - T_3}{T_3 - T_2} \tag{2.2}$$

The two previous indices don't take into account the design profile, so the turbine profile factor is used, and it addresses the maximum temperature difference by comparing the average temperature at any given radius around the circumference, T_{3r}, and the design temperature for that same radius, T_{3des}, as shown in Equation 2.3 [34, 35].

$$\text{Turbine profile factor } = \frac{(T_{3r} - T_{3des})_{max}}{T_3 - T_2} \tag{2.3}$$

The goal is to achieve an actual temperature profile that matches the design profile and the dilution jet penetration is the major force that determines if the goal is achieved [34].

2.3.5 Wall Cooling

As the permissible inlet turbine temperature has been increasing over the last few years, the problem of the combustor walls' cooling has increased in importance. So, the liner wall must have sufficient thermal resistance to endure the continuous and cyclic high-temperature operation. Producing this component from high-temperature and oxidant-resistant materials is not enough, since it can deteriorate and melt, so cooling air must be used to help reduce the walls' temperature. In modern combustors, around 20% of the incoming compressor airflow is used for this purpose. One would think that more air used for wall cooling would be beneficial, however, this is not acceptable because it would reduce the available air for combustion and dilution. Furthermore, it would worsen the radial temperature profile at the combustor exit plane, hence reducing the turbine blades' life. So, the solution relies solely upon using efficient cooling methods, and if possible, even reducing the amount of air used for this. The liner wall's temperature is determined by the balance between the heat received from hot gases through radiation and convection and the heat transferred through convection to the cooling air and through radiation to the air casing [35].

There are several film cooling methods to reduce the heat in the liner wall, however, the term *film cooling* defines systems where several annular slots provide air injected axially along the inner wall of the liner to give a protective film of cooling air between the liner wall and the hot gases from combustion. The hot gases' turbulent mixing gradually destroys the film of cooling air so the annular slots are usually placed in a sequence along the length of the liner. This problem fades downstream of the liner since the flow acceleration at the nozzle reduces the turbulence and the cooling film can endure for a longer distance. One of the disadvantages of these methods is that a uniform wall temperature can't be achieved. The temperature is lower near the slot and increases downstream the wall until the next slot [35]. Several film-cooling devices like wigglestrips, stacked rings, splash-cooling rings and machined rings exist, but only the latter will be here explained since it is the one employed in the CFM56-3 engine [37, 38, 39].

A machined ring liner consists of either a single piece of metal that was machined or several rings welded together. Several rows of holes are then drilled in the liner walls to allow annulus air to enter the cooling slot by either total pressure feed, static pressure differential, or a combination of both, as shown in Figure 2.13.

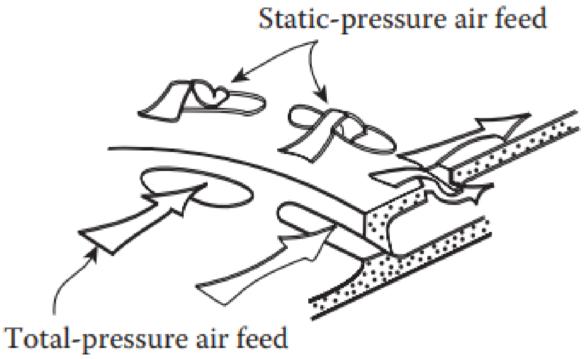

Figure 2.13: Machined ring film-cooling device [35].

This wall-cooling solution presents some advantages since it can more accurately control the cooling air quantity needed and it has improved mechanical strength, which, as mentioned in section 2.3.3.2, is important in annular combustors [35].

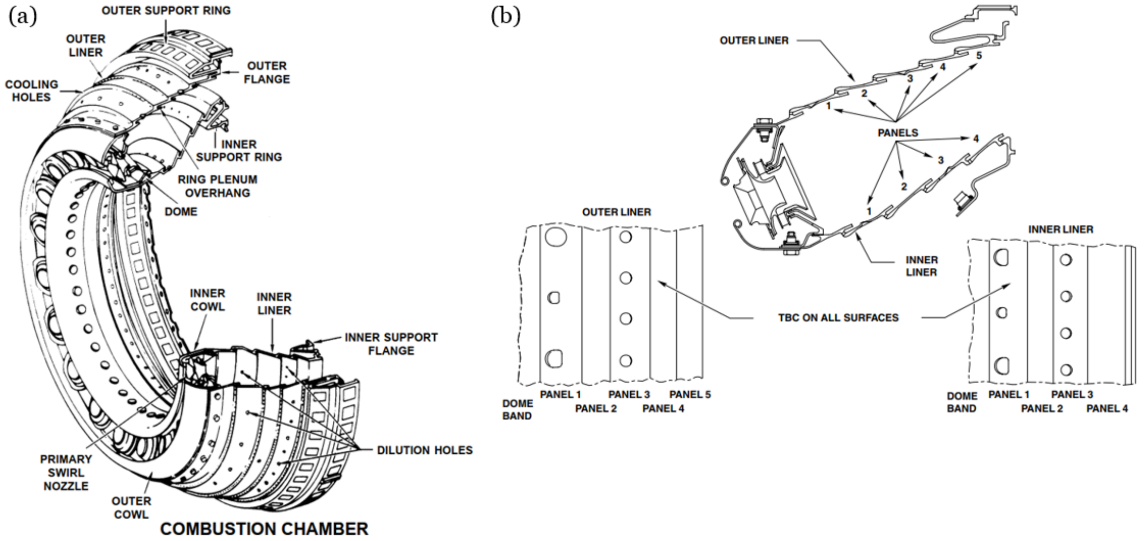

Figure 2.14: (a) CFM56-3 combustion chamber overview [37], (b) cutview of the CFM56-3 combustion chamber [38].

The total airflow of the drilled holes is carefully calculated to match the exact amount of cooling air required. The end of each liner panel is designed to provide a plenum to dissipate turbulence and to allow the jets to merge and form a single annular air film. At the downstream end, the gap width is designed to get the desired cooling air velocity, hence an optimum value can be fixed for maximum cooling efficiency despite the pressure drop across the liner [35]. In Figure 2.14 (a) the position of one of the sets of cooling holes is represented in the CFM56-3 combustion chamber overview. Knowing that at the beginning of each panel, there is a set of cooling holes, from Figure 2.14 (b), the position of all the cooling holes can be deduced.

Besides the film cooling device explained above, the CFM56-3 also uses a technology called Thermal barrier coating (TBC) [38]. It consists of a protective coating sprayed on the liner walls, which in this combustion chamber's engine is applied to both the inner and outer walls, as can be seen in Figure 2.14 (b), and it increases the efficiency of cooling by decreasing the liner wall temperatures by up to 150K [35].

2.4 Ignition

Gas turbine combustion, as mentioned before, is continuous and self-sustaining, however, there is the need for an ignition system. This system is important for the light up during ground starting, while the engine speed increases to a self-sustaining one, and should also be able to rapidly relight the chamber if a flameout occurs mid-flight. The flameout might happen under severe climatic conditions or on takeoff from a wet runway, where there is the risk of ingestion of large amounts of water and ice [35]. The first step in starting a GTE is to accelerate the compressor to a minimum speed capable of delivering an airflow that sustains combustion. During this acceleration, the ignition system is switched on and fuel is fed when the rotational speed reaches about 15 to 20% of the normal. When self-sustaining operation is achieved the ignition system is switched off. There are several ways of igniting a combustible mixture, but an electric spark is generally the mean chosen for the ignition in the GTE's combustor [35].

2.4.1 Ignition Process

The ignition process in a GTE combustor consists of three distinctive phases. A failure in any of these three phases will lead to a failed attempt to ignite the combustor, so the recognition of this phased process helps understand various apparent anomalies [35].

Phase 1 concerns the formation of a kernel of flame with enough size and temperature for propagation. This phase is affected by the effective air/fuel ratio adjacent to the plug (which should be close to stoichiometric), the energy and duration of the spark, the local conditions of velocity and turbulence, and the igniter plug position and extent to which it protrudes through the liner wall [35].

Phase 2 consists of the following propagation of the flame from the kernel to all parts of the primary zone. The igniter location and whether the kernel is well entrained into the primary zone reversal or is swept away downstream influence this stage. Some factors like the increase in pressure and temperature, the reduction of the primary zone velocity, or any change in the air/fuel ratio toward the stoichiometry value improve phase 2 [35].

Finally, phase 3, which only applies to can and can-annular combustors, regards the spread of the flame from a lighted liner into an unlighted liner. The main factors affecting this phase are the location and characteristics of the interconnections. The tube entrance should be in the highest gas temperature region and the exit should direct the flow towards the recirculation zone of the adjacent liner. It's also beneficial if the interconnections are made with a large flow area and a short length [35].

To understand why the ignition performance is unsatisfactory, it is necessary to determine which phase is causing the problem. This is done by examining the position of the ignition loop with the stability one. Figure 2.15 presents the two main types of ignition failure.

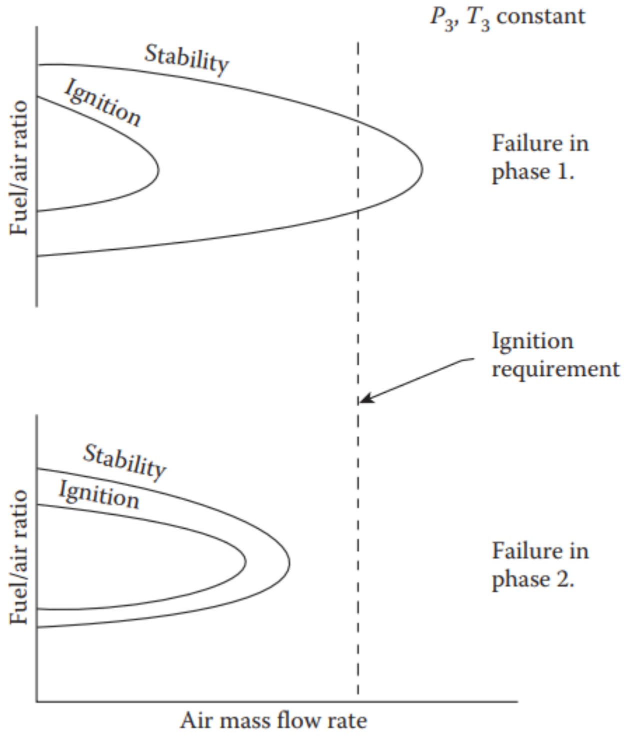

Figure 2.15: Graphic representation of the two main types of ignition failure [35].

If the ignition loop lies well inside the stability limits, like the first diagram in Figure 2.15, then the problem occurs in phase 1. This problem can be corrected with a change in the spark energy. If, on the other hand, the ignition loop is close to the stability loop, as in the second diagram of Figure 2.15, the performance limitation is certainly in phase 2. Failure occurs in phase 3 if the maximum relighting altitude is significantly less than the value predicted from rig tests on a single liner.

2.5 Fuel Injection

Liquid fuels need to be atomized into many droplets since they are not usually volatile enough to produce vapour in the amounts required for ignition and combustion. The fuel droplets size plays a vital role in the ignition performance and the spray qualities also influence the stability limits, combustion efficiency and pollutant emission levels [35]. If the fuel droplets are smaller than about 10 microns, they will evaporate quickly and are unable to sustain stable combustion. If, on the other hand, they are greater than approximately 200 to 250 microns, fuel will remain partially unburned and pass to exhaust in the form of smoke. Thus the chosen fuel injection method is of great importance [27].

Liquid fuels need to be well mixed with air before combustion and so, there are two main methods of doing this and delivering it to the combustor: fuel spray nozzles and vaporizers [35]. Both methods will be briefly described in this section.

2.5.1 Fuel Spray Nozzles

In this method, liquid fuels are atomized and well mixed with air before combustion. Atomization can be described as a process where bulk fuel is converted into small drops. For this to happen, a liquid jet or sheet of fuel needs to be disintegrated by the kinetic energy of the liquid itself or by exposure to high-velocity air or gas [9, 35]. Three main types of fuel spray nozzles will be described: pressure atomizers, air-assist atomizers and airblast atomizers.

2.5.1.1 Pressure atomizers

One of the most common methods of fuel atomization is forcing the fuel under pressure to pass through a specially designed orifice. Pressure atomizers rely on the conversion of pressure into kinetic energy so that the fuel achieves a relatively high velocity compared to the surrounding air. The simplest way of doing this is passing the fuel through a plain circular orifice. If the liquid pressure is low, it will emerge as a thin distorted pencil, but if the fuel pressure exceeds the ambient pressure by about 150kPa, a high-velocity jet is formed and fuel quickly disintegrates and a well-atomized spray is formed. Despite its simplicity, this configuration is disadvantageous for most applications since the cone spray angle obtained with it is too narrow [35].

Pressure-swirl atomizers were created to solve the problem mentioned above. In its simplest form, it is called a simplex atomizer. Basically, fuel is fed into a swirl chamber through tangential holes that will give the fuel a high angular velocity. Once the fuel exits the orifice under axial and radial forces, it will emerge as a hollow conical sheet. Even though the cone spray angle is now fixed there is still a major drawback to this atomizer configuration. It is difficult to obtain a good atomization over a wide range of fuel flow. If the atomizer orifice is made small to ensure good atomization at low fuel flow rates, then at high fuel flow rates the fuel pressure required will be excessive. If the orifice is made large then at low fuel flow rates and low fuel pressures, atomization will be unsatisfactory [35].

The solution to this problem comes with the dual-orifice atomizer or duplex nozzle. This type of atomizer has been widely used on many types of engine aircraft, like the CFM56-3 as shown in Figure 2.16. It consists of two simplex nozzles that are fitted concentrically, i.e., the dual-orifice atomizer contains two swirl chambers, one of which, the primary (or pilot), is placed concentrically inside the other, the secondary (or main). At low fuel rates, the fuel is supplied solely to the primary orifice, which is made small to deal with low-pressure fuel. As the fuel pressure and fuel flow rate increase, a valve opens and fuel is also passed to the secondary orifice, which is much larger and can handle higher-pressure fuels. This way, a high-quality optimization is obtained over a wide range of fuel flow rates [35].

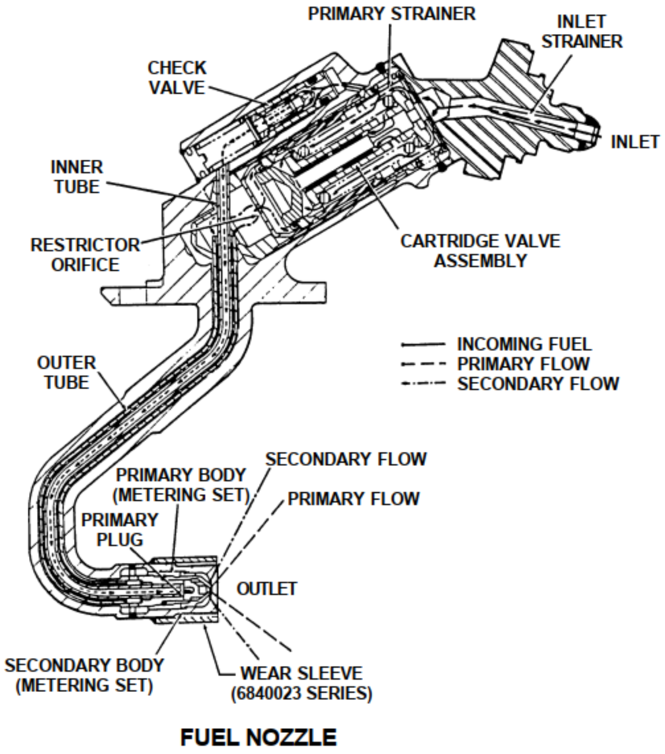

Figure 2.16: CFM56-3 dual-orifice fuel nozzle [37].

2.5.1.2 Air-assist atomizers

There is another way of solving the simplex atomizer disadvantage regarding poor quality optimization over a wide range of fuel flow rates. This solution is obtained by sizing the fuel orifices for the highest fuel flow rates and then using high-velocity air jets to enhance the atomization process at low fuel flows. There are many different configurations but the internal-mixing and the external-mixing can be highlighted. This type of configuration has been used in many industrial gas turbine engines [35].

2.5.1.3 Airblast atomizers

The airblast atomizer uses the same principles as the air-assist atomizer, since both use the kinetic energy of a flowing airstream to break a fuel jet or sheet into small drops. The main difference between the two lies in the amount of air used for the processes and their atomization velocities. In the air-assist atomizer, the air supplied comes from a compressor or a high-pressure cylinder, so it is essential to keep the airflow rate to a minimum, and, since there are no restrictions, the air velocity can be made very high. On the other hand, airblast atomizers have a limited air velocity, corresponding to the pressure differential across the combustor liner. This way, larger amounts of air are required to atomize the fuel well. These large amounts of air, however, are not wasted since after atomizing they will mix with the additional air used in combustion. The quality of this configuration has led to its use in a wide range of aircraft, marine, and industrial gas turbines [35].

2.5.2 Vaporizers

An alternative to all the atomization methods mentioned above is vaporization. This method of preparation of the liquid fuel for combustion consists of heating it above the boiling point of the heaviest hydrocarbon present so that it is fully converted into vapour before combustion. One way of doing this is injecting the fuel with some air along tubes immersed in the flame. The tube walls will heat the mixture and it will emerge as a vaporized mixture of fuel and air [35].

Despite being a low-cost system and having fairly low soot formation it still has various drawbacks. There is the risk of thermal damage to the vaporizing elements and sensitivity to variations in fuel type, during the starting cycle the tubes are too cold to vaporize the mixture and, if a rapid engine acceleration occurs, the sudden addition of more fuel will overcool the tubes reducing vaporization effectiveness and combustion efficiency [35].

2.6 Combustion Chamber Performance

Combustion chambers must burn the fuel efficiently and stably over a wide range of operating conditions without suffering large pressure losses and with combustion efficiencies close to 100%. Moreover, it must relight easily and quickly if a flameout occurs. In performing these tasks, the combustor components must be mechanically reliable. The main parameters of prime importance in assessing combustion chamber performance are pressure loss, combustion efficiency, combustion intensity and combustion stability [26, 35].

2.6.1 Pressure Loss

It should be noted that any flow process is associated with pressure loss. Still, this pressure loss in a Brayton cycle means there will be a reduction in work output and cycle efficiency, so this pressure loss must be kept to a minimum. The pressure loss across the combustor consists of two different parts. One of them, the cold loss, exists simply by pushing the air through the combustor. The other one, the hot loss or fundamental loss, arises from the heat addition to a high-velocity stream. [26, 27].

The cold losses contain the losses present in the diffuser and the liner, which from an overall engine performance stance, their distinction is immaterial. But, if the combustion is being considered, it is important to distinguish them because the pressure losses in the diffuser are wasted whereas the losses in the liner are displayed as turbulence, which is beneficial for combustion and mixing. As mentioned in section 2.3.1, this leads to incompatible combustor performance requirements because low-pressure losses won't allow uniform temperature distribution at the combustor outlet due to lack of turbulence. Therefore an ideal combustor would have all the cold losses in the liner with zero pressure drop across the diffuser. Typically modern combustors have cold pressure drops ranging from 2.5 to 5% of the inlet combustor pressure [27, 35].

The hot loss or fundamental pressure loss occurs when heat is added to a flowing gas and is given by Equation 2.4, where T_2 is the inlet temperature and T_3 is the outlet temperature [35]:

$$\Delta P_{hot} = 0.5\rho U^2[T_3/T_2 - 1] \tag{2.4}$$

Looking at the equation it can be concluded that a reduction in the inlet temperature of the combustor will lead to a lower hot pressure drop. For this to be accomplished a diffuser is used, which will not only reduce the velocity of the air but also recover as much of the dynamic pressure as possible and present a smooth and stable flow [35]. Providing adequate turbulence and mixing, a total pressure drop across the combustor between 3 to 8% of the inlet pressure is induced [26].

2.6.2 Combustion Efficiency

Combustion must always achieve high levels of efficiency. If this is not accomplished, it is generally regarded as unacceptable because in a way this means that the fuel is not being fully burned and there is waste, but mainly because, consequently, this will be displayed in the form of pollutant emissions, such as UHC and carbon monoxide. This is the reason why emissions regulations call for combustion efficiencies over 99%. This happens effectively with modern aircraft engines since combustion efficiencies are practically 100% at take-off conditions. To avoid the presence of ”white” smoke efficiency must exceed 96% and at no point in the operating conditions is it lower than 90% [35].

One way of evaluating combustion efficiency is through a chemical analysis of the combustion products. If the air/fuel ratio used and the proportion of unburned elements are known, it is possible to calculate the ratio of the real energy released to the theoretical quantity available. This chemical analysis approach, however, is not easy to implement, on the one hand, because it is difficult to obtain truly representative samples from the high-velocity stream and on the other hand, the high air/fuel ratios employed make the unburnt constituents to be measured are a very small part of the whole sample. More elaborate techniques have to be developed for this approach to be applied [36].

Another way of defining combustion efficiency is the ratio of actual heat release to the theoretical heat release in a combustion chamber, as shown in Equation 2.5 [27]:

$$\eta_c = \frac{\text{Actual total head temperature rise in combustion chamber}}{\text{Theoretical total head temperature rise}} \tag{2.5}$$

The heat released in the combustion system depends mainly upon the inlet pressure and inlet temperature. Any increase in these factors at the combustor inlet will help reduce the ignition lag, and taking into account that the residence time of the fuel-air mixture is very short (of the order of a few milliseconds), this effect becomes very important. The higher the inlet temperature, the lesser the ignition lag. The inlet pressure affects the inlet velocity which in turn will affect the turbulence, enhancing the combustion efficiency [27].

From a design standpoint, it is important to relate the combustion efficiency to operating variables such as air pressure, temperature, and mass flow rate, and to the combustion dimensions. However, the complex processes taking place in the combustion zone make this impossible now. Until possible, suitable parameters to relate combustion performance to combustion dimensions and operating variables can be derived from very simplified models to represent the combustion process. One of those models uses the well-established notion that the total time necessary to burn a liquid fuel consists of the sum of the times required for fuel evaporation, mixing of the vapour with air and combustion products, and chemical reactions. So, combustion efficiency can be obtained through Equation 2.6 [35]:

$$\eta_c = f\left(\text{airflow rate}\right)^{-1}\left(\frac{1}{\text{evaporation rate}} + \frac{1}{\text{mixing rate}} + \frac{1}{\text{reaction rate}}\right)^{-1} \tag{2.6}$$

In combustion systems, the maximum rate of heat release under any given operating conditions may be governed by either evaporation, mixing, or chemical reaction, but rarely by all three at the same time. When the combustion process is in transition, however, from one regime to another, two of the three rates will determine the overall combustion efficiency [35].

2.6.3 Combustion Intensity

Combustion intensity is an indication of the heat release rate in a given space and with a certain pressure. So the size of the combustion chamber will be decided by the required heat release rate. A high combustion intensity means a smaller space [27]. So, to obtain a high power output a comparatively small and compact combustion chamber, requirements for aircraft engines, must release heat at exceptionally high rates [26].

According to Cohen et al. [36], combustion intensity can be calculated by Equation 2.7:

$$\text{Combustion intesity} = \frac{\dot{Q}}{VP} \tag{2.7}$$

Where $\dot{Q}$ is the heat release rate, V is the combustion chamber volume and P is the pressure. The combustion intensity units come as kW/m^3atm. The pressure has an exponent of unity, which is realistic for design operation conditions. But, if extreme conditions are being considered, e.g., high altitude, $P^{1.8}$ is appropriate to use in the Equation 2.7, and in that case, units would be $kW/m^3atm^{1.8}$. It is correct to say that the lower the combustion intensity is, the easier it is to design a combustor that meets the requirements needed. For aircraft engines, combustion intensity ranges between $2 - 5 \times 10^4$ kW/m^3atm [36].

2.6.4 Combustion Stability

A gas turbine combustor needs to operate in a wide range of operating conditions. This means the combustor must operate at low temperatures and pressures, as well as air/fuel ratios that lie outside the normal limits of flammability for hydrocarbon and air mixtures [35]. For this reason, it is important to understand the stability limits of the combustor regarding air/fuel ratio, air mass flow, pressure and temperature.

There are rich and weak air/fuel ratio limits over which the flame is unstable in a combustion chamber. These limits are defined for the air/fuel ratios at which the flame blows out, although instability occurs before the limit is attained. The stable region for the air/fuel ratio between the rich and weak limits is reduced with the increase in air velocity, and if the air mass flow is increased beyond a certain value, it is impossible to have a flame at all [36]. A typical stability loop is presented in Figure 2.17 where the limiting air/fuel ratio is plotted against air mass flow.

It is important to note that the stable region and rich and weak air/fuel ratio limits presented in Figure 2.17, are so for a given pressure and temperature. This happens because the stability loop is a function of pressure and temperature. If the pressure decreases, the

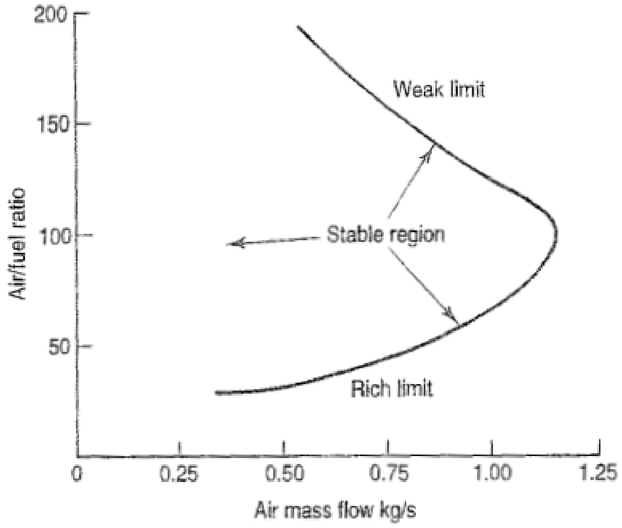

Figure 2.17: Stability loop [37].

rate at which the chemical reactions occur will decrease and hence the stability limits will narrow [36]. The same happens with air temperature, if it is increased, the stable region is extended [27]. For aircraft engines, it is important to inspect if the stability limits are wide enough at the condition of the lowest pressure, i.e., at the highest altitude [36].

2.7 Combustion Fundamentals

Combustion embraces a wide variety of processes and phenomena but it can be maybe described simply as an exothermic reaction of fuel and an oxidant. Concerning gas turbine combustors, the fuel may be liquid or gaseous but the oxidant is always air. Combustion can occur in many forms, but contrary to what one might think, not all forms are accompanied by flame or luminescence [35]. Combustion can also be described as a transformation of energy present in chemical bonds to heat, which can be used in a variety of ways [40]. The present section will focus on important aspects of combustion that are relevant to the GTE.

2.7.1 Combustion Mode and Flame Types

Two important combustion regimes can be discerned, deflagration and detonation. The regime of deflagration is characterized by the presence of a flame that propagates through the unburned mixture and it takes less than 1 ms for 80% completion. From a macroscopic viewpoint, the flame can be seen as an interface between the burned gases and the unburned mixture. All the flame processes that occur within a gas turbine combustor fall within this category. Detonation regimes cannot happen with the conventional fuel-air mixtures used in gas turbine combustors. They are characterized by a shock wave supported by a chemical reaction zone [35].

For their turn, flames can also be categorised. Although flames can propagate through a static gas mixture, it is usual to fix the flame at one point and continuously supply it with a combustible mixture. With this said, flames can either be of the premixed or the diffusion type. This classification is based on whether the fuel and air are mixed prior to the combustion or mixed by diffusion in the flame zone, respectively [35]. In other words, in a premixed flame, the fuel and oxidizer are mixed at the molecular level before any significant chemical reaction, while in a diffusion flame, the reactants are initially separated, and the reaction occurs at the interface between the fuel and the oxidant where mixing and reaction happen at the same type. In practical devices, like gas turbine combustors, both types of flame are present in various degrees [40]. Both flame types mentioned previously can further be classified depending on their prevailing flow velocities as either laminar or turbulent [35].

2.7.2 Flammability Limits

For a liquid fuel to be ignited by a discrete ignition source, the fuel must be volatilized to produce a mixture of vapour and oxidant whose composition falls within certain limits, i.e., the flame will only propagate if the composition of the mixture is inside those limits [35, 41].

If small amounts of fuel are gradually added to the oxidant (usually air), there will be a point at which the mixture becomes flammable. The percentage of fuel vapour at this point is called lean limit or weak limit. Below this point, the mixture is too lean to support a combustion reaction. If fuel continues to be added to the mixture, there will be a point at which it will no longer burn. This point in the percentage of fuel is called the rich limit. Above this point, combustion is too rich to support a combustion reaction [35, 41].

It is important to note that many variables influence flammability limits. For example, increased pressure will widen the range, especially hydrocarbon-air mixtures. This widening, however, occurs mainly at the rich limit of the range, while the weak limit is not strongly influenced by pressure. Temperature can also widen the flammability range since high initial temperatures of the mixture can enhance the flame propagation hence widening the flammability range [35, 42].

2.7.3 Mixture Ratios

The mixture ratio is an important parameter in combustion system analysis because it represents the ratio of fuel to air present in the combustion system. The mixture ratio can be expressed through several parameters depending on the type of combustion system and analysis goal. The most important ones are fuel/air ratio (or air/fuel ratio if inverted), equivalence ratio and mixture fraction. These parameters are going to be presented and explained below.

The fuel-to-air ratio, usually represented as F/A or FAR, is commonly used in the gas turbine industry and refers to the ratio between the mass of fuel, m_f, and the mass of air, m_a, as presented in Equation 2.8 [43]. It can also be calculated as the ratio between the fuel mass flow rate, $\dot{m}_f$, and the air mass flow rate, $\dot{m}_a$. The air-to-fuel ratio, represented as A/F or AFR, is obtained if inverted.

$$\mathrm{F/A} = \frac{m_f}{m_a} = \frac{\dot{m}_f}{\dot{m}_a} = \frac{1}{\mathrm{A/F}} \tag{2.8}$$

The equivalence ratio (ϕ) is a fuel-type-independent measure of the mixture ratio. It is commonly used to quantitatively indicate if a fuel-air mixture is stoichiometric (combustion stoichiometry will be explained below), rich (have more fuel) or lean (have more air) [41, 40]. It is the ratio between the actual fuel-to-air ratio and stoichiometric fuel-to-air ratio and is represented by Equation 2.9:

$$\phi = \frac{(\mathrm{F/A})_{\text{actual}}}{(\mathrm{F/A})_{\text{stoic}}} = \frac{(\mathrm{A/F})_{\text{stoic}}}{(\mathrm{A/F})_{\text{actual}}} \tag{2.9}$$

From the expression, it can be seen that if $\phi > 1$ the mixture is fuel-rich, if $\phi < 1$ the mixture is fuel-lean and if $\phi = 1$ the mixture is stoichiometric [40].

The mixture fraction (ξ) is a useful measure of mixture ratio in combustion, especially for diffusion flames. In a combustion system where the fuel stream with mass flux $\dot{m}_f$ is mixed with an air stream with mass flux $\dot{m}_a$, the mixture fraction represents the mass fraction of the fuel stream in the mixture [44]. The mixture fraction is represented by Equation 2.10:

$$\xi = \frac{\dot{m}_f}{\dot{m}_f + \dot{m}_a} = \frac{\frac{\dot{m}_f}{\dot{m}_f}}{\frac{\dot{m}_f}{\dot{m}_f} + \frac{\dot{m}_a}{\dot{m}_f}} = \frac{1}{1 + \mathrm{A/F}} \tag{2.10}$$

From Equation 2.10 it is possible to verify that in the air stream, with A/F $\longrightarrow \infty$, $\xi = 0$ and in the fuel stream, with A/F $= 0$, $\xi = 1$.

2.7.4 Stoichiometry

Physically, a stoichiometric reaction can be defined as a unique reaction in which the oxidizer present is just the amount required to burn the quantity of fuel in the combustion system completely. In other words, it can be regarded as the most economic reaction. As it was said in previous sections of this chapter if more than a stoichiometric value of oxidizer is supplied, the mixture is said to be lean and if less than the stoichiometric oxidizer is supplied the mixture is said to be rich. It is usual to write the theoretical stoichiometric reaction without formation of NO_x in terms of 1 mole of hydrocarbon fuel in reaction with air, as shown in Equation 2.11 [40, 43].

$$\mathrm{C}_x\mathrm{H}_y + \left(x + \frac{y}{4}\right)(\mathrm{O}_2 + 3.762\mathrm{N}_2) \longrightarrow x\mathrm{CO}_2 + \frac{y}{2}\mathrm{H}_2\mathrm{O} + 3.762\left(x + \frac{y}{4}\right)\mathrm{N}_2 \tag{2.11}$$

The constant 3.762 present in the Equation 2.11 comes from the ratio of approximately 79% N_2 to 21% O_2 by volume (or 77% N_2 to 23% O_2 by mass) in the air [35, 43]. This means that for every mole of oxygen necessary for combustion, 3.762 moles of nitrogen are also introduced. The nitrogen present in the air participates in combustion to produce nitrogen oxides and although it does not significantly affect the oxygen balance it has a major impact on the thermodynamics, chemical kinetics and formation of pollutants in the combustion system [45]. If combustion occurs at an air/fuel ratio lower than the stoichiometric value, oxygen will be deficient and so combustion will be incomplete. This means that unburned fuel in the form of carbon monoxide and UHC will be released from the combustion zone [35]. The stoichiometric air/fuel ratio can be determined with Equation 2.12, where M_a and M_f represent the molecular weights of the air and fuel, respectively [40, 43]:

$$(\mathrm{A/F})_{\text{stoic}} = \left(\frac{m_a}{m_f}\right)_{\text{stoic}} = 4.762\left(x + \frac{y}{4}\right)\frac{M_a}{M_f} \tag{2.12}$$

2.7.5 Enthalpy of Formation, Absolute Enthalpy and Enthalpy of Combustion

The enthalpy of formation of a substance also called the heat of formation, represented as $\Delta h^0_{f,i}$, is defined as the heat evolved when 1 mole of a substance is formed from its elements in their standard state. It can also be defined as the energy associated with the chemical bonds or the lack thereof. Generally, the standard temperature is taken to be $T_{\text{ref}} = 295.15K$ and the standard pressure is taken to be $P_{\text{ref}} = 1atm = 101325Pa$. So the standard state of an element is the stable form of that element at that temperature and pressure. By convention, it is adopted that the enthalpy of formation of elements in their standard state is zero [40, 43, 45].

The sensible enthalpy change, represented as $\Delta h_{s,i}$, is associated with the heat necessary to change the temperature of the substance from the reference (or standard) temperature to the desired temperature [45].

With the two definitions above, the absolute enthalpy of a substance can now be defined. It is the sum of the enthalpy of formation and the sensible enthalpy change. Thus, the definition of the absolute enthalpy for a substance i at a temperature T comes in the form of the Equation 2.13 [40]:

$$\bar{h}_i(T) = \bar{h}^0_{f,i}(T_{\text{ref}}) + \Delta\bar{h}_{s,i}(T) \tag{2.13}$$

Where $\Delta\bar{h}_{s,i}(T) = \int_{T_{\text{ref}}}^{T} \bar{c}_{p,i}(T^*)\, dT^*$ [45]. The subscript ref refers to the standard state, the f refers to the formation of the substance from the elements, the index ^{0} refers to all substances in their standard state and the subscript s indicates the term of the sensible enthalpy change.

With the absolute enthalpies of all the substances present in the combustion reaction, reactants and products, the enthalpy of reactants, h_{reac}, and of products, h_{prod}, can be calculated by simply adding all of the absolute enthalpies of all the reactants and products, respectively. From here, the enthalpy of combustion, or enthalpy of reaction, can be defined as the heat released in the combustion reaction. It can be determined by relating the enthalpy of reactants and products and is defined by Equation 2.14, or in terms of extensive properties by Equation 2.15 [40]:

$$\Delta h_R = h_{prod} - h_{reac} \tag{2.14}$$

$$\Delta H_R = H_{prod} - H_{reac} \tag{2.15}$$

2.7.6 Heat of Combustion

The heat of combustion, represented as Δh_c, also known as the heating value, is numerically equal to the enthalpy of combustion but with opposite sign. There are two heating values, the higher heating value (HHV) and the lower heating value (LHV). The HHV is the heat of combustion calculated when all the water in the products is assumed to condense to liquid, and this is the scenario where the most energy is released. If the water is assumed to not condense, then the LHV is determined [40].

2.7.7 Adiabatic Flame Temperature

The adiabatic flame temperature is the temperature that the flame would obtain if the net energy released by the combustion reaction were completely used for heating the products of combustion [35]. In other words, if the combustion is considered to take place adiabatically in a closed system without changes in kinetic and potential energies, the temperature attained by the products of the reaction is called the adiabatic flame temperature. It is the maximum temperature that can be achieved because any heat transfer from the acting components and incomplete combustion leads to a lower temperature of the products [43]. In practice, this happens, since there are no adiabatic close systems, and heat is lost from the flame by convection and radiation, so the adiabatic flame temperature is rarely achieved [35]. The adiabatic flame temperature can be controlled with an excess amount of air or diluent and the maximum adiabatic flame temperature for a given fuel and oxidizer is achieved with stoichiometric conditions [43]. It is worth noting that if dissociation of the products occurs, the maximum adiabatic flame temperature will not be attained because the energy absorbed in this process is considerable [35].

Depending on the combustion process conditions, there are two types of adiabatic flame temperatures: one for a constant-pressure combustion and one for a constant-volume combustion. Since GTE work under constant-pressure conditions, only the first one will be explained here. If a fuel-air mixture burns adiabatically, i.e. from Equation 2.14 $\Delta h_R = 0$, at a constant pressure than the absolute enthalpy of the reactants at the initial state (T_i, P_i) equals the absolute enthalpy of the products at the final state (T_{ad}, P_i). Thus, as shown in Equation 2.16, the adiabatic flame temperature can be calculated [40]:

$$h_{reac}(T_i, P_i) = h_{prod}(T_{ad}, P_i) \tag{2.16}$$

2.8 Emissions

2.8.1 Regulation of Engine Emissions

ICAO is a specialized agency of the United Nations responsible for regulating international civil aviation, so one of its tasks is to regulate emissions from aircraft engines with subsonic and supersonic speeds. For this reason, it was decided that the present study should consider the ICAO's regulation for emissions control under the LTO cycle. All regulations and standards regarding this matter are presented in [46].

The engine used for this study, the CFM56-3, falls into the section of ”turbojet and turbofan engines intended for propulsion only at subsonic speeds” whose manufacture date is after 1 January 1986 and whose rated thrust is greater than 26.7kN. So according to [46], the gaseous emissions (i.e. hydrocarbons, carbon monoxide and oxides of nitrogen) from the engine used for this study shall not exceed the regulatory levels determined from the following equations:

- For hydrocarbons:

$$\frac{D_p}{F_{00}} = 19.6 \tag{2.17}$$

- For carbon monoxide:

$$\frac{D_p}{F_{00}} = 118 \tag{2.18}$$

- For oxides of nitrogen

$$\frac{D_p}{F_{00}} = 40 + 2\pi_{00} \tag{2.19}$$

In Equations 2.17, 2.18 and 2.19 D_p is the mass of any gaseous pollutant emitted during the reference emissions landing and take-off cycle, F_{00} is the rated thrust and π_{00} is the reference pressure ratio [46].

Furthermore, since the CFM56-3 has a manufacturing date after 1 January 1983, it must also comply with regulations regarding the smoke. The Smoke Number (dimensionless term quantifying smoke emission, further defined in [46]) at any of the four LTO operating mode thrust settings shall not exceed the level determined from Equation 2.20:

$$\text{Regulatory Smoke Number} = 83.6(F_{00})^{-0.274} \tag{2.20}$$

Or a value of 50, whichever is lower [46].

2.8.2 ICAO's LTO Cycle

The reference emissions LTO cycle defines the thrust settings and time to be used for each mode when making smoke and gaseous emission measurements. The thrust settings and times are listed in [46]. The LTO cycle only assesses emissions below 915m (3000ft) and consists of four operating modes defined as follows and illustrated in Figure 2.18 [46]:

- Approach phase: The operating phase is defined by the time during which the engine is operated in the approach operating mode (Thrust setting: 30% of F_{00}; Time in mode: 4.0min).

- Climb phase: The operating phase is defined by the time during which the engine is operated in the climb operating mode (Thrust setting: 85% of F_{00}; Time in mode: 2.2min).

- Take-off phase: The operating phase is defined by the time during which the engine is operated at the rated thrust (Thrust setting: 100% of F_{00}; Time in mode: 0.7min).

- Taxi/ground idle: The operating phases involving taxi and idle between the initial starting of the propulsion engine(s) and the initiation of the take-off roll and between the time of runway turn-off and final shutdown of all propulsion engine(s) (Thrust setting: 7% of F_{00}; Time in mode: 26.0min).

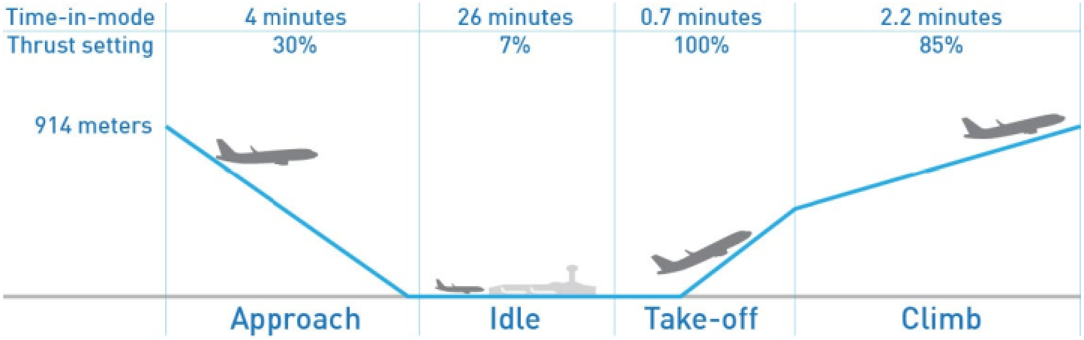

Figure 2.18: ICAO reference LTO cycle [47].

2.8.3 CFM56-3 Exhaust Emissions

Table 2.1 presents the exhaust emission data for the CFM6-3 engine under the LTO cycle, obtained from the ICAO Aircraft Engine Emissions Databank [48]. The emissions are presented as emission indexes (EIs) expressed as the mass of pollutant per mass of fuel burned.

Table 2.1: LTO cycle measurements for the CFM56-3 [48].

LTO operating mode	Fuel Flow [kg/s]	Emission Index [g/kg]			Smoke Number
		HC	CO	NO_x	
Take-off	0.946	0.04	0.9	17.7	4
Climb	0.792	0.05	0.95	15.5	2.5
Approach	0.290	0.08	3.8	8.3	2.5
Taxi/ground idle	0.114	2.28	34.4	3.9	2.2

2.9 Turbofan Engine Performance

This section will define some important parameters and their corresponding equations regarding the design performance of a turbofan engine. The first essential parameter to be defined is the engine net thrust, F. It can be calculated by simply adding the momentum thrust (i.e., the thrust obtained by the acceleration of air) to the pressure thrust (i.e., the thrust obtained when the exhaust gases are not fully expanded). In Equation 2.21 this definition for the net thrust is presented. The thrust generated's cold stream and hot stream parts are separated into different terms in the equation [36].

$$F = \dot{m}_c(v_{jc} - v_a) + A_{jc}(P_{jc} - P_a) + \dot{m}_h(v_{jh} - v_a) + A_{jh}(P_{jh} - P_a) \tag{2.21}$$

Where $\dot{m}_c$ represents the mass flow rate through the cold path, $\dot{m}_h$ represents the mass flow rate through the hot path, v_{jc} is the velocity of the cold stream, v_{jh} is the velocity of the hot stream, v_a is the velocity of the air at the engine's inlet, A_{jc} is the exit area of the "cold nozzle", A_{jh} is the exit area of the "hot nozzle", P_{jc} is the pressure of the flow at the exit of the "cold nozzle", P_{jh} is the pressure of the flow at the exit of the "hot nozzle" and P_a is the ambient pressure.

With the net thrust defined, an important parameter for indicating the relative size of engines producing the same thrust can be determined. This parameter is the specific thrust F_s and it gives this indication because the size of the engine is primarily defined by the airflow. It is defined by the ratio of thrust with mass flow rate, as presented by Equation 2.22 [36]:

$$F_s = \frac{F}{\dot{m}} \tag{2.22}$$

Where $\dot{m}$ is the total mass flow rate passing through the engine, i.e. $\dot{m} = \dot{m}_c + \dot{m}_h$.

Another important performance parameter is the thrust specific fuel consumption, $TSFC$. It is an efficiency factor that represents the fuel consumption of an engine for the thrust produced. It is the ratio between the fuel mass flow rate, $\dot{m}_f$ and the engine thrust, as shown in Equation 2.23 [27]:

$$TSFC = \frac{\dot{m}_f}{F} \tag{2.23}$$

There are several ways of analysing the engine's performance through different efficient parameters. If the efficiency of the Brayton cycle, presented in section 2.1.1, is to be studied, then Equation 2.24 should be used [36]:

$$\eta = 1 - \left(\frac{1}{r_p}\right)^{(\gamma-1)/\gamma} \tag{2.24}$$

Where r_p is the pressure ratio and γ is the ratio of specific heats.

The propulsion efficiency, η_p, relates the useful propulsive energy or thrust power to the sum of that energy and the unused kinetic energy of the jet. It is given by Equation 2.25 [36]:

$$\eta_p = \frac{\dot{m} v_a (v_j - v_a)}{\dot{m}\left[v_a(v_j - v_a) + (v_j - v_a)^2/2\right]} = \frac{2}{1 + (v_j/v_a)} \tag{2.25}$$

The energy conversion efficiency, η_e, relates the potentially useful kinetic energy with the rate of energy supplied in the fuel and is given by Equation 2.26 [36]:

$$\eta_e = \frac{\dot{m}(v_j^2 - v_a^2)/2}{\dot{m}_f LHV} \tag{2.26}$$

Lastly, with the use of the last two definitions, the overall efficiency, η_o, can be calculated using Equation 2.27, and it relates the useful work done in overcoming drag with the energy in the fuel supplied [36]:

$$\eta_o = \eta_p \eta_e = \frac{F v_a}{\dot{m}_f LHV} = \frac{v_a}{TSFC \cdot LHV} \tag{2.27}$$

Chapter 3

Fuels

3.1 Conventional Jet Fuel

Petroleum-derived fuels have always been preferred as transportation fuels due to their energy content, performance, availability, ease of handling and price [49]. The aviation industry is no exception to this rule since the vast majority of civil and military aircraft fly using a distillate of crude oil. Commercial and military aircraft with turbojet engines use what is commonly known as jet fuel, a specifically designed aviation fuel [50]. It is a blend of various kerosene hydrocarbons and the length of these is between that of gasoline and diesel. Jet fuel is preferred over gasoline because it is less volatile and denser and it is preferred over diesel since it is lighter and less likely to wax at low temperatures [51]. The chemical components of the jet fuel are alkanes, iso-alkanes, naphthenic or naphthenic derivatives and aromatic compounds. Each of these components influences the characteristics desired in the jet fuel. The high hydrogen-carbon ratio of alkanes ensures the energy density of the fuel; the naphthenes reduce the freezing point essential in high-altitude flying; and the aromatics contribute to lubricity and prevent leaks in the seals. This last one, however, should be more carefully controlled because if excessive it compromises the cleanliness of the fuel [50].

Two major kerosene-based conventional jet fuels are used in the commercial aviation industry: Jet A and Jet A-1. The former is mainly used in the USA while the latter is used in the rest of the world. These two are generally very similar except for the maximum freeze point. Jet A-1 has a lower maximum freeze point (-47°C) than Jet A (-40°C). This makes the Jet A-1 more suitable for long international flights, especially the ones on polar routes during winter [51, 52]. For military aviation, the requirements are slightly different, so different versions of jet fuel are used, namely JP-8 and JP-5. JP-8 can be defined as the military version of Jet A-1 but with more additives to improve the fuel properties. JP-5 is used in aircraft loaded on aircraft carriers and differs from the JP-8 due to its higher flash point, thus reducing the risk of fire [52, 53, 54].

This long dependency on petroleum products, however, needs to change due to several factors. On one side, the oil price has been increasing lately together with a growing concern regarding the continued availability of petroleum and the ”peak oil” debate. If nothing is done otherwise, energy security may be compromised [49]. On the other hand, and as mentioned in Chapter 1, the use of petroleum-derived fuels in the aviation industry has a major impact on climate change, specifically global warming. These concerns led the industry to seek alternative fuels or energy sources for aircraft. Since this work focuses on the analysis of the feasibility of using drop-in SAF in turbofan engines, only these will be introduced and explained. So, the present chapter will explain what SAF are, why they are the best immediate solution and present the chosen fuel to analyse and why it was chosen.

3.2 Sustainable Aviation Fuels

3.2.1 Definitions and Overview

Since hydrogen- and battery-powered aircraft are still far from becoming an immediate real solution for the large commercial aviation industry and are sustained in future breakthroughs that might overcome the present technological barriers, SAF present themselves as the best short and medium-term solution to mitigate environmental impacts of petroleum-derived fuels [10]. Although multiple definitions can be found for SAF, in a simplified way, and from the SAF Grand Challenge, they can be defined as ”drop-in liquid hydrocarbon jet fuels produced from renewable or waste resources that are compatible with existing aircraft and engines”. Most definitions from other organizations, like CAAFI or ICAO, are similar but include different nuances. Some of the nuances that can be highlighted are the need for these alternative fuels to reduce net life cycle CO_2 emissions; they should also enhance the sustainability of aviation by being superior economically, socially and environmentally; and they must enable drop-in jet fuel production from multiple feedstocks and production processes so that no changes in aircraft, engine fuel systems, distribution infrastructure or storage facilities are needed [55]. SAF is considered the best option because its main resource, biomass, in its multiple forms, is the only renewable energy source that contains carbon that can directly absorb CO_2 from air to produce organic matter. Furthermore, it is widely distributed and produced and the technology capable of converting this resource to produce liquid fuel for transportation has advanced substantially over the last few years, as seen in section 1.4 with the listed production pathways available. This way the use of biomass for SAF production can reduce the dependency on fossil fuels and decrease emissions over their life cycle due to the carbon neutrality of biomass. Finally, commercial jet fuels have high standard requirements for the physical and chemical properties, and SAF using biomass as a resource have low sulfur content, low tailpipe emissions, high thermal stability, and good cold flow properties [50].

3.2.2 Feedstock Generations

SAF can be categorised or classified according to their feedstocks into four generations. Although different authors define these generations with some variations, the following description of the generations used Wei et al. [50] and Doliente et al. [51] as references:

- The first-generation biofuels have edible food crops like oil palm, corn, sugarcane, sugar beets and wheat as their feedstock. The sugar, starch, fat and oil contents extracted from these crops are converted into jet fuel through various processes. Fats and oils are processed through the HEFA-SPK and starch and sugars use the HFS-SIP conversion method. This generation of biofuels, however, is not recommended and popular due to its drawbacks. The majority of these edible crops typically have high water and nutrient demands. Moreover, first-generation feedstock production competes with food production for land, water, and energy. The expansion to forestland for land resources is a false solution since it will create deforestation and biodiversity loss;

- The second-generation biofuels for aviation can avoid the food vs. fuel competition since they are made from non-edible biomass. These can be classified into two main groups: energy crops and waste biomass. The waste biomass can be further subdivided into agricultural and forestry residues and food and municipal waste. Typical examples of feedstocks from this generation are camelina, jatropha, used cooking oils and waste animal fats. Despite the different classifications, the second-generation feedstocks are either oil- or sugar-rich resources. Compared to the first-generation, the main difference is that the second-generation feedstock's sugar is trapped in the tough and recalcitrant lignocellulosic matrix of plant cell walls. This makes the conversion process into jet fuel a bit more complex, however, the relatively high abundance and low-use competition of lignocellulosic second-generation feedstocks makes them an appropriate long-term alternative. Using waste biomass is also beneficial because it promotes circular economies, waste management and environmental protection;

- The third-generation biofuels use algal feedstock, which is highly interesting. It contains a relatively high oil content, requires less land than many other biomass sources, has high yields, relatively low-cost requirements, and offers a solution for CO_2 sequestration. Besides, algae can grow in polluted water or water unsuitable for agriculture which simultaneously lowers operating costs and enables a solution for wastewater treatment. Furthermore, the demand for water (independent of its quality) is substantially lower than most first-generation feedstocks;

- While some authors may not yet recognize it, fourth-generation feedstocks include non-biological resources and genetically modified organisms. Genetically modified organisms, that include microalgae, cyanobacteria, fungi, and yeast, have artificially enhanced oil and/or sugar yields and negative carbon capabilities. This technology, however, is still in the early stages of research and many more studies are needed to assess the health and environmental risks that these organisms can pose. Non-biological feedstocks, e.g., CO_2, water, renewable electricity and sunlight, can become a more environmentally benign option, especially when industrial flue gases are used.

3.2.3 Advantages, Disadvantages and Challenges

To analyse the viability of using SAF to substitute petroleum-derived fuels, it is necessary to balance their advantages and disadvantages. Hence a brief enumeration of them will be presented. On the advantageous side, SAF has theoretically unlimited feedstock supply, less risk in the long term in the case of fuel spillage, and the capability of reducing net CO_2 emissions depending on the production pathway. Furthermore, it can be used as a drop-in alternative both in existing engines and distribution infrastructure and it is generally lower in contaminants like sulfur. On the other hand, there are problems associated with monocultures, like lack of biodiversity and vulnerability to pests, competition with food production if energy crops become more profitable for farmers than the food crops, harmful land-use change, and spatial and temporal boundaries (feedstocks may depend on seasons and specific conditions to grow) [51]

There are still several challenges that SAF faces regarding the scale-up and expansion into the fuel market: the lack of maturity of practically all of the conversion pathways because despite the increasing number of flights using SAF, no pathway has yet achieved the highest technological readiness level; unavailability of feedstock quantities and in the case of biofuels sustainability problems associated with the increase in its production; and insufficient support from local governments and international organizations to ease the transition to alternative fuels. If these concerns are not addressed, the economic viability of SAF will remain questioned. Decarbonization efforts will decelerate, preventing the aviation sector from achieving the set objectives [10]. One way of solving these problems is by assuming policies that act as catalysts and encourage companies to shift from fossil fuels to SAF. Financial support can decide a project's financial viability, e.g., tax exemptions or direct funding of those projects. Legislations that set specific targets for SAF integration in airports throughout the years, also promote the SAF use [10].

3.3 Gevo's ATJ

3.3.1 Background and Fuel Properties

This final section of the chapter will briefly present the chosen SAF to be compared with Jet A in the CFD analysis. Although the author could not control it, the main factor that conditioned the selection of the alternative fuel was the available information online. Even though there is plenty of information regarding SAF, it is difficult to find data regarding the detailed chemical composition of these fuels. This is needed to obtain the thermodynamic properties of the fuel to input in the species model in ANSYS Fluent (that will be explained ahead) since this software's thermodynamic database does not have any SAF. The only solution found was in the Xu et al. [56] report which presented the thermochemical properties of an ATJ-SPK produced by Gevo, Inc.. The report also presented these properties in the National Aeronautics and Space Administration (NASA) 7-term polynomial form and CHEMKIN format [57] which is the required format to introduce new species in the ANSYS Fluent thermodynamic database. The thermochemical properties of the Gevo ATJ fuel in the CHEMKIN format are presented in Appendix A.

Due to the need for alternative fuels to be drop-in, SAF properties tend to be very similar to the Jet A fuel ones. So, in Table 3.1, where the Jet A and Gevo ATJ main fuel properties are compared, it can be seen that there aren't big disparities between the two fuel properties [10, 56, 58, 59].

Table 3.1: Jet A and Gevo's ATJ fuel properties [10, 56, 58, 59].

Fuel properties	Jet A	Gevo ATJ
Approximate chemical formula	$C_{12}H_{23}$	$C_{13}H_{28}$
Molecular weight [g/mol]	167.4	184.4
Density [kg/m^3]	775-840	760
Flash point [°C]	38	50
LHV [MJ/kg]	42.8	43.9
Freezing point [°C]	-40	-78

The main property that stands out because of the difference between the two fuels is the freezing point. The Gevo ATJ has a lower freezing point which is actually beneficial since, this way, it is even less probable for the fuel to freeze at the low temperatures felt at high altitude flights.

3.3.2 ATJ-SPK Conversion Process Description

As the conversion pathway name suggests, the starting substance of this fuel production method is alcohol. Currently, only isobutanol and ethanol are considered favourable feedstocks. Still, it is expected that other alcohols like methanol, iso-propanol and long-chain fatty alcohols are approved as feedstocks for ATJ-SPK production [3]. Gevo can produce its alternative fuel from both ethanol and isobutanol, which are mainly obtained from corn [60]. Depending on the type of biomass raw material, the alcohols can be obtained from a wide range of processes. Sugar can be converted to alcohol by fermentation with yeasts or microbes; starches, for their part, should first be acidic or enzymatically hydrolysed to release sugars; and, finally, for the lignocellulosic biomass, the conversion is more complex, which can be hydrolysis followed by fermentation or thermochemical conversion, or gasification followed by fermentation [50].

The ATJ-SPK conversion method typically follows a four-step upgrading process, as can be seen in Figure 3.1. All the steps of this process have been extensively researched due to the maturity of the technology associated with alcohols. The first step is dehydration, where the removal of water yields olefins, or alkene molecules, simultaneously removing impurities from the alcohol. Next, in the oligomerization step, the alkene monomers will react to synthesize longer-chain molecules. The oligomerized product consists mainly of C_8, C_{12}, C_{16} and C_{20} oligomers and the required carbon lengths for jet fuel are between C_{14} and C_{20}. So, to produce a greater yield of jet fuel per feedstock unit, the C_8 olefins can be separated and then recycled or sent to a secondary dimerization facility. The third step will hydrogenate the oligomers to obtain a product containing the synthetic paraffinic kerosene. Finally, the last step of the process is distillation, where the jet blendstock is separated from the diesel and gasoline product streams [51].

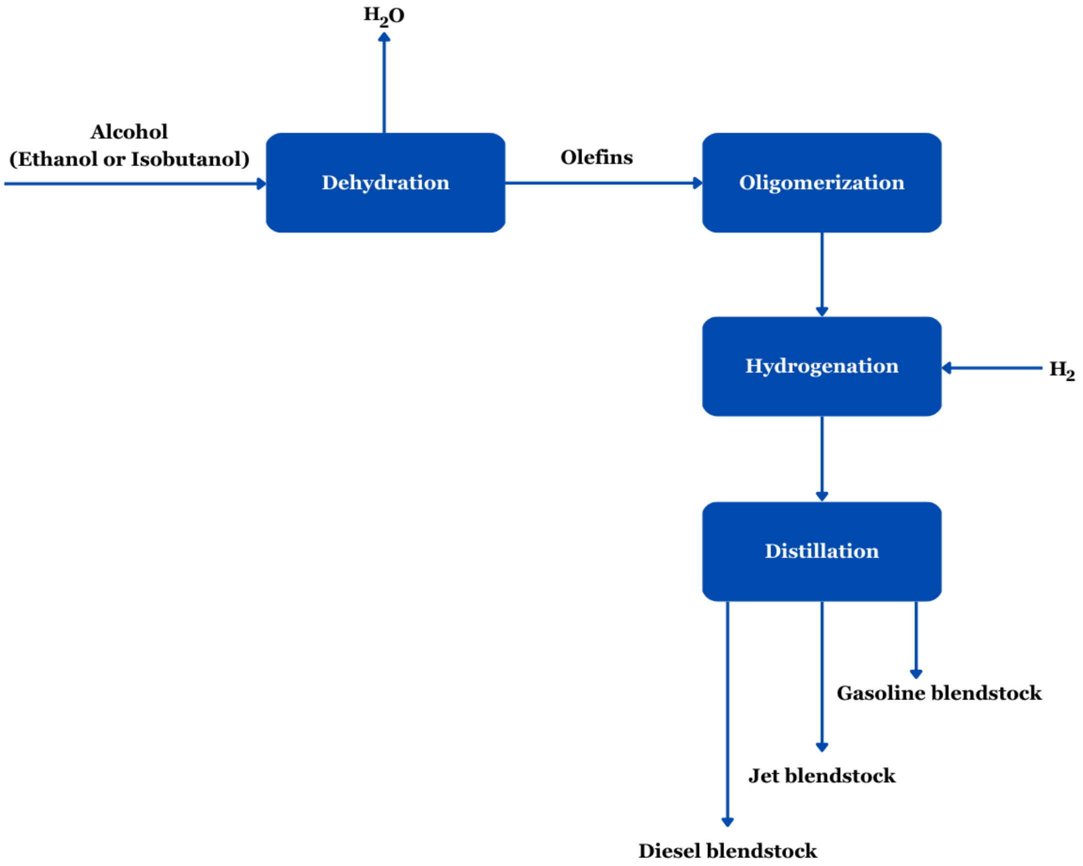

Figure 3.1: ATJ-SPK process, adapted from [50, 51].

3.3.3 Benefits and Limitations

One of the major benefits of the ATJ-SPK compared to other SAF production processes, is the fuel produced. This method, depending on the catalytic process used, can produce jet fuel with permissible aromatics content, which can be directly used in existing engines without fuel seal concerns. This way, it can be expected that certification for this type of fuel to be used without Jet A blending is to be approved in the future [7, 51]. Another advantage of this conversion process is that ethanol production is a long-established process that is at commercial production levels. Hence, the aviation industry can take advantage of the established infrastructure and construct the necessary facilities for the ATJ-SPK process close to the ethanol factories reducing transportation costs [51].

There are, however, some limitations. Currently, bioethanol is widely used as a component of automobile fuel, so the commercialization of ATJ-SPK may create competition between road and air transportation sectors in terms of feedstock availability [7, 51]. Furthermore, there are still issues with the low yields associated with bioethanol production, this way reducing profitability. So, there is still a need for more research and development of the production process to ensure a reduction in production costs and maximization of its future benefits [51].

Chapter 4

Methodology and CFD Simulation

The main objective of this work is to solve a combustion problem in which the combustion of alternative jet fuels is compared with that of conventional jet fuel. The possible approaches to solving combustion problems are theoretical methods, numerical methods, experimental methods, or any combination of these. Ideally, combustion problems should be solved theoretically and experimentally and to be economical and efficient, it is essential to apply correctly the basic principles involved in combustion phenomena [43]. In this study, the numerical and computational approaches will be used to model the combustion problem and, when possible, the results will be compared and verified with experimental data obtained from previous works.

The CFD software used for this purpose was ANSYS, a multiphysics simulation software widely used for engineering simulation across many fields. More specifically, the module Fluent was used due to its fluid flow, heat and mass transfer and chemical reactions modelling capabilities, which are adequate for solving combustion problems [61, 62].

The main tasks that need to be completed to perform a simulation in ANSYS Fluent and that are going to be described throughout this chapter are:

1. Design the geometry that represents the combustion system. As mentioned before, for this work, the geometry used was developed by de Oliveira [9].
2. Generate an appropriate mesh.
3. Define the models that will solve the combustion problem. Here, equations for fluid motion, enthalpy and chemical reactions are defined.
4. Define boundary conditions that specify, e.g., fluid behaviour and physical fluid boundaries.
5. Compare and analyse the results obtained.

4.1 Objectives, Importance and Application of Combustion Modelling

First, it is important to make some regards about combustion modelling, especially its objectives, why it became an important and powerful tool and its applicability. The main objectives of combustion modelling, according to Kuo [43] are:

- To simulate combustion processes;
- To develop predictive capability for combustion systems under various operating conditions;
- To help in interpreting and understanding observed combustion phenomena;
- To substitute for difficult or expensive experiments;
- To guide the design of combustion experiments;
- To determine the effect of individual parameters in combustion processes by conducting parametric studies.

It is important, however, to validate theoretical models by comparison with experimental results before applying them to the prediction and evaluation of the influence of certain parameters [43].

Taking these objectives into account, it becomes clear that combustion modelling through CFD simulation is a powerful and profitable tool for understanding the mechanisms and phenomena that combustion processes and determining the operating conditions and geometric parameters at the design and operating stages that allow a safe engineering practice. Contrary to simple empirical or lumped-parameter models, CFD models take into account the interaction between flow field, chemical reaction, transport phenomena and geometry occurring in combustion systems [42].

The readiness of CFD to be used for solving combustion-related problems can be assessed by its prediction capability of certain critical performance characteristics, e.g., emissions, exit temperature profiles, wall temperatures and lean blowout fuel-air ratio. To make sure that CFD is reliable in gas turbine combustion calculations, the following four steps must be taken [63]:

1. Systematic assessment of the available turbulence models against standard benchmark cases, so that the prediction availability of the solver is determined and the turbulence model is selected adequately.
2. Accurate prediction of the cold flow field in and around the combustor, i.e., the airflow through the inlet ports, the pressure, velocity and turbulence distribution, the diffusion system and the combustion system details.
3. State-of-the-art modelling of the fuel atomization system to accurately estimate the spray quality.
4. Lastly, an appropriate selection of the chemistry model and turbulence chemistry interaction model to predict the critical characteristics of chemically reacting flow within the combustor.

All these steps were followed during this work except for the fuel atomization model, which would highly increase the complexity of this already complex study. This would require a thorough study of the first and second phases of the fuel atomization system.

4.2 Turbulent Flow Analysis

Although turbulent flow combustion modelling is a vast subject area, and there is plenty to discuss, this study does not intend to conduct a rigorous review of it. So, it was decided to only summarize the available turbulence models and their most important aspects. This section will also present the selected turbulence model and why it was chosen.

4.2.1 Turbulence Models

Turbulence is characterized by irregularity or randomness, diffusion, vortices and viscous dissipation and involves a wide range of time and length scales. This makes it one of the major unsolved problems of physics and its modelling represents one of the main issues affecting the precision of numerical simulations in engineering, especially for reacting flows [64].

In theory, it is possible to resolve the whole spectrum of turbulent scales, without the need for modelling, using what is called Direct Numerical Simulation (DNS), where the Navier-Stokes equations are numerically solved in time and space. DNS, however, is not possible for practical engineering problems involving high Reynolds number flows. This method requires high computational power, so it becomes prohibitive for these types of flows and it is only applicable for low Reynolds number flows [64, 65, 66]. For this reason, it was necessary to filter out all, or at least, parts of the turbulent spectrum, by averaging the Navier-Stokes equations. One of the most used averaging procedures is time-averaging, or Reynolds-averaging, of the equations, resulting in a set of equations computationally less expensive to solve. This resulted in the appearance of two of the most used numerical simulation methods, the Reynolds Average Navier-Stokes (RANS) simulation and the Large Eddy Simulation (LES) [66]. As represented in Figure 4.1, RANS models practically all the turbulent structures while LES resolves large turbulent structures and only models the small eddies. In Figure 4.1, it can also be seen that DNS resolves the whole turbulent spectrum.

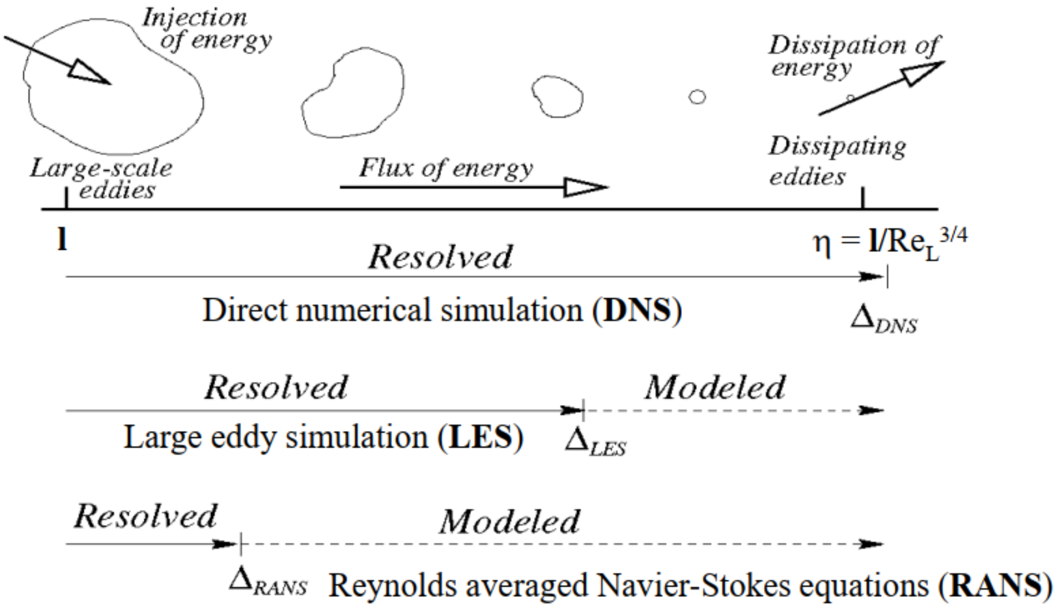

Figure 4.1: Turbulent flow simulation methods [67].

The most economic approach for computing complex turbulent industrial flows is offered by RANS models. Two different types of RANS models can be distinguished, the Eddy Viscosity Models (EVM) and the Reynolds Stress Models (RSM). The first type simplifies the problem to the solution of two additional transport equations and introduces an Eddy-Viscosity to compute the Reynolds Stresses. These models are simpler and typical examples include the k-ε and the k-ω models in their different forms. The RSM, on the other hand, are more complex and they solve an individual equation for each of the six independent Reynolds Stresses directly plus a scale equation (ε-equation or ω-equation). RANS models are suitable for the majority of engineering applications and typically provide the level of accuracy required, so there is no need for more complex models [66]

The LES is one of the most well-known Scale-Resolving Simulation (SRS) models. This alternative to RANS models resolves at least a portion of the turbulent spectrum in at least a part of the flow domain. LES, however, has to be run for a sufficiently long flow time to obtain stable statistics of the flow being modelled. This results in computational cost orders of magnitude higher than that for RANS calculations in terms of memory and CPU time [65, 66].

Taking into account all of the above, RSM was chosen over LES, because it delivers the required level of accuracy while being more economical in terms of time and computational power, which are important for this study. It was also preferred over other simpler RANS models, like k-ε models because it accounts for effects of streamline curvature, swirl, rotation, and rapid changes in strain rate (effects present in the combustor in study) more rigorously and so has the potential to give more accurate predictions [65].

Since it is not the goal of this work to thoroughly analyse the equations that govern the chosen turbulence model, it was decided not to present them here. However, they can be checked in [65].

4.3 Combustor Model

4.3.1 Geometry

As mentioned previously, the geometry used for the CFD simulations was not developed by the author of this work. Instead, the original geometry consists of a Computer-Aided Design (CAD) model of the CFM56-3 combustor developed by de Oliveira [9] during his master's thesis. For that, de Oliveira [9] had to use reverse engineering since combustor blueprints are very difficult to find, due to the confidentiality that GTE companies and manufacturers practice with their products. This means that a 3D scan of the combustor that was provided by TAP followed by a CAD design was necessary to obtain the final model.

To take advantage of the symmetry of the combustor and as it was done in previous works where this CAD model was used, only a quarter section of the combustor was used for simulation purposes. This way, simulation time can be greatly decreased while still correctly representing the four rich mixture fuel injectors present in the combustor, since for every five fuel injectors there is one that injects a richer mixture in each quarter section.

Although the original CAD model was developed by de Oliveira [9], that wasn't the CAD model used as the geometry for this work, since as it was pointed out by Domingues [39] that model had some misrepresentations of the CFM56-3 combustor that can lead to poor results. These problems were related to the position of the fuel injectors, the area of the inlets of the swirlers, the shape of the outlets of the secondary air swirlers, and the connection of these outlets to the cooling walls of the dome. With the help of technical data found on the internet, Domingues [39] could solve these issues by changing minor geometry details and so, more accurately represent the original combustor in his CAD model. So, to avoid problems in achieving good quality results, it was decided to use Domingues [39] final CAD model that more faithfully represents the CFM56-3 combustor.

The final CAD model developed by Domingues [39] is represented in Figures 4.2, 4.3 and 4.4 with all its important components such as the combustor walls, the primary and secondary swirlers, the fuel injectors and the dilution and cooling holes. The geometry presented consists only on a quarter of a section of the total combustor, as was explained before, and all the components are numbered.

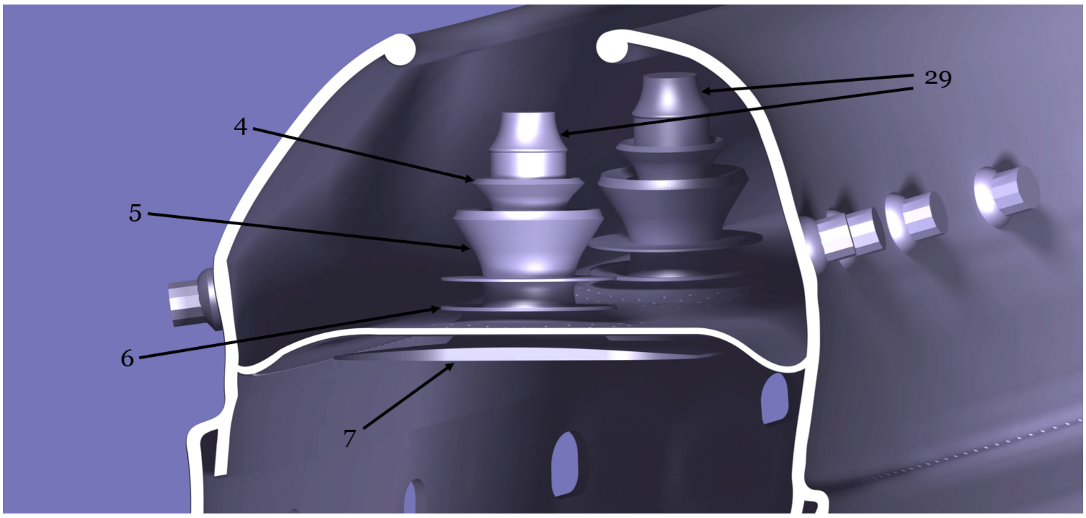

Figure 4.2: Detailed view of the CAD combustor model around the swirler.

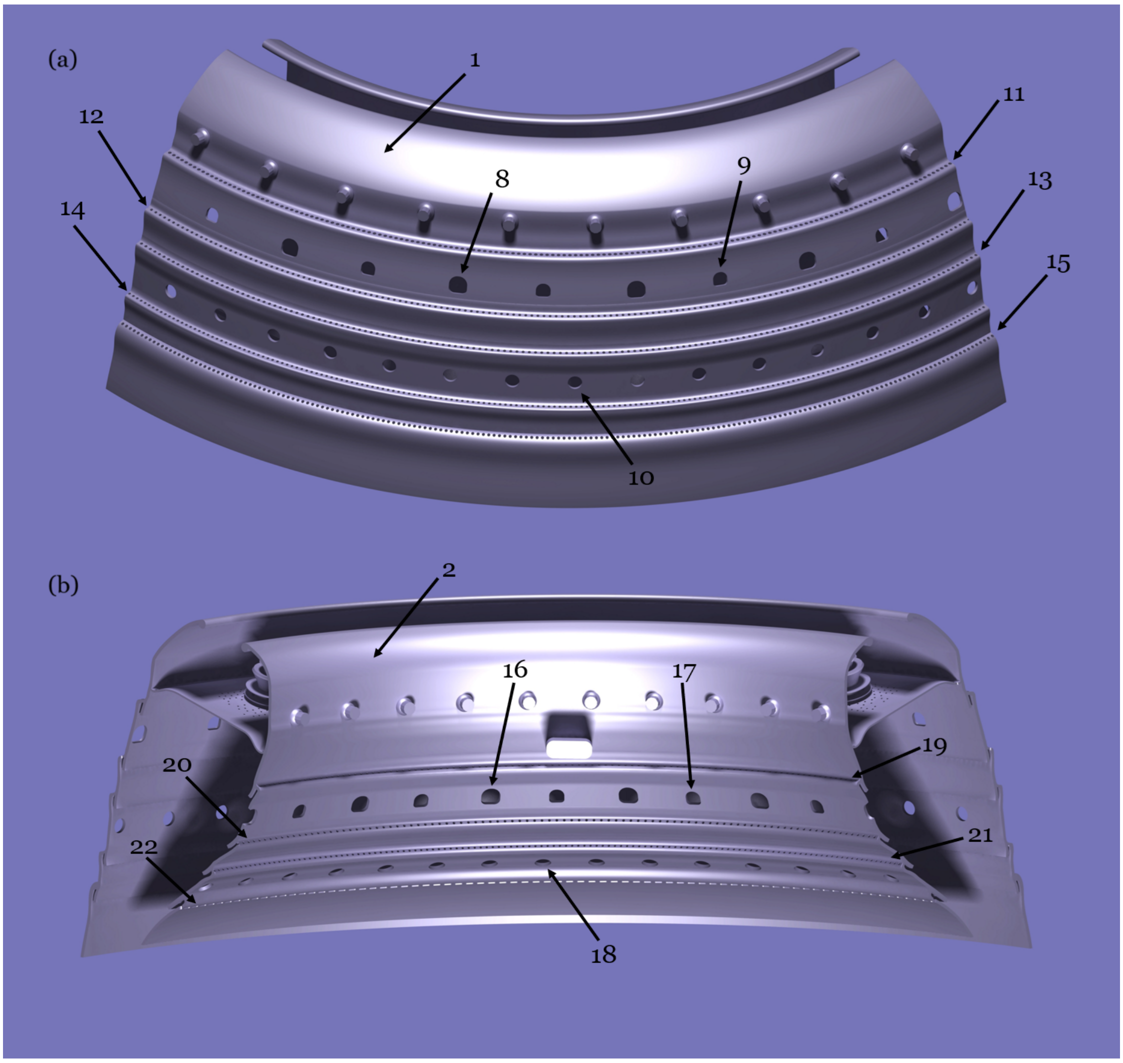

Figure 4.3: Views of the CAD combustor model: (a) outside view, (b) inner view.

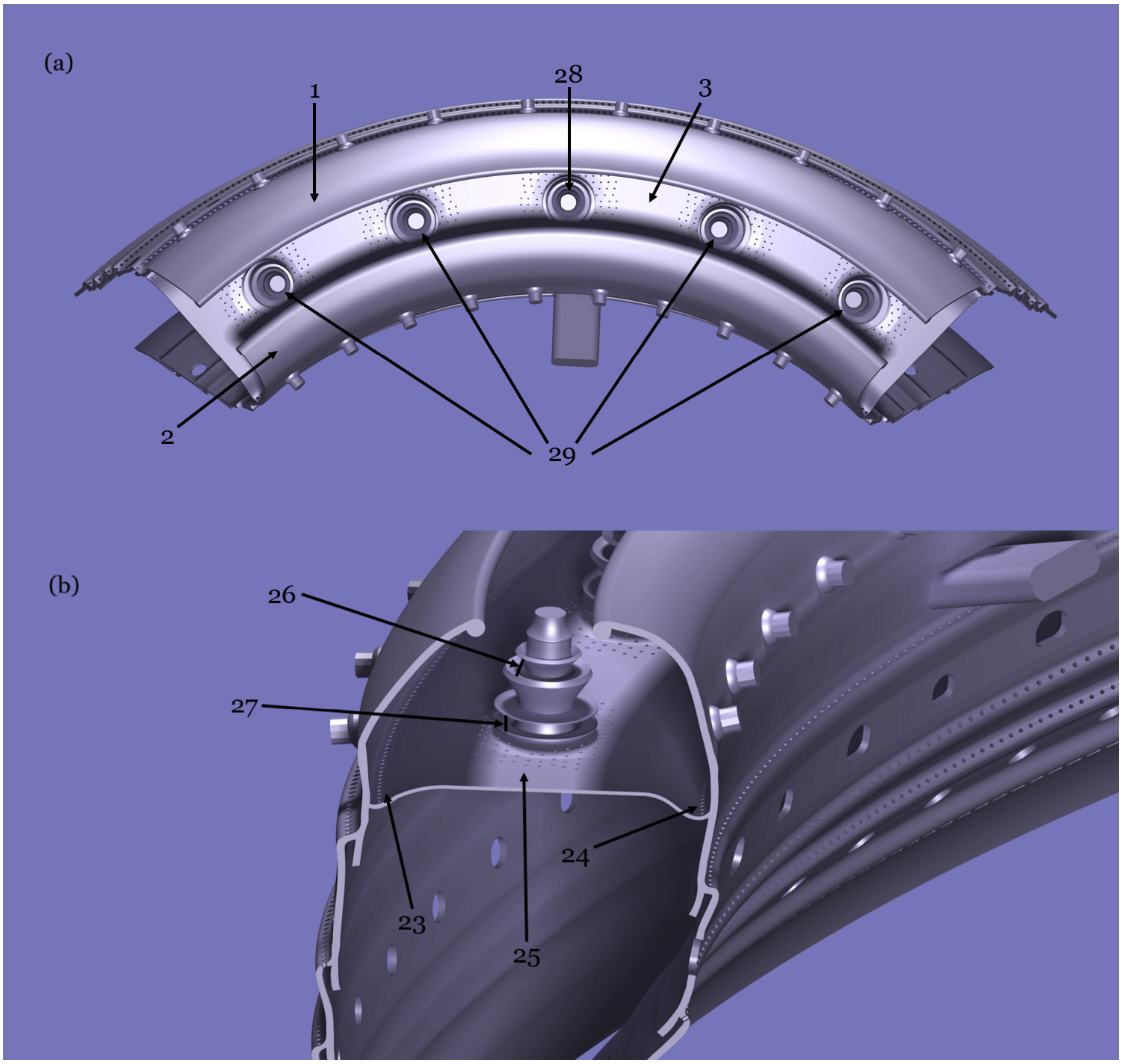

Figure 4.4: Views of the CAD combustor model: (a) top view, (b) side view.

The description of these components is presented in Table 4.1 as well as the boundary type used in the simulation associated with each component. It is worth noting that the symmetry and outlet planes are not represented in the images because they are not physical boundaries. However, these planes were created to be used in Fluent and to limit the fluid zone.

Table 4.1: CAD combustor model numbered components and their associated boundary type.

Numbered component	Component description	Boundary type
1	Exterior wall	Wall
2	Inner wall	Wall
3	Dome wall	Wall
4	Swirler’s top	Wall
5	Swirler’s middle	Wall
6	Swirler’s bottom	Wall
7	Swirler’s cooling wall	Wall
8	Primary zone big dilution holes at the exterior wall	Mass-flow inlet (air)
9	Primary zone small dilution holes at the exterior wall	Mass-flow inlet (air)
10	Secondary zone dilution holes at the exterior wall	Mass-flow inlet (air)
11	First cooling holes line at the exterior wall	Mass-flow inlet (air)
12	Second cooling holes line at the exterior wall	Mass-flow inlet (air)
13	Third cooling holes line at the exterior wall	Mass-flow inlet (air)
14	Fourth cooling holes line at the exterior wall	Mass-flow inlet (air)
15	Fifth cooling holes line at the exterior wall	Mass-flow inlet (air)
16	Primary zone big dilution holes at the inner wall	Mass-flow inlet (air)
17	Primary zone small dilution holes at the inner wall	Mass-flow inlet (air)
18	Secondary zone dilution holes at the inner wall	Mass-flow inlet (air)
19	First cooling holes line at the inner wall	Mass-flow inlet (air)
20	Second cooling holes line at the inner wall	Mass-flow inlet (air)
21	Third cooling holes line at the inner wall	Mass-flow inlet (air)
22	Fourth cooling holes line at the inner wall	Mass-flow inlet (air)
23	Exterior cooling holes line at the dome wall	Mass-flow inlet (air)
24	Interior cooling holes line at the dome wall	Mass-flow inlet (air)
25	Cooling holes around the swirlers	Mass-flow inlet (air)
26	Swirler’s primary inlet	Mass-flow inlet (air)
27	Swirler’s secondary inlet	Mass-flow inlet (air)
28	Rich mixture injector	Mass-flow inlet (fuel)
29	Poor mixture injector	Mass-flow inlet (fuel)
30	Symmetry plane	Symmetry
31	Outlet plane	Pressure outlet

4.3.2 Mesh Generation

A CFD mesh consists of multiple cells representing the portion of the fluid wanted to be simulated. This way, the mesh can provide a grid of points where the solution will be calculated. This means that the mesh generation presents itself as one of the most critical phases of a CFD simulation. A poor mesh quality can lead to poor results or even to the CFD simulation failure. It is important to note that the finer the mesh, the better the results will be, but this will also lead to a higher computational and time cost. So, it is important to find a balance.

For the mesh generation, it was decided to use the Fluent Meshing present in the ANSYS software. It was chosen because it is a user-friendly software, its generated mesh can be more easily integrated into Fluent in the following steps (solution) and with the help of the tips provided by ANSYS in [68] the mesh generated is good enough for simulation and correctly represents all the geometrical features.

4.3.2.1 Process followed for mesh size definition

One of the most faced issues in CFD simulations is what mesh resolution to consider appropriate for the case study, since, as mentioned above, this can influence the quality of the results obtained afterwards during the solution. The mesh refinement level is a complex function that depends on the flow conditions, type of analysis, geometry, and many other variables [69].

One way of finding the best grid resolution that requires the least computational cost while delivering the best possible results is to start the mesh analysis with a grid resolution and then perform a series of mesh refinements and assess the effect of this refinement in the results. This is known as a grid refinement study [69]. It is wise to start this process with the coarser possible mesh that still correctly defines all the geometrical features of the model, and then reduce grid spacing to obtain finer meshes. It is expected that as the mesh is refined and the resolution improves the obtained solution stops changing and an asymptotic value is reached, i.e., the true numerical solution is obtained. This, however, doesn't mean that the true physical solution of the equations is the same as the computed one since there may still be an error between the two [69].

This process was followed to obtain the final mesh that was used in the CFD simulations developed for this work. Every time a grid refinement was done and a mesh obtained, the quality of the said mesh was analysed and the results were compared with the previous coarser mesh. Once a good quality mesh was achieved and the results attained an asymptotic value, the final mesh was found. In the following sections, the process and the parameters used in Fluent Meshing to obtain the final mesh as well as the mesh independence test and quality mesh parameters analysed will be more thoroughly explained.

4.3.2.2 Process and parameters used in Fluent Meshing

Taking into account what was mentioned above, it was decided to create a coarse mesh firstly that captured all the features of the complex geometry of the combustor model. After this, a refinement of the mesh was performed until the results of two consecutive meshes were similar. Fortunately, it was only necessary to do one refinement, since the results of the first (coarser) and the second (finer) mesh were very close. This means that the coarser mesh could be used in the simulations. The coarser mesh has 16,180,926 cells and 47,845,867 nodes while the finer one has 21,608,962 cells and 63,370,314 nodes. The independence test and the results obtained to draw this conclusion will be presented in the next section. First, the process and the parameters used to generate the coarser mesh in Fluent Meshing will be presented.

Since the geometry model was provided to the author with all the boundaries/surfaces already separated in different parts in the *.stl* format, there was no need to convert them to a different one because Fluent Meshing can easily import them. So the generation of the mesh in this software could start.

Once the software starts, the first step is to select the Workflow type necessary to create the mesh. As in this case, the geometry is in the *.stl* format, the best-suited option is the *Fault-tolerant Meshing* since it doesn't require any previous treatment for the geometry, it can import problematic CAD geometries and facilitates the mesh generation for complex geometries. With the workflow chosen, a series of tasks have to be completed.

The first one concerns the import of the geometry into the software. So, the files just need to be uploaded, then click the *Load* button and if done correctly, it is just missing to click *Create Meshing Objects*. In the advanced options of this task, it is important to ensure that one zone is created per object.

In the second task, the Flow type chosen was *Internal flow through the object* and all the available standard and advanced options were selected as *No* except for the *Identify regions?* one. This was selected as *Yes* as it allows to define the fluid region to be meshed. Following the previous task, the third task allows the definition of the fluid region to mesh. To do that a material point inside the combustion chamber, i.e. in the fluid volume, must be selected. The easiest way to do it is to select the option *Centroid of Objects* as a method of location definition and then choose the two objects concerning the rich mixture injector and the outlet plane from the list of objects. This way the material point will be placed in the centroid of these two objects, inside the closed boundaries of the combustor model.

In the *Update Region Settings* task, for the fluid region previously created, the options *fluid*, *wrap* and *ploy-hexcore* were chosen for the *Type*, *Extraction Method* and *Volume Fill* settings, respectively. This is advised by ANSYS in [68] for complex combustor geometries.

The following task, *Choose Mesh Control Options*, allows to define local refinement levels in certain boundaries/surfaces uploaded. This way, specific parts of the geometry, like walls or inlets, can have finer or coarser cells in the mesh, as required for the solution. For that, through the *Add Local Sizing* option, the refinement methods in *Size Functions* were chosen and the refinements done. The two refinement methods used were *Curvature* and *Proximity* and in the Tables 4.2 and 4.3 all the objects refined and the parameters used for the final mesh are presented. It is important to note that the author had to go through a trial-and-error approach to get the final parameters presented in the tables. One of the main problems faced in getting the final parameters in this task was that some of the inlets, specifically the smaller ones, i.e., the cooling holes, were being incorrectly meshed.

Table 4.2: Refinement parameters used for the final mesh through the *Curvature* refinement method in the *Choose Mesh Control Options* task[2].

Objects refined	Minimum Size [mm]	Maximum Size [mm]
8, 9, 10, 16, 17, 18	1.6	5
11, 12, 13, 14, 15, 19, 20, 21	0.08	0.15
22	0.4	0.6
23, 24	0.1	0.2
25	0.05	0.1
26, 27	0.7	3.5
1, 2	0.4	1.2
3	0.7	1.5
28, 29	1.6	5
4, 5	1.1	2.2
6	1.1	2.2
7	0.9	1.5
30, 31	1.3	2.8

Table 4.3: Refinement parameters used for the final mesh through the *Proximity* refinement method in the *Choose Mesh Control Options* task[2].

Objects refined	Minimum Size [mm]	Maximum Size [mm]
8, 9, 10, 16, 17, 18	0.8	5
11, 12, 13, 14, 15, 19, 20, 21	0.08	0.15
22	0.4	0.6
23, 24	0.1	0.2
25	0.05	0.1
26, 27	0.7	3.5
1, 2	0.33	0.58
3	0.7	1.3
28, 29	0.8	5
4, 5	0.15	0.19
6	0.15	0.18
7	0.9	1.4
30, 31	1.3	2.8

---

[2] The numbering of the ”Objects refined” is the same as in Table 4.1.

For all the objects refined through the *Curvature* refinement method, the *Grow Rate* was set at 1.2, the *Curvature Normal Angle* was set at 18°and the *Scope to* setting defined as *faces-and-edges*. In the *Proximity* method, the *Grow Rate* was set at 1.2, the *Cells Per Gap* was set at 3 and the *Scope to* setting defined as *faces-and-edges* as well.

The next task is the *Generate the Surface Mesh* where the target skewness was set to 0.7 and all the other options were left as default. As the name of the task suggests, here only the surface mesh will be generated. Next, in the *Add Boundary Layers* task, and as suggested by ANSYS in [68], the number of inflation layers was set to 3 because it is proven to yield accurate results. Also on this task, the options *aspect-ratio* and *only-walls* were chosen for the *Offset Method Type* and *Grow on* settings, respectively and the *First Aspect Ratio* was defined as 10 and the *Grow Rate* as 1.2.

The concluding task is *Generate the Volume Mesh*, where the volume mesh will be generated. Here, the option *Enable Region Settings* was enabled so that the max cell length could be varied. This was the method used to change the base cell spacing so that the two meshes (coarser and finer) could be obtained. As mentioned previously, the coarser mesh was the one used for this work and the *Max Cell Length* defined for it was 5 mm. With all the parameters and options defined the final volume mesh was generated and it can be seen in Figure 4.5. In Figure 4.5 the volume mesh is presented with a clipping plane through the rich mixture injector so that the interior can be seen.

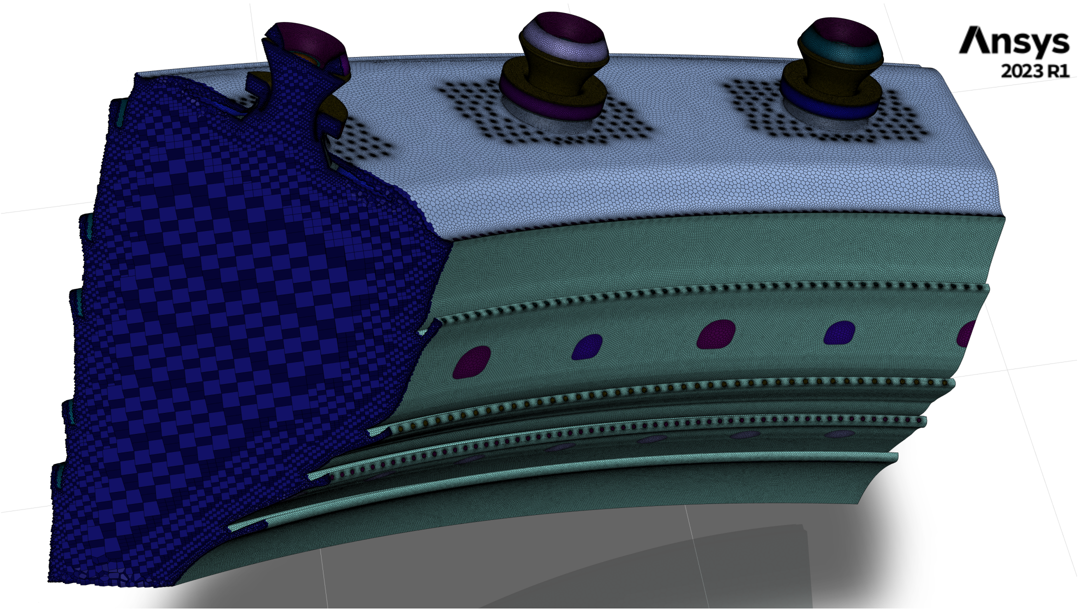

Figure 4.5: Final volume mesh generated with a clipping plane.

Figure 4.6 presents the internal structure of the final mesh generated in the cut-view plane of the rich mixture injector. In Figure 4.6 (b) a zoom in the swirler zone allows a more detailed view of the mesh and its inflation layers on the walls.

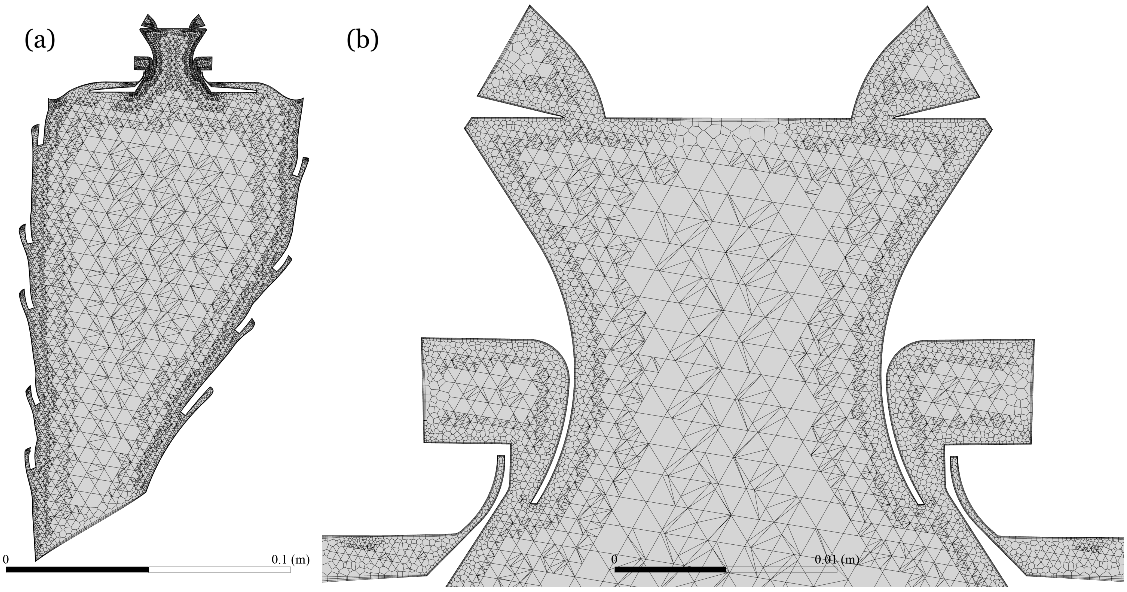

Figure 4.6: Final generated mesh internal structure: (a) in the cut-view plane of the rich mixture injector, (b) with a zoom in the swirler zone.

4.3.2.3 Mesh Independence Test

As mentioned previously, two meshes were generated (coarser and finer) to perform the mesh independence test. The available information regarding numerical and experimental data for Jet A fuel burning in the CFM56-3 combustor was found in [70] and [48], where the outlet temperature of the combustion chamber (at 100% power) and the NO_x emissions (for all the LTO cycle) are presented, respectively. Taking these into account, it was decided that the mesh independence test should be conducted at the 100%-power operating condition, where most of the boundary conditions were known, comparing and analysing the following parameters:

- Average static temperature at the outlet of the combustion chamber;
- Average static temperature and average velocity magnitude of the fluid volume, because NO_x emissions mainly depend on the temperature and residence time inside the combustion chamber [39].

In Table 4.4 the results obtained with the two meshes comparing the chosen parameters during the mesh independence test are presented. As a comparing tool, it was decided to calculate the relative error between two consecutive meshes. This means that for each chosen parameter the absolute error was divided by the result obtained with the finer mesh, as presented in Equation 4.1.

$$\text{Relative error}[\%] = \frac{|\text{Coarser mesh value} - \text{Finer mesh value}|}{\text{Finer mesh value}} \times 100 \tag{4.1}$$

Table 4.4: Compared results obtained from the two meshes used for the mesh independence test.

Comparing parameter	Average static temperature at the outlet [K]	Average static temperature of the fluid volume [K]	Average velocity magnitude of the fluid volume [m/s]
Coarse mesh	1650.09	1627.84	62.203
Fine mesh	1644.88	1600.87	61.347
Relative error [%]	0.317	1.68	1.40

In Table 4.4 it can be seen that the relative error did not surpass a value of 2% at any of the parameters and the maximum one obtained was for the average static temperature of the fluid volume, at 1.68%. On the other hand, for the average static temperature at the outlet, the relative error was very low and their values were very similar to the one reported by Ribeiro [70] in his master's thesis (1649.94 K). With these obtained values, i.e., the low relative errors, it was concluded that the refinement level of the coarse mesh did not influence the results negatively, which means the results are mesh-independent. Obviously, a higher level of refinement, i.e., continuing the grid refinement study, would lead to even lower errors between consecutive meshes, but this would inevitably lead to more computationally demanding simulations that would not yield substantially higher-quality results. This way, using the coarser mesh, some time was saved.

It is important to note that all the values in Table 4.4 were obtained using the mass flow rate reported by Ribeiro [70], to make comparisons with his reported combustion chamber outlet static temperature and so, these are not the final results for the 100%-power operating condition. However, this does not affect the independence test as only the error between consecutive meshes is important and not the obtained results.

4.3.2.4 Mesh Quality

The quality of the mesh has a very important role in the accuracy and stability of the numerical computation as a bad-quality mesh can cause convergence difficulties, bad physic description and diffuse solution. Then, it is important to check quality criteria and improve the grid if needed [68, 71].

One of the most used quality metrics is the cell orthogonal quality, which is computed using cell skewness, the vector from the cell centroid to each of its faces, the corresponding face area vector and the vector from the cell centroid to the centroids of each of the adjacent cells. This metric can range from 0 to 1, where 1 is perfect and 0 is unacceptable and is recommended to be at least higher than 0.1 [68, 71]. For the mesh generated, the minimum orthogonal quality attained was 0.062, however, this does not mean the mesh is of bad quality since this value only regards the cell with the lowest value. The average value, which is a better indicator, is 0.928 sitting itself very close to an excellent value. In Figure 4.7, a histogram presents the orthogonal quality of all the cells along the range (0 to 1).

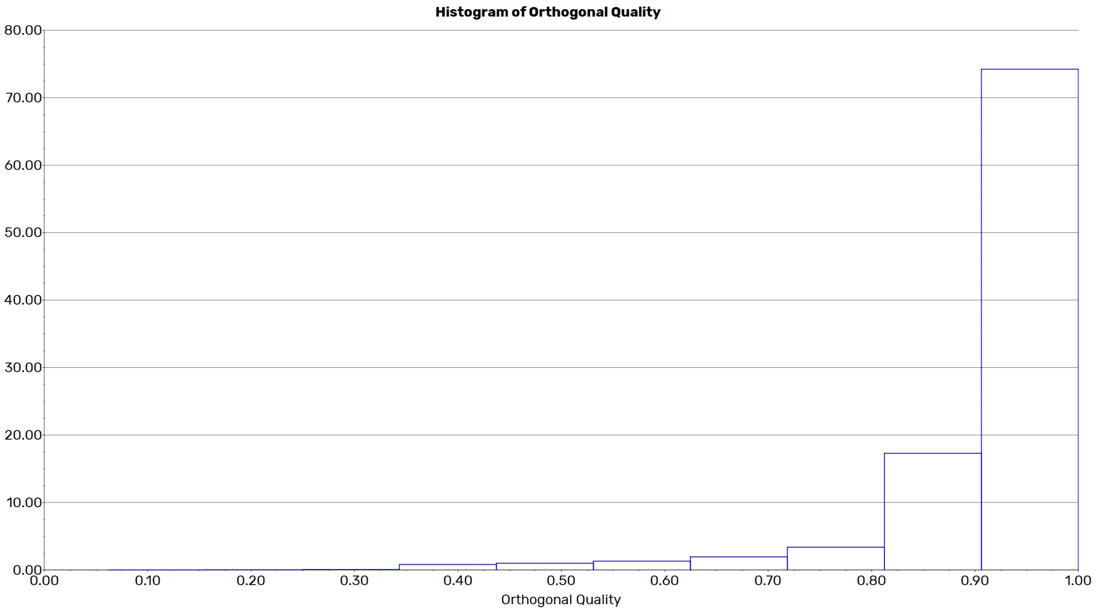

Figure 4.7: Histogram plotting the percentage of cells distributed along the orthogonal quality range.

Another important quality metric is the aspect ratio, which is a measure of the stretching of a cell. It is computed as the ratio of the maximum value to the minimum value of any of the following distances: normal distances between the cell centroid and face centroids, and the distances between the cell centroid and nodes. When meshing combustors using ANSYS, it is recommended that the aspect ratio does not surpass the value of 100 [71]. For the generated mesh in this work, the maximum value obtained for the cell with the highest one was 187, however, as it happened for the orthogonal quality, this number is not representative of the whole mesh. The average value of the aspect ratio is 6.24, which is well below 100.

A *Mesh Check* was also performed in Fluent Meshing at the end of the meshing process to ensure there were no errors. Since no errors were found, the mesh is ready to be used in the following steps of the CFD simulation.

4.4 Boundary Conditions Determination

One of the most important steps in CFD simulation is the correct boundary conditions definition since this greatly influences the convergence and especially the obtained results. As mentioned previously, GTE manufacturers and producers tend to keep technical information confidential, so parameters as simple as the air mass flow inlet are not disclosed. This way, it becomes quite difficult to obtain these parameters and how the air is distributed along the numerous inlets of the combustor.

After reviewing the different approaches to determining the boundary conditions followed by de Oliveira [9], Morão [72] and Domingues [39], it was concluded that the latter opted for the best strategy and that the first two were sometimes erroneous. So, to avoid repeating work that has already been done and to save some time during this master's thesis development, it was decided to use the same boundary conditions values and the same method to calculate them used by Domingues [39]. However, this does not mean that the parameters used were not checked and compared with the available information regarding numerical and experimental data for Jet A fuel burning in the CFM56-3 combustor, whenever possible, as it will be demonstrated. In this section, this approach for the boundary conditions determination will be explained.

In his master's thesis, Ribeiro [70] analysed the thermodynamic cycle of the CFM56-3 engine using GasTurb. So, all over his work, it is possible to obtain several important parameters in different stages of the GTE for the power condition of 100%. These include the air and fuel mass flow rates as well as some operating conditions like temperature and pressure, presented in Table 4.5. From his work, it is also possible to extract values of temperature and pressure at the inlet of the combustion chamber for other power settings. These are presented in charts and were obtained through testbed analysis.

Table 4.5: Important parameters for the 100%-power condition obtained through Ribeiro [70].

Stage	$\dot{m}_a$ [kg/s]	$\dot{m}_f$ [kg/s]	Temperature [K]	Pressure [kPa]
Combustor entry	41.451	1.1271	743.91	2343.346
Combustor exit	42.578	-	1649.94	2226.179

It was with this set of values and through an iterative process that Domingues [39] was able to determine the boundary conditions to use in this work. First, once only one-quarter section of the combustor is being modelled, it is necessary to divide by four the total mass flow rates presented in Table 4.5 and from there calculate the overall A/F, using Equation 2.8. Thus, the reference values, at the combustor's entry, used for the calculation of the boundary conditions are: $\dot{m}_{a,1/4} = 10.3628$ kg/s, $\dot{m}_{f,1/4} = 0.2818$ kg/s and A/F = 36.777. This value of overall A/F lies within the interval of typical values of the air-to-fuel ratio (between 33 and 44) for the power setting of 100%, so it can be considered a correct value [9, 39]. Theoretically speaking, the A/F in the primary zone should be at stoichiometric conditions for all power settings and the overall A/F should increase from 33-40, at 100% power, to 100, at 7% power [9, 39]. However, Domingues [39] concluded that ensuring this would lead to different air mass flow rate distributions in the inlets in percentage, for each power setting, and malfunctions for lower power settings of the combustor. So, it was decided to fix the values of the air mass flow rate percentages at each inlet through all the power conditions. To determine these percentages, Domingues [39] considered that the air mass flow rates only depended on the areas of the inlets since temperature and pressure conditions outside the combustion chamber walls were constant. All of the dilution and cooling hole areas could be determined from the CAD model, but the swirler's inlet areas were unknown, so through an iterative process and using the reference values mentioned above, the percentage of air mass flow rate through the swirlers and the walls were changed until the outlet combustion temperature was the same as the one reported by Ribeiro [70]. In this process, the fuel mass flow rate was divided equally by the five fuel injectors, except for the rich fuel injector which injected 10% more fuel [9].

After concluding this iterative process, Domingues [39] deduced that the air mass flow rate that passed through the swirlers was approximately 21% which checks with the work done by Smith and et al. [73] with similar engines. As mentioned in section 4.3.2.3, during the mesh independence test, the author decided to use the mass flow rates reported by Ribeiro [70] and the distributions of air mass flow rates calculated by Domingues [39] in his iterative process. This way, it was possible to verify that these percentages were correctly determined since the outlet combustor temperature obtained in the mesh independence test was very similar to the one reported in [70].

Since ICAO [48] reports the fuel mass flow rates for the four studied power conditions, and because the one for 100% power is different from Ribeiro [70], it was decided to redo the simulation for the full power condition but keeping the air mass flow rates percentage distribution calculated previously. This way, all the boundary conditions are defined for the 100% power condition. It is now only missing the boundary conditions definition for the lower power conditions.

As mentioned previously, Ribeiro [70] presents charts with the temperature and pressure at the combustor entry collected in testbed analysis for all power conditions. So, assuming that in his work idle corresponds to 7% power, it is possible to make good guesses for temperature and pressure for that condition. The values collected are: $T = 450$ K and $P = 354637.5$ Pa. Furthermore, from Smith and et al. [73] it is possible to verify that this type of engine, at idle, usually works with the primary zone at a stoichiometric condition. So, assuming this, using the values for temperature and pressure mentioned, the fuel mass flow rate reported by ICAO [48] and the air mass flow rate percentage distribution, Domingues [39] could determine the overall A/F and define all the boundary conditions for the condition of 7% power.

With all the information gathered until this point, it is possible to interpolate through linear regression the operating parameters, i.e., pressure, oxidizer temperature and overall A/F for the power conditions of 30% and 85%. Then, with the overall A/F and the fuel flow, it was possible to determine the total air mass flow that enters the combustion chamber for each of these power conditions. This way, all the operating parameters and boundary conditions are calculated for all the power settings to be studied. This parameters are presented in Tables 4.6 and 4.7.

In Table 4.6, the fuel temperature was considered to be 298.15 K and the same for all power conditions as this is the value assumed by the GasTurb software. This way, it is following the work done by Ribeiro [70]. Regarding the fuel pressure, it was considered to be twice the operating pressure value inside the chamber [39].

Table 4.6: Operating parameters for the LTO power settings obtained by Domingues [39].

Operating parameter	Power setting [%]			
	100	85	30	7
Air inlet pressure [Pa]	2343346	2022587	846468.6	354637.5
Air outlet pressure [Pa]	2226179	1921457	804145.2	336905.6
Air pressure variation [Pa]	117167.3	101129.3	42323.43	17731.88
Air temperature [K]	743.91	696.51	522.69	450
Fuel pressure [Pa]	4452357	3842914	1608290	673811.3
Fuel temperature [K]	298.15	298.15	298.15	298.15
Overall A/F	36.7772	39.8258	57.2166	70.0000
Primary zone A/F	7.7230	8.3636	12.0156	14.7000

Table 4.7: Mass flow rates for each inlet for the LTO power settings obtained by Domingues [39].

Inlet number	Mass flow rate [%]					Air flow [%]
	GasTurb	ICAO's database				
	100%	100%	85%	30%	7%	
8	0.5334	0.4477	0.4059	0.2135	0.1027	5.147
9	0.3382	0.2839	0.2574	0.1354	0.0651	3.264
10	0.8862	0.7438	0.6744	0.3548	0.1706	8.552
11	0.5310	0.4456	0.4040	0.2125	0.1022	5.124
12	0.3753	0.3150	0.2856	0.1502	0.0722	3.621
13	0.4806	0.4034	0.3657	0.1924	0.0925	4.638
14	0.4147	0.3480	0.3155	0.1660	0.0798	4.002
15	0.4581	0.3845	0.3486	0.1834	0.0882	4.421
16	0.5155	0.4326	0.3922	0.2063	0.0992	4.974
17	0.3404	0.2857	0.2590	0.1363	0.0655	3.285
18	1.0415	0.8742	0.7925	0.4169	0.2005	10.051
19	0.1274	0.1070	0.0970	0.0510	0.0245	1.230
20	0.1659	0.1392	0.1262	0.0664	0.0319	1.601
21	0.1560	0.1309	0.1187	0.0624	0.0300	1.505
22	0.8417	0.7064	0.6405	0.3369	0.1620	8.122
23	0.3302	0.2772	0.2513	0.1322	0.0636	3.187
24	0.2472	0.2075	0.1881	0.0990	0.0476	2.386
25	0.4034	0.3386	0.3069	0.1615	0.0777	3.892
Total cooling flow	8.1866	6.8712	6.2295	3.2771	1.5760	79.000
26	0.9994	0.8388	0.7605	0.4001	0.1924	9.644
27	1.1768	0.9877	0.8955	0.4711	0.2266	11.356
Total swirler flow	2.1762	1.8265	1.6560	0.8711	0.4190	21.000
Total air mass flow	10.3628	8.6977	7.8855	4.1482	1.9950	100.000
28 (rich injector)	0.06078	0.05101	0.04271	0.01564	0.00615	-
29 (4 poor injectors)	0.22100	0.18549	0.15529	0.05686	0.02235	-
Total fuel mass flow	0.28178	0.23650	0.19800	0.07250	0.02850	-

4.5 Problem Setup

Now that the mesh is generated and the boundary conditions defined, the problem setup in ANSYS Fluent can begin. This section will explain the whole process and all the parameters used in the software. Two workstations were used to run all the cases, so two cases could be run at a time and this way some time could be saved. The first one has a 10-core processor (20 logical processors) with 96GB of random access memory (RAM) and the second is a four-computer cluster with 4 cores (8 logical processors) and 32GB of RAM each. The first one was running ANSYS Fluent 2023 R1 and the second ANSYS Fluent 2024 R2.

When initiating the software, a window named Fluent Launcher is displayed, and there, it is necessary to ensure that the options *3D* and *double precision* are checked. The latter guarantees that more accurate results are obtained but at the cost of a slower solution. In the displayed window, it was also chosen to run the simulations in parallel processes as this greatly reduces the computational time. Usually to run the simulations as efficiently as possible the number of parallel processes should equal the number of logical processors in the workstation. However, after some tests, it was decided to launch Fluent in the computer with 18 parallel processes and 24 in the cluster. In the former, this was the number of processes that allowed the fastest iteration time and in the latter, if all available logical processors were used, the workstation would become unstable.

As soon as ANSYS Fluent launches, and before starting the simulation setup, it is good practice to check the mesh quality [66]. When performing the *Mesh Check* and *Report Quality* some of the most important quality metrics will be displayed in the console. As expected, no problems were encountered and no warnings were displayed. Figure 4.8 presents the reports displayed in the console, with the same mesh quality values obtained previously in Fluent Meshing.

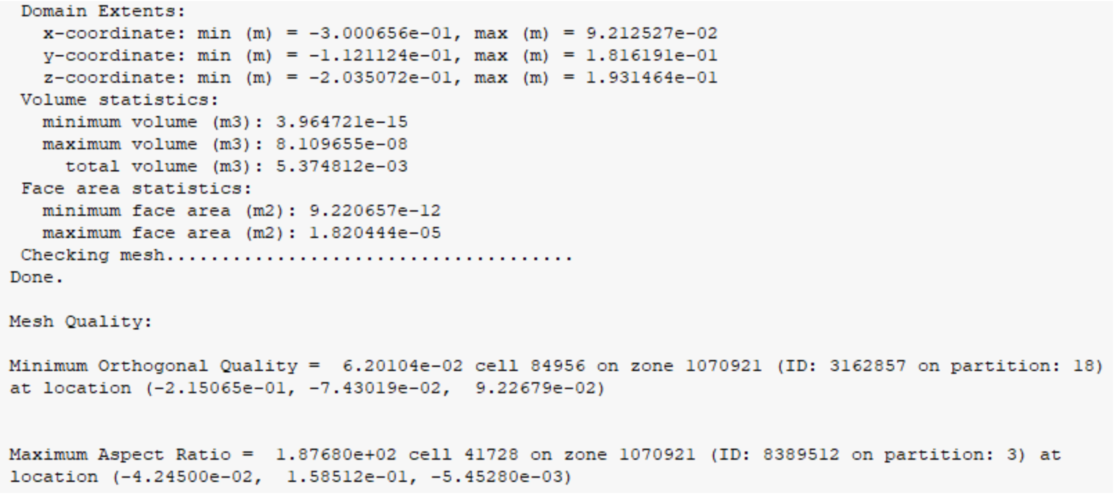

```
 Domain Extents:
   x-coordinate: min (m) = -3.000656e-01, max (m) = 9.212527e-02
   y-coordinate: min (m) = -1.121124e-01, max (m) = 1.816191e-01
   z-coordinate: min (m) = -2.035072e-01, max (m) = 1.931464e-01
 Volume statistics:
   minimum volume (m3): 3.964721e-15
   maximum volume (m3): 8.109655e-08
     total volume (m3): 5.374812e-03
 Face area statistics:
   minimum face area (m2): 9.220657e-12
   maximum face area (m2): 1.820444e-05
 Checking mesh.....................................
Done.

Mesh Quality:

Minimum Orthogonal Quality =  6.20104e-02 cell 84956 on zone 1070921 (ID: 3162857 on partition: 18)
at location (-2.15065e-01, -7.43019e-02,  9.22679e-02)


Maximum Aspect Ratio =  1.87680e+02 cell 41728 on zone 1070921 (ID: 8389512 on partition: 3) at
location (-4.24500e-02,  1.58512e-01, -5.45280e-03)
```

Figure 4.8: Reports of *Mesh Check* and *Report Quality* displayed in the ANSYS Fluent console.

4.5.1 Models Setup

Depending on the case study and the respective intended simulation, ANSYS Fluent provides an extensive selection of models to choose from. In this work, five different models were selected to solve the combustion problem. Below, a brief description of the inputs and parameters used in these models will be presented.

1. Energy model - This model must be enabled because it allows the setting of parameters related to energy and heat transfer processes inside the combustor [65, 66]. These kinds of processes are present in this case study, such as the temperature variations due to the chemical reactions.

2. Radiation model - To simulate heat transfers due to radiation, this model must be enabled. The P1 model was selected because it works reasonably well for combustion applications and it can be easily applied to complicated geometries while while requiring little computational cost [65].

3. Viscous model - As mentioned in section 4.2.1, RSM was the chosen model. When setting up the model, in the *Viscous Model* window, the submodel *Linear Pressure-Strain* was selected, the selected wall treatment was *Standard Wall Functions* and the options *Wall BC from k Equation* and *Wall Reflection Effects* were also enabled. All model constants were kept as default.

4. Species model - This model is related to the calculation of species transport and combustion [66]. The complexity and importance of this model require a more careful and thorough explanation of the parameters defined.

   Firstly, the selected model was *Non-Premixed Combustion*, as this represents the type of combustion in this study. Then, *Inlet Diffusion* was enabled as this allows to include the diffusive transport of mixture fraction through the inlets [66]. In the *Chemistry* tab, *Chemical Equilibrium* was selected as the *State Relation* and *Non-Adiabatic* as the *Energy Treatment* so that heat transfers due to chemical reactions are considered. Next, in *Model Settings*, the correct operating pressure should be introduced, according to Table 4.6 and varied with the power setting. Here it was decided to input the outlet pressure and then include the pressure variation in the inlets, as it will be later explained. For the *Fuel Stream Rich Flammability Limit* it was decided to input the value 1, as this way, ANSYS Fluent will perform calculations over the full range of mixture fraction [66]. In the same tab, it is important to choose the *Thermodynamic Database* where the thermodynamic properties of the ATJ fuel (Appendix A) were introduced.

   Then, in the *Boundary* tab, the fuel and oxidizer species and their specifications will be defined. The oxidizer, which in this case is air, was considered to be composed of nitrogen and oxygen, with mole fractions of 0.7899 and 0.2101, respectively. The fuel will be either Jet A or ATJ, depending on the case being modelled, but with a mole fraction of 1 in both cases, as these are injected alone. For the fuel and oxidizer temperatures, their values were defined according to Table 4.6 and varied with the power setting of the case being modelled.

Finally, in the *Table* tab, the *Automated Grid Refinement* was enabled and the Probability Density Function (PDF) table could be calculated. After that, the species created could be checked in *Materials*.

5. NO_x model - This model was enabled so that NO_x emissions could be predicted. It was decided to use this model in postprocessing since it is the most efficient way to use it, i.e., after the main calculations are done and the results have converged, all the other equations will be turned off [66].

   The selected pathways were *Thermal* NO_x and *Prompt* NO_x as these are the most important ones [39]. Then the fuel species should be selected from the list (either Jet A or ATJ, depending on the case). In the *Thermal* tab, *equilibrium* and *partial-equilibrium* were chosen for the [O] and [OH] models, respectively. In the *Prompt* tab, the *Fuel Carbon Number* and the *Equivalence Ratio* should be defined according to Table 4.8 depending on the type of fuel and power setting.

   Finally in the *Turbulence Interaction Mode* tab, the options *temperature*, *beta*, 30, *transported* and *global-tmax* were selected as the *PDF Mode*, *PDF Type*, *PDF Points*, *Temperature Variance* and *Tmax Option*, respectively. This way, turbulence fluctuations are taken into account [66].

Table 4.8: Important parameters to input in the NO_x model[3].

	Parameter	Power setting [%]			
		100	85	30	7
Jet A	Stoichiometric A/F	14.6	14.6	14.6	14.6
	Fuel carbon number	12	12	12	12
	Overall equivalence ratio	0.3970	0.3666	0.2552	0.2086
ATJ	Stoichiometric A/F	14.9	14.9	14.9	14.9
	Fuel carbon number	13	13	13	13
	Overall equivalence ratio	0.4051	0.3741	0.2604	0.2129

4.5.2 Boundary Conditions Definition

Once the models are defined, the next step should be setting the boundary conditions. Following Table 4.1, four types of boundaries are to be defined.

Starting with the *Mass-Flow Inlets*, in the *Momentum* tab, the *Mass Flow Rate* should be introduced according to Table 4.7 and the *Direction Specification Method* was set as

---

[3] The stoichiometric A/F was calculated using Equation 2.12 and the overall equivalence ratio using Equation 2.9. All values were calculated using ICAO's database [48].

Normal to Boundary for all inlets. A more realistic approach would require the air mass flow to enter through the swirlers using a different *Direction Specification Method*, however, after trying several methods, including the ones reported by de Oliveira [9] and Domingues [39], the result was always non-converging solutions, probably due to bad definitions of the inlet angle. So it was decided to keep the air entering as normal to the boundary, even though this might slightly influence the results. All the turbulence parameters can be changed, but it was decided to keep them as default. Since previously in the species model, the operating pressure was defined as the outlet pressure, now in the inlets, the *Supersonic/Initial Gauge Pressure* should be defined as the pressure variation of the chamber (Table 4.6) for the air inlets and with the same value of the outlet pressure for the fuel inlets (this way the inlet fuel pressure is double the operating pressure, i.e., operating pressure plus gauge pressure). Using this method, a more realistic approach is taken regarding the pressure drop that combustors deal with. In the *Thermal* tab of the *Mass-Flow Inlets*, the *Total Temperature* should be introduced according to Table 4.6 and according to the type of inlet (air or fuel). Finally, in the *Species* tab, the *Mean Mixture Fraction* should be set to 1 for fuel inlets and 0 for air inlets (as explained in the section 2.7.3).

Regarding the other types of boundaries, *Wall*, *Symmetry* and *Pressure-Outlet*, all the parameters were kept as default. This means that in the latter, the *Gauge Pressure* assumed a value of zero which means that the pressure in the boundary will be the same as the operating one (defined as the outlet pressure in the species model).

4.5.3 Solution Methods, Solution Controls and Monitors

Now that the modelling of the problem and the boundary conditions are defined, it is only left to specify and define parameters regarding the solution of the problem. Here, are included the solution methods (solver and spatial discretization schemes), the solution controls and the monitors.

For this work, it was decided to use the *Pressure-Based Solver*. It is worth noting that all simulations performed used the same parameters here mentioned. The *Pressure-Velocity Coupling* scheme used was *Coupled* since it obtains more robust and efficient single phase implementation for steady-state flows and, although it requires 1.5 to 2 times more memory, it has a higher rate of solution convergence [65, 66]. The chosen gradient method was the *Least Squares Cell Based* because it has a comparable accuracy level to that of node-based (and both superior to the cell-based gradient) but it is less expensive to compute [65]. For the *Pressure Interpolation Scheme* it was decided to use the *PRESTO!* scheme since it is the recommended one for flows with high swirl numbers, high-Rayleigh-number natural convection, high-speed rotating flows and flows in strongly curved domains [66]. For all other equations, the *Second Order Upwind* scheme was used because it yields more accurate results [66].

Next, it is necessary to define the solution parameters that control the convergence of the problem in the *Solution Controls* task page. It is usually recommended to leave this set of parameters as default since for most cases they work generally well. However, because this case study is quite complex, the default parameters are too aggressive and lead to divergence errors, e.g., *divergence detected in AMG solver: enthalpy* (a common error that appeared in this work). So these values had to be lowered so that convergence was achieved and the solution was stabilized. The final parameters defined, used for all simulations, are presented in Table 4.9. It is important to note that to reach this set of numbers it was necessary to go through a trial-and-error approach until no divergence was detected.

Table 4.9: Solution control values for *Flow Courant Number*, explicit relaxation factors and under-relaxation factors[4].

Parameter	Value
Flow courant number	2
Explicit relaxation factors	
Momentum	0.25
Pressure	0.25
Under-relaxation factors	
Density	0.2
Body forces	0.5
Turbulent kinetic energy	0.2
Turbulent dissipation rate	0.3
Turbulent viscosity	0.3
Reynolds Stresses	0.2
Pollutant no	0.95
Temperature variance	0.9
Energy	0.4
Temperature	0.4
P1	0.65
Mean mixture fraction	0.3
Mixture fraction variance	0.3

During the solution calculation, it is a common error in CFD simulations to monitor the convergence by only checking residuals. It is also important to monitor important values and parameters for the specific case (pressure, velocity, temperature, etc.), since residuals may reach the intended values and the solution may not have converged. So, for the residuals, it was used the absolute convergence criterion with the default values, i.e., all equations should decrease to 10^{-3} except for the P1 and energy equations which should decrease to 10^{-6}. Besides this, the convergence of several important values was also monitored, like: average absolute pressure, average total temperature and average velocity magnitude in the fluid volume, average static temperature and average mass fraction of NO_x in the outlet of the combustion chamber and mass imbalance. So, the solution was

---

[4] The under-relaxation factors for the *Pollutant no* and *Temperature variance* equations were only used in postprocessing.

only considered converged when the above criteria were attained.

4.5.4 Solution Initialization and Calculation

The initial guess of values at the beginning of the simulation influences the convergence velocity and stability. So, this initial set of values must be good and appropriate. For this work, the option used was *Hybrid Initialization* because it allowed to obtain a smooth and relatively quick convergence of the solution.

To ensure no errors exist within the case, i.e., in the mesh, models, boundaries or solver, it is advised to *Check Case* before running the solution. After doing this and guaranteeing no errors existed, the solution calculation is good to start.

Chapter 5

Results

In this chapter, the results obtained from the simulations of the combustion of Jet A and Gevo ATJ in the CFM56-3 combustor, for the LTO cycle, will be presented and analysed. It was performed a total of 8 simulations and their respective postprocessing (to run the NO_x model independently), with the independent mesh, of which half of them were for Jet A and the other half for the ATJ. Besides these, 2 other simulations were performed for the mesh independence test, as explained in the section 4.3.2.3.

Firstly, an example of how the convergence evaluation was done for the simulations performed, to ensure quality results, will be presented. After that, the influence of the two different fuels on some parameters inside the combustion chamber will be analysed. Then a more thorough analysis of the temperature distribution across the combustion chamber for the two fuels throughout the LTO cycle will be presented. To ensure the obtained results follow the numerical and experimental data presented by Ribeiro [70], an analysis will be done on the combustor's outlet temperature. Finally, to carry out the main objective of this master's thesis, an analysis of the emissions will be made. It will start with a comparison of the results obtained for the Jet A simulations with data published by ICAO [48]. Then the results regarding the emissions of the two different fuels will be compared.

It is worth noting that all results presented were obtained for a quarter section of the CFM56-3 combustor. Furthermore, the plots were done in Microsoft Excel and the contours were obtained using ANSYS Fluent.

5.1 Convergence Evaluation

The criteria used to analyse and ensure the convergence of the results obtained were presented in the section 4.5.3. So, taking these into account, an example of how the convergence analysis was done for all simulations, will be demonstrated in the present section. For this example, it was decided to use the ATJ simulation for the 30%-power condition.

It was previously mentioned that if the residuals decreased to a sufficient degree, one of the criteria was met. So, starting with the residuals analysis, it was noticed that for some of the simulations, the stipulated target for each of the equations' residuals was not always met. In these cases, especially for the continuity and the P1 equations, the residuals stagnated at a certain value and would not decrease any further. However, the values at which they stopped were not very far from the values they were supposed to attain. Considering this, and that the other convergence criteria were met (which will be analysed below), it was decided not to find this as problematic. In Figure 5.1 a plot of the residuals decreasing throughout the simulation is presented. This was one of the simulations in which the continuity and P1 equations' residuals did not reach the set values of 10^{-3} and 10^{-6}.

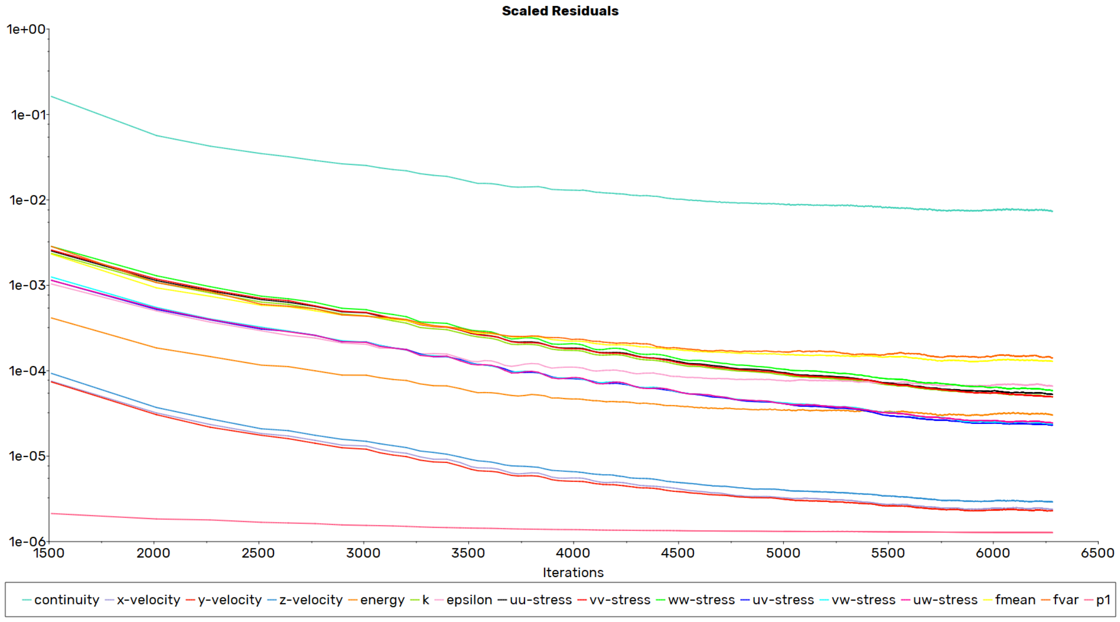

Figure 5.1: Plot of the residuals throughout the ATJ combustion simulation for the 30%-power condition.

It is important to note that in Figure 5.1, the residuals for the whole range of iterations, specifically from 1 to 1500, are not plotted because ANSYS Fluent is not able to save all the data regarding the residuals, so the older ones are gradually erased.

The second criterion to judge the solution convergence is checking if the monitored parameters defined in section 4.5.3 converge to a value. Still for the same example, i.e., for the ATJ combustion for the 30% power setting, in Figures 5.2 and 5.3 the average absolute pressure and the average velocity magnitude in the fluid volume are plotted, respectively. The other plotted parameters are presented in Appendix B in Figures B.1, B.2, B.3 and B.4. It is possible to conclude, looking at the plots, that all the chosen parameters to monitor smoothly converged to a constant value. This way, another validation of the solution convergence is given.

As a third and final criterion, the value of the mass imbalance should be ascertained to be less than 0.5% of the total mass flow through the system [9, 39]. In this case, the net imbalance was 1.57×10^{-6}, way below the defined threshold which also confirms the solution convergence.

Although not presented in this work, the convergence analysis performed for the other 7 simulations yielded similar plots and values.

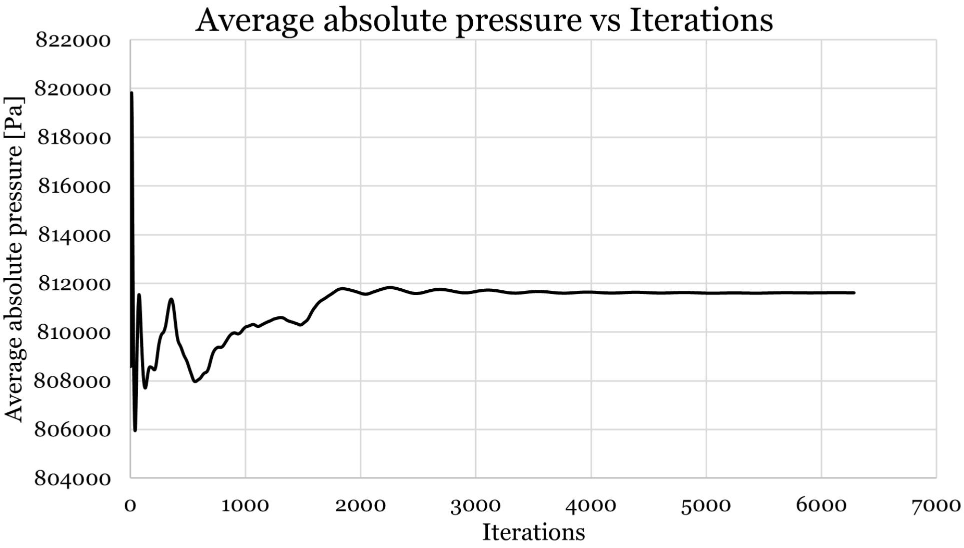

Figure 5.2: Plot of the average absolute pressure in the fluid volume for the ATJ combustion simulation at the 30% power setting.

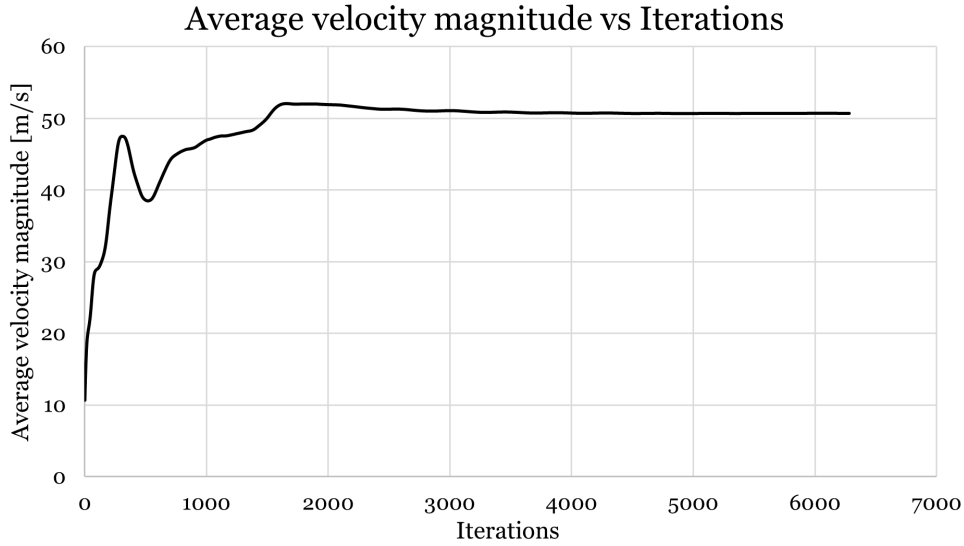

Figure 5.3: Plot of the average velocity magnitude in the fluid volume for the ATJ combustion simulation at the 30% power setting.

5.2 Fuel Change Influence in the Combustion Chamber

This section will compare some important factors inside the combustion chamber (mainly temperature and velocity magnitude) between the two different fuel combustions. The influence of the fuel change on the combustion will be analysed, with a focus on the primary zone characteristics that have a major impact on efficiency and emissions. This way, an assessment of whether the chosen SAF can be a good replacement for the conventional jet fuel can be made.

The comparison will begin with an evaluation of the static temperature distribution across the combustion chamber. For that, the contours for both fuel combustions at a power setting of 100% for this variable are presented in Figure 5.4.

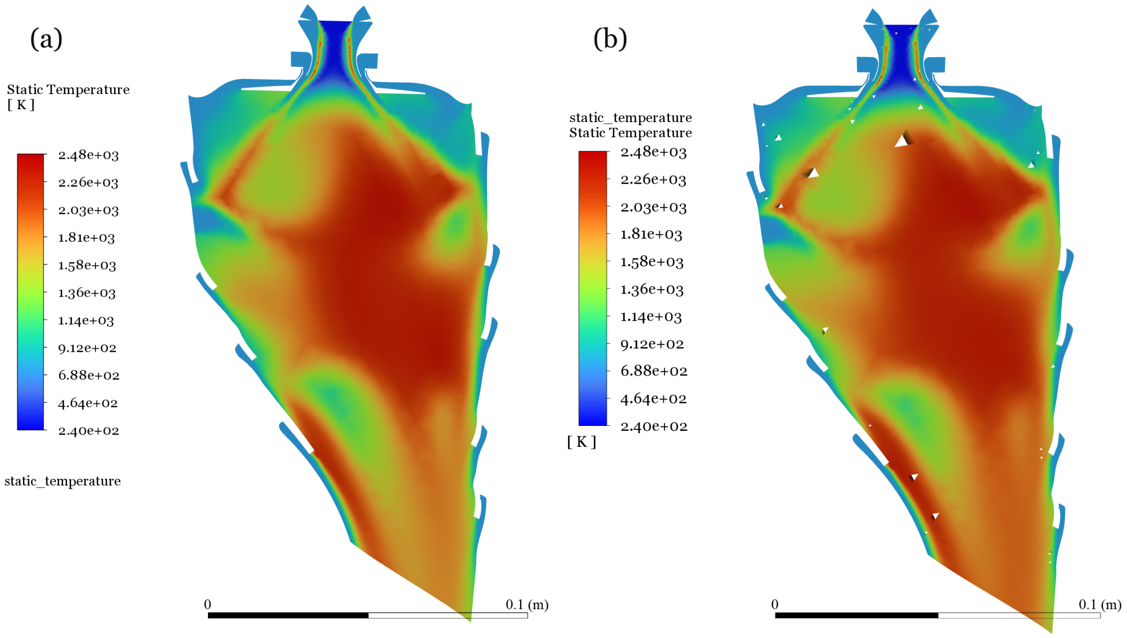

Figure 5.4: Static temperature contours at the cut-view plane of the rich fuel injector at the 100% power setting: (a) for the Jet A fuel combustion, (b) for the ATJ fuel combustion.

It becomes clear looking at Figure 5.4 that the static temperature distribution across the cut-view plane of the combustion chamber is very similar, almost identical, for both fuels. This is especially true for the primary zone where the temperature values are exactly the same and the distribution follows the same pattern for both fuels. The only noticeable difference between the two contours is located at the end of the combustion chamber, i.e., in the dilution zone. It is possible to see that for the ATJ fuel combustion, the temperature is slightly higher and it has a marginally more consistent temperature distribution across this zone. This difference, however, is so subtle that it can be disregarded. So, regarding the static temperature distribution across the combustion chamber, it can be assumed that the chosen ATJ fuel is a perfect replacement. It is important to note that in Figure 5.4 (b), the white dots dispersed in the contour are due to an error in the display done by ANSYS Fluent.

Another important parameter that should be analysed is the velocity magnitude. So, in Figure 5.5, the velocity magnitude vectors for both fuels at a power setting of 100% are presented.

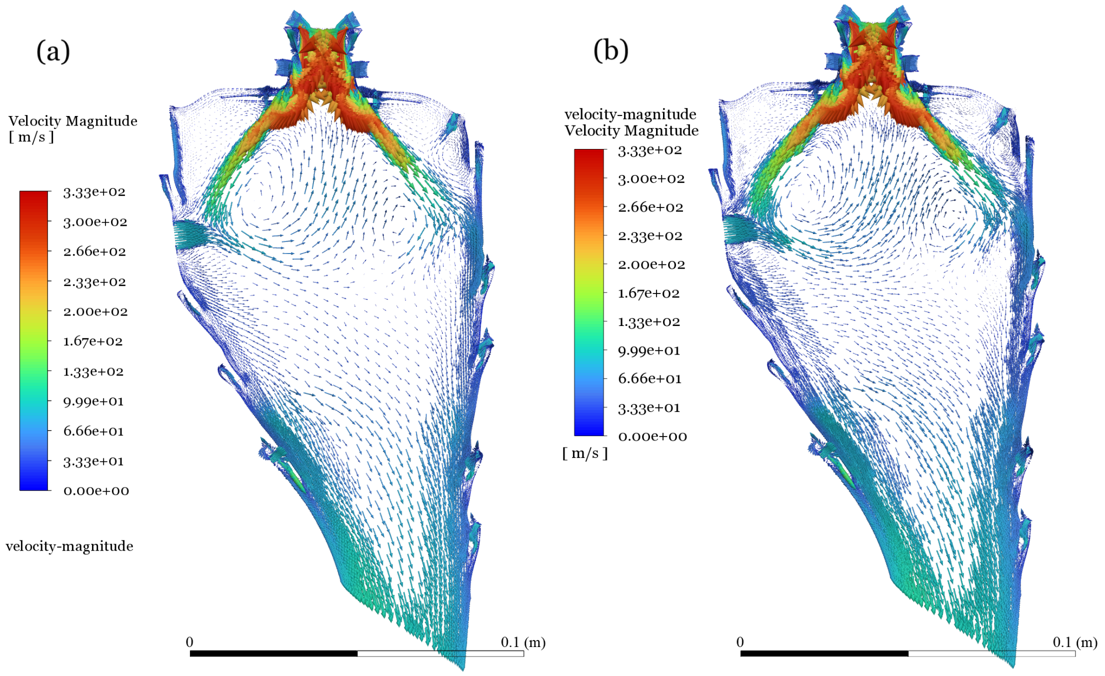

Figure 5.5: Velocity magnitude vectors at the cut-view plane of the rich fuel injector at the 100% power setting: (a) for the Jet A fuel combustion, (b) for the ATJ fuel combustion.

Once again, looking at Figure 5.5, the velocity magnitude vectors distribution across the combustion chamber for both fuels proves and sustains the affirmation previously done. No differences can be noticed comparing the two velocity magnitude fields, and so, once more, the ATJ fuel can be considered a good replacement for the Jet A fuel. It is worth noting that the velocity magnitude vector fields obtained can be a validation of the model setups done to represent the combustion of the fuels inside the chamber since it is possible to identify the recirculation zones in the primary zone. As mentioned in section 2.3.4.1 a toroidal flow reversal that recirculates the hot gases should be expected in any combustion chamber.

5.3 Temperature in the Combustion Chamber Throughout the LTO Cycle

It is also important to analyse the variation of the temperature distribution across the combustion chamber throughout the LTO cycle, i.e., the variation of the temperature along the four studied power settings. For that, Figures 5.6, 5.7 and 5.8 present the contours of the static temperature in the cut-view plane of the rich injector for the 85%, 30% and 7% power conditions, respectively. The contour for the 100% power setting was already presented in Figure 5.4. Although the temperature distribution is practically similar for the two studied fuels, it was decided to present both fuel combustion contours to compare them and emphasize how akin their behaviours are. All the presented contours have the same temperature scales so that comparison is possible between different power settings.

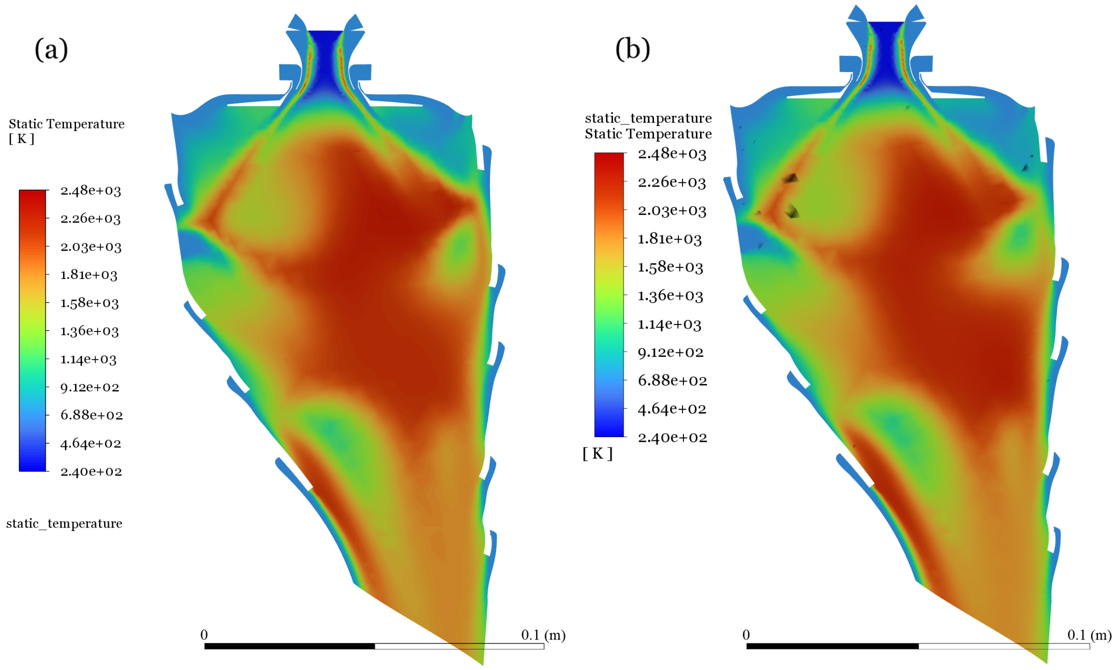

Figure 5.6: Static temperature contours at the cut-view plane of the rich fuel injector at the 85% power setting: (a) for the Jet A fuel combustion, (b) for the ATJ fuel combustion.

Looking at the presented contours of the static temperature it is possible to notice that the temperature decreases alongside the decrease of the throttle position. Although this is expected and almost obvious, since for lower throttle positions less fuel will be injected and burned, this comes as a validation of all the cases modeled and simulated. It is also possible to observe that the hottest area in the combustion chamber is always placed in the primary zone, which is also expected since this is the main zone where the combustion occurs and where the fuel is directly injected. For the cases of 100% and 85% power settings, this hot area extends a bit further, until the secondary zone, which is normal since as more fuel is being burned, harder it becomes to cool down the gases before reaching the combustor exit. Finally, it is possible to examine that the dilution and cooling of the gases are correctly modelled since the temperature decreases the closer the gases come to the combustor exit, albeit to a lesser degree for the 100% and 85% power conditions. As previously mentioned, the behaviour of the ATJ fuel combustion regarding this parameter is the same as the one of the Jet A, which makes this alternative fuel a perfect substitution, since this way no modifications are needed for the combustor. The black dots present in the contours of Figures 5.6 (b) and 5.7 (b) are also due to errors in the display done by ANSYS Fluent.

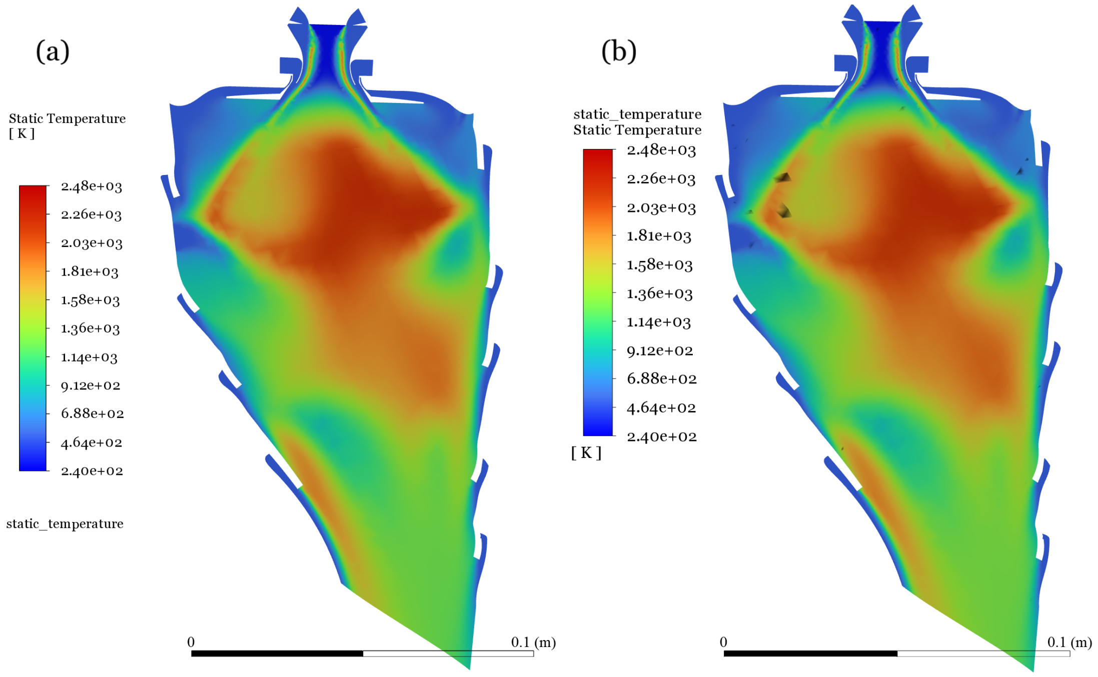

Figure 5.7: Static temperature contours at the cut-view plane of the rich fuel injector at the 30% power setting: (a) for the Jet A fuel combustion, (b) for the ATJ fuel combustion.

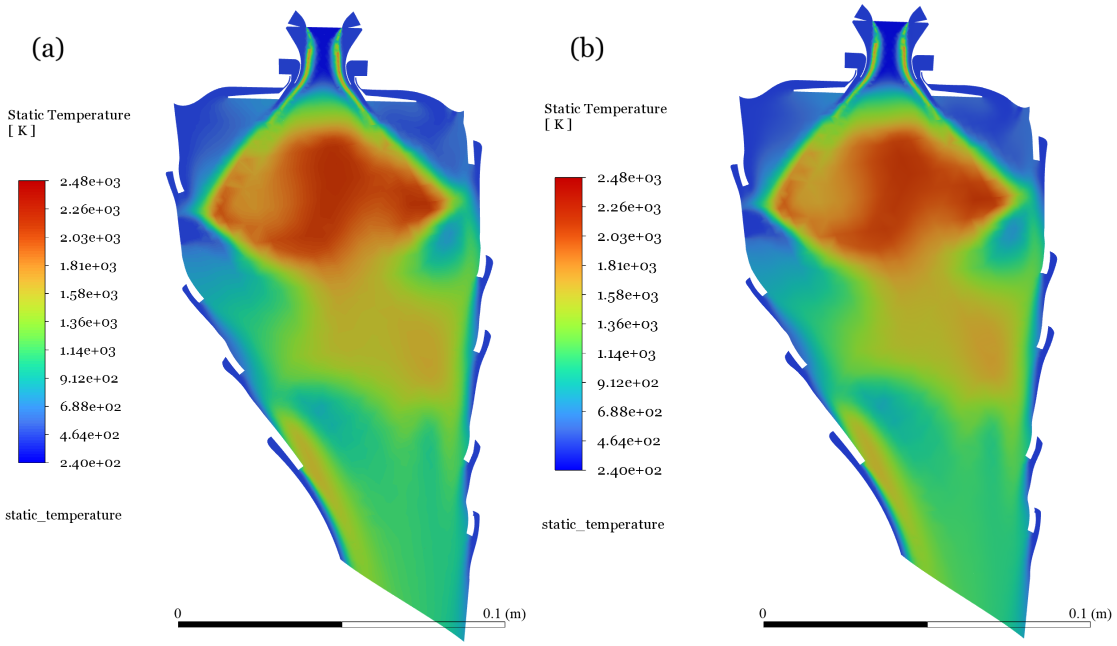

Figure 5.8: Static temperature contours at the cut-view plane of the rich fuel injector at the 7% power setting: (a) for the Jet A fuel combustion, (b) for the ATJ fuel combustion.

5.4 Combustor's Outlet Temperature

The combustor's outlet temperature is one of the most important parameters regarding the efficiency and the life expectancy of some of the GTE parts. So, this should be analysed and compared between the two fuel combustions to first assess if the models were correctly set and then if the alternative fuel behaves similarly and can replace the Jet A fuel in this regard. In this section, the exit combustor temperature obtained for the 100% power setting burning Jet A fuel will also be compared with the value reported by Ribeiro [70] and this way, serve as a validation for the results obtained in the simulations done in this work.

All the data regarding the average static outlet temperature for both fuel combustions is presented in Figure 5.9 and also in Table 5.1 since the values are very close for both combustions and are better interpreted if presented in these two distinctive matters.

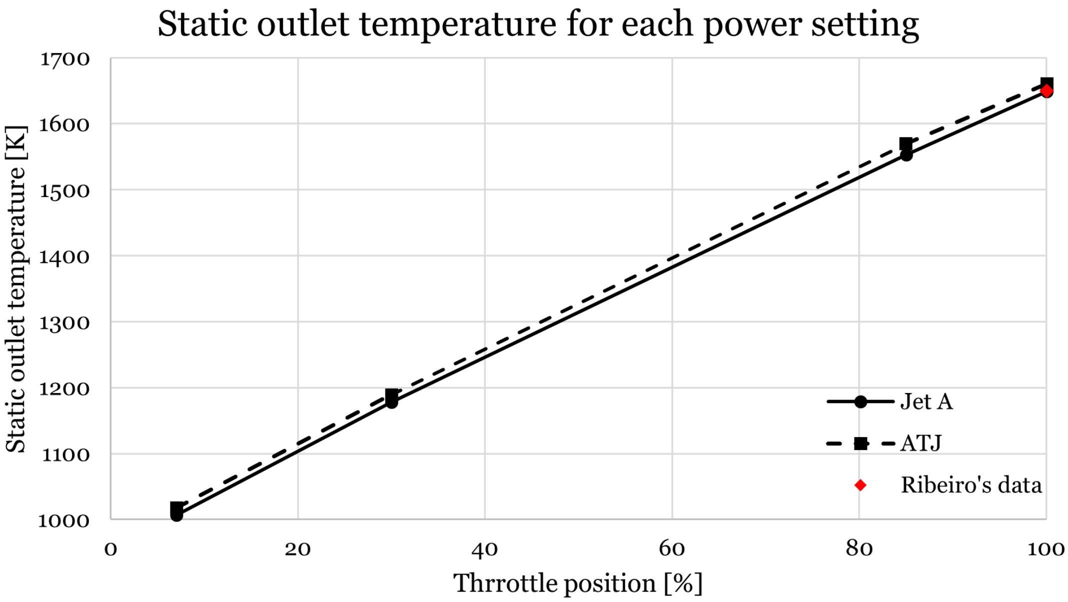

Figure 5.9: Plot of the average static outlet temperature for each power setting burning Jet A fuel and ATJ fuel as well as the reference value reported by Ribeiro [70].

Table 5.1: Average static outlet temperature for each power setting burning Jet A fuel and ATJ fuel.

	Power setting [%]			
	100	85	30	7
Average static outlet temperature burning Jet A fuel [K]	1649.08	1552.88	1178.10	1007.21
Average static outlet temperature burning ATJ fuel [K]	1660.57	1569.45	1189.52	1017.60

Looking at the data presented in Figure 5.9 and Table 5.1, specifically at the value obtained burning Jet A at full power and considering that Ribeiro [70] reported a value of 1649.94

K, the achievement of the reference outlet temperature can be considered a success and the results can be considered validated in this regard. To be more specific, for this power condition, the error was only 0.05%, which is practically null.

It is also possible to observe that for all power conditions, the outlet temperature achieved by burning the ATJ fuel is slightly higher. This is probably due to the higher LHV of the GEVO's ATJ when compared with the Jet A fuel, however, this slight temperature difference should not be problematic, since for full power (the most critical case) this parameter doesn't exceed an 11 K of difference. Although in similar works ([9] and [39]) it was decided to adjust the fuel mass flow rate of the alternative fuel, for this work it was decided to keep it the same for both fuels since they are chemically very similar. If, however, the outlet combustor's temperature is desired to be exactly the same when burning the ATJ fuel, it is only necessary to marginally reduce the quantity of fuel injected. This way, the same conditions are achieved and at the same time a fuel reduction is accomplished. This slight reduction can become significant when a broader perspective is taken into account, i.e., considering the whole quantity of fuel that an aircraft carries.

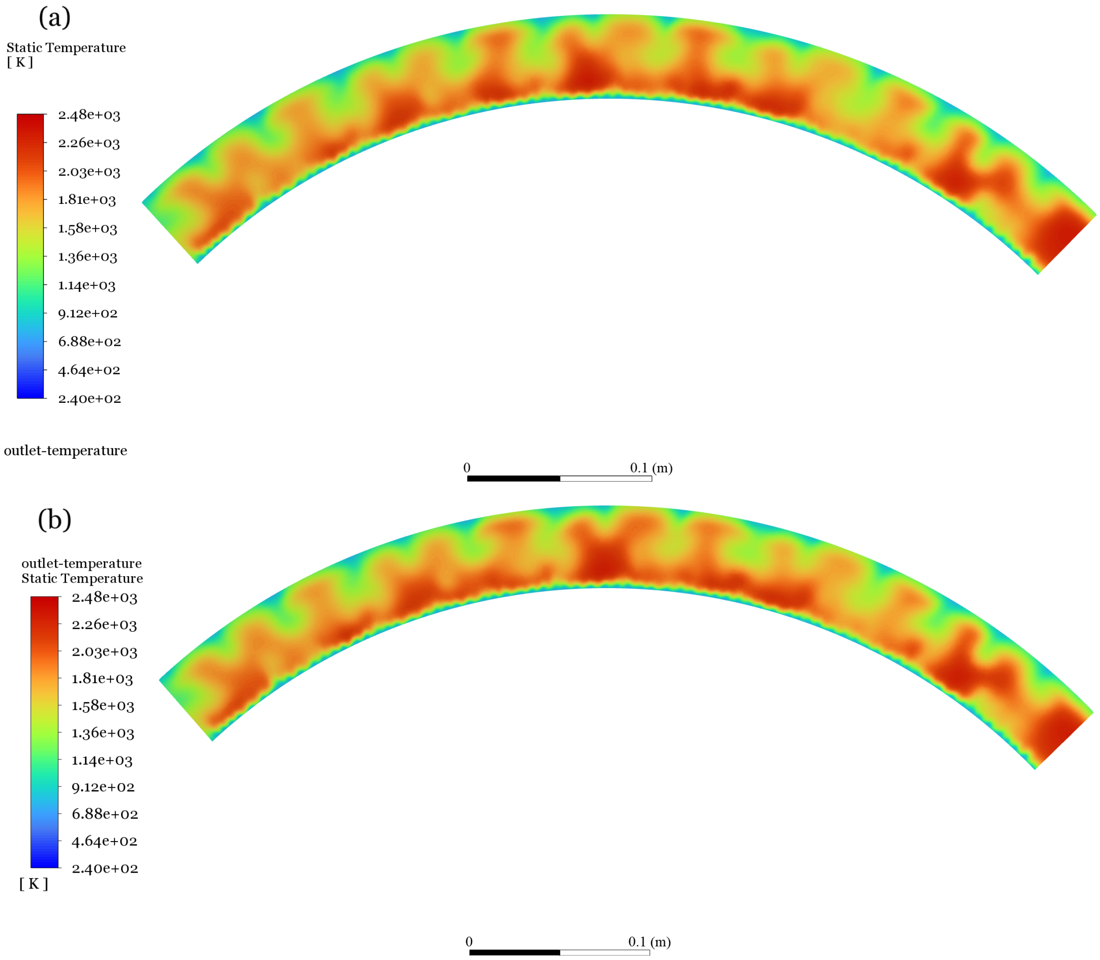

Figure 5.10: Static temperature contours at the outlet surface at the 100% power setting: (a) for the Jet A fuel combustion, (b) for the ATJ fuel combustion.

Still concerning the outlet temperature, it is pertinent to analyse the temperature profile. So, Figure 5.10 presents the contours of the static outlet temperature for both fuel combustions at full power.

It is possible to conclude looking at Figure 5.10 that for both cases the temperature is not constant and uniform along the outlet section. This is undesirable and can become problematic since the existence of these hot spots can lead to faster degradation of the turbine nozzle guide vanes and the turbine blade. The hot spots are naturally more pronounced in the rich mixture injector zone (the middle of the surface) where the combustor attains higher temperatures. This problem can be due to the non-modelling of the swirl effect which probably hinders the mixing and the complete combustion in the primary zone.

5.5 Emissions Analysis

To conclude the presentation and discussion of the results, in this section an emissions analysis will be demonstrated. Several pollutants can be studied but in this work, it was decided to analyse the emissions of NO_x and CO as ICAO presents experimental data regarding these pollutants in its database [48]. Besides these, the emissions of CO_2 will also be investigated as this is one of the main GHG, even considering that CO_2 is a natural byproduct of a complete combustion. To be able to compare the results obtained in the simulations with the ICAO data, all emissions will be presented as EIs. So, Equation 5.1 will be used to calculate them.

$$\begin{aligned}\text{EI [g/kg of fuel]} &= \frac{\text{Pollutant flow rate [kg/s]} \times 1000}{\dot{m}_f \text{ [kg/s]}} \\ &= \frac{\text{Pollutant mass fraction} \times (\dot{m}_a + \dot{m}_f) \text{ [kg/s]} \times 1000}{\dot{m}_f \text{ [kg/s]}}\end{aligned} \tag{5.1}$$

The pollutant mass fractions were obtained by reporting the area-weighted average mass fraction of each pollutant on the outlet surface in ANSYS Fluent. It is important to note that although the simulations were performed for a quarter section of the combustor, since all flow rates in Equation 5.1 are for that same quarter section, there is no need to multiply them by four because they would cancel each other. This means the results obtained from the equation can be directly compared with the ICAO data. Furthermore, it is also worth noting that the units of the EI are grams of the pollutant per kilogram of fuel burned.

5.5.1 NO_x Emissions

The main pollutant emission to be analysed is the NO_x emission, since as mentioned in section 1.1 these are one of the prime responsible for contrail formations and therefore warming effect. In Figure 5.11 the results for the NO_x EIs obtained for both fuel combustions are compared with the ICAO values.

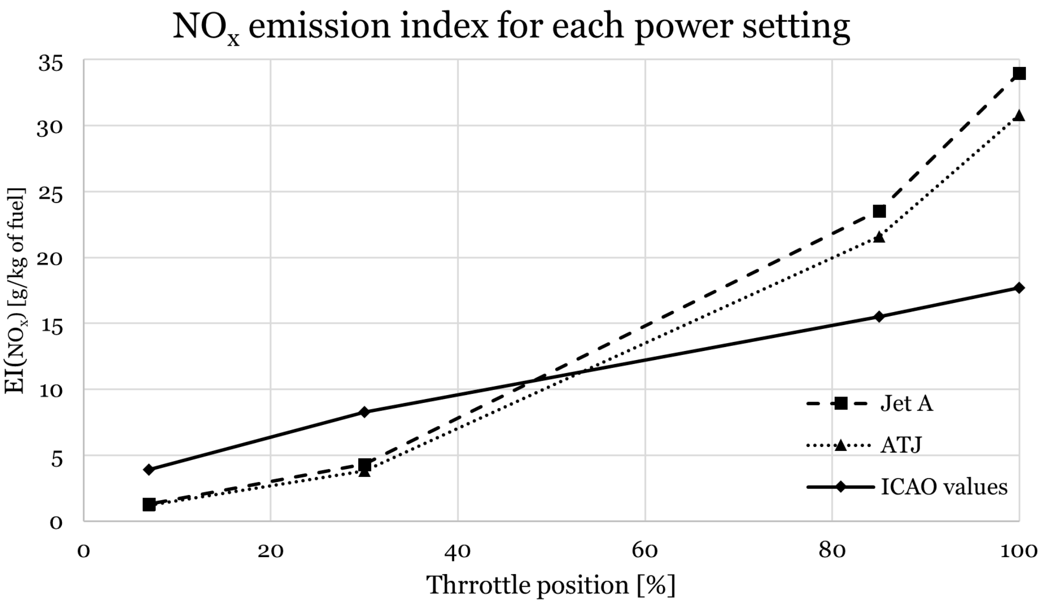

Figure 5.11: Results of NO_x EI for both fuel combustions compared to the NO_x emissions reported by ICAO, for each of the four studied power settings.

First, it is possible to check that, as expected, the results obtained for both fuel combustions follow the correct NO_x emissions trend along the LTO cycle, i.e., with the increase in power, the emissions also increase. This tendency for NO_x emissions to increase with the throttle position happens because this pollutant formation is enhanced at higher temperatures. So in this regard, the results obtained are in agreement with the experimental data. On the other hand, comparing the values for the Jet A combustion (control simulation) with the experimental data, it can be observed that for the two lower power settings the ANSYS Fluent NO_x model underestimated the pollutant emissions and contrary, for the higher power settings, the emissions were overpredicted. The biggest discrepancy for the higher power settings was for the full power condition where the EI obtained through the simulation was approximately 1.9 times higher, while for the underestimated values, the biggest difference was for the 7% power condition where the obtained EI was almost one-third of the experimental value. However, even taking this into account, the results can be considered validated in this regard, since numerically simulated emission results are difficult to match with experimental data, the trend was nevertheless correctly predicted and the results were not very far off from the experimental ones.

With what was mentioned above in mind, a comparison between the NO_x emissions of the two fuel combustions should and must be done. At first look, it is possible to conclude that the alternative studied fuel emits slightly less nitrogen oxides than the conventional one. It can also be observed that the emission indices follow the same pattern for both fuels and although it seems that the difference between the two fuel emissions increases with power, the ratio between the two EI is proportional throughout the whole LTO cycle. Moreover, although one might think, looking at the chart, that the difference in emissions is negligible, it is important to remember that this difference should be scaled up to the effective quantity of fuel that an aircraft carries and burns during a flight since the presented results are for a kilogram of fuel. So it can be concluded that GEVO's ATJ fuel can be a potential alternative fuel for reducing NO_x emissions.

To have a better understanding of where the NO_x is formed inside the chamber, Figure 5.12 presents a contour of the mass fraction of NO_x in the cut-view plane of the rich mixture injector for the ATJ fuel combustion at full power condition.

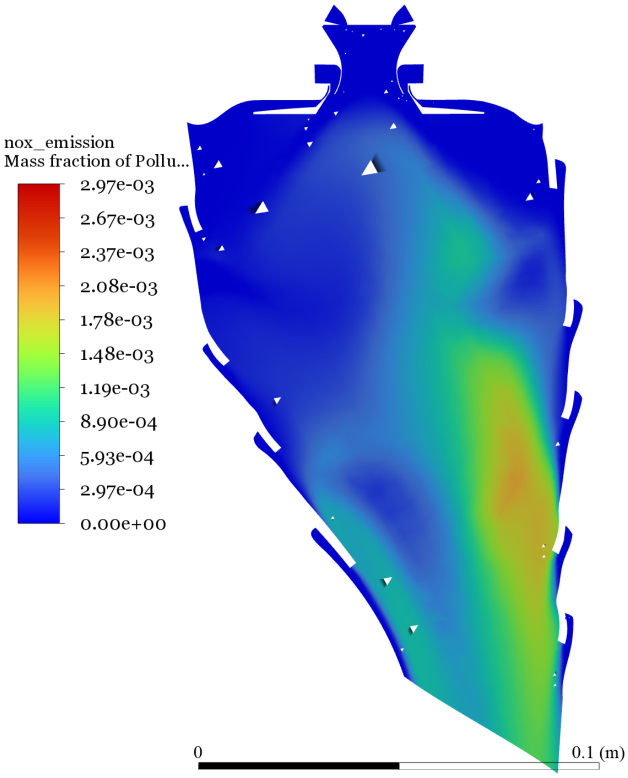

Figure 5.12: Contour of the mass fraction of NO_x at the cut-view plane of the rich fuel injector at the 100% power setting for the ATJ fuel combustion.

It is clear, looking at Figure 5.12, that the majority of NO_x formation occurs in the secondary and dilution zone, probably because these zones are more prone to oxidation.

5.5.2 CO Emissions

Contrary to what happened with the NO_x emission predictions obtained with the simulations, for the CO emissions the results were not satisfactory. In Figure 5.13 the results for this pollutant EIs obtained for both fuel combustions are compared with the ICAO values.

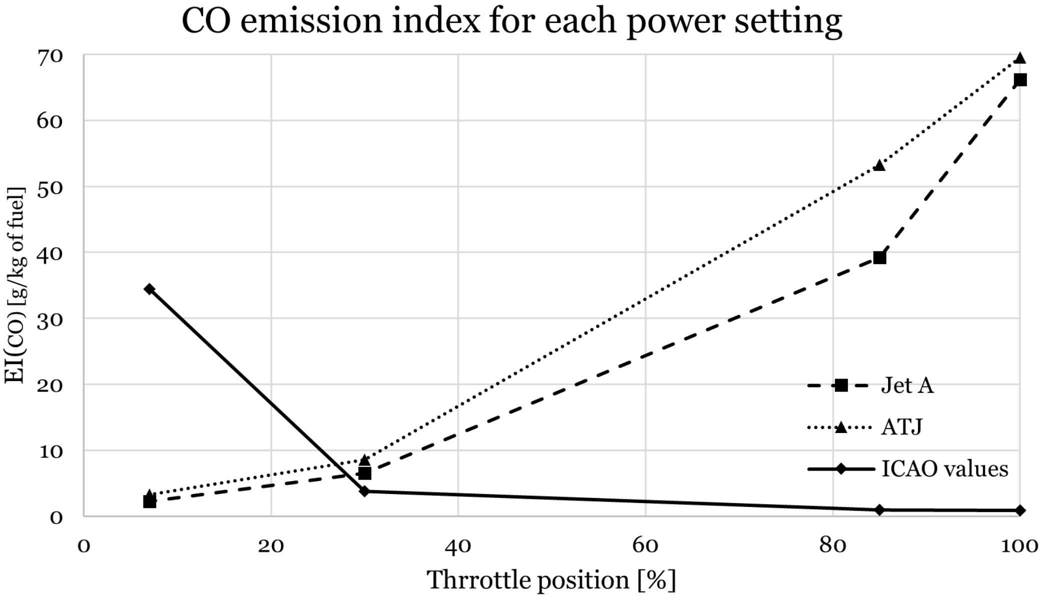

Figure 5.13: Results of CO EI for both fuel combustions compared to the CO emissions reported by ICAO, for each of the four studied power settings.

In this case, it can be observed that the emissions of CO were not correctly predicted. Beyond the fact that the values of the control simulation (Jet A fuel combustion) are very far from the experimental data, especially for the high-power conditions, the tendency of the carbon monoxide along the LTO cycle is wrongly predicted. With the increase in power, the emissions of this pollutant should decrease since the combustion gets more efficient and complete and for both fuel simulations, the inverse is happening. So, the results regarding the CO emission can't be validated and are not reliable. This erroneous prediction is most likely due to the non-modelling of the swirl effect in the air swirlers, as well as the non-modelling of the fuel atomization in the fuel inlets. These promote the mixing of the fuel and enhance combustion efficiency, which would increase CO_2 formation and decrease CO emissions, mainly for high-power conditions. Regarding the comparison between the two fuel combustions, it can be seen that the ATJ fuel produces slightly more carbon monoxide for all power conditions, however, this prediction isn't well-founded and cannot be trusted.

In Figure 5.14 a contour of the mass fraction of CO in the cut-view plane of the rich mixture injector for the ATJ fuel combustion at full power condition is presented. Here, it can be seen that the main concentrations of this pollutant occur in the primary zone and that they decrease in the secondary and dilution zones. This was expected, since, as mentioned in section 2.3.4.4 the carbon monoxide is formed in the primary zone and is oxidized in the secondary zone and transformed into CO_2.

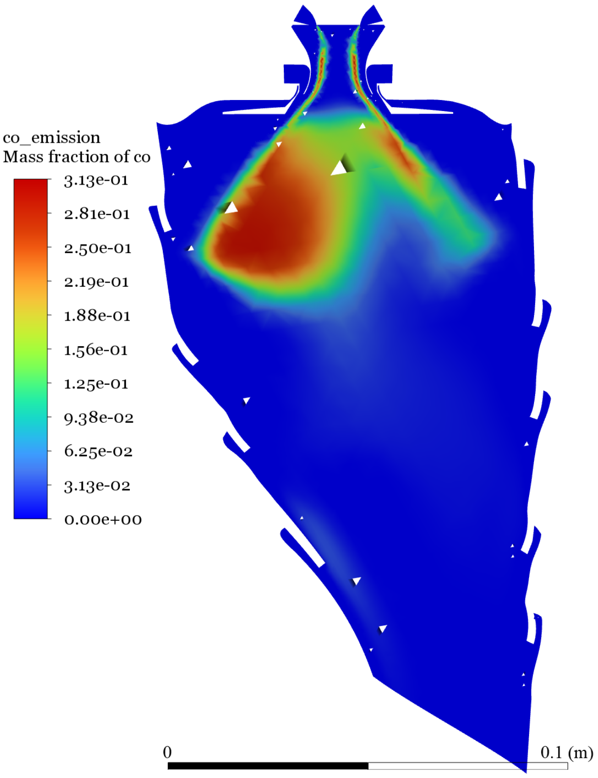

Figure 5.14: Contour of the mass fraction of CO at the cut-view plane of the rich fuel injector at the 100% power setting for the ATJ fuel combustion.

5.5.3 CO_2 Emissions

Finally, CO_2 emission will have a brief analysis. Although no validation of the results can be made since no experimental data was found for the carbon dioxide emissions for the studied engine combustor, it was still decided to present a comparison between the two fuel combustions. It is important to remember that CO_2 is a natural byproduct of complete fuel combustion and so, compared with the previous pollutant emissions analysed, the EIs are much higher in value. Figure 5.15 presents the results obtained for CO_2 EIs for both fuel combustions.

Looking at the chart it can be deduced that the burning of the ATJ fuel has the potential to greatly reduce the amount of CO_2 emitted during combustion. This, paired with the capacity of SAF to reduce CO_2 emissions during their life cycle, can be a game changer in mitigating the negative impact of aviation on climate change. It is, however, important to emphasize that this prediction wasn't validated with experimental data.

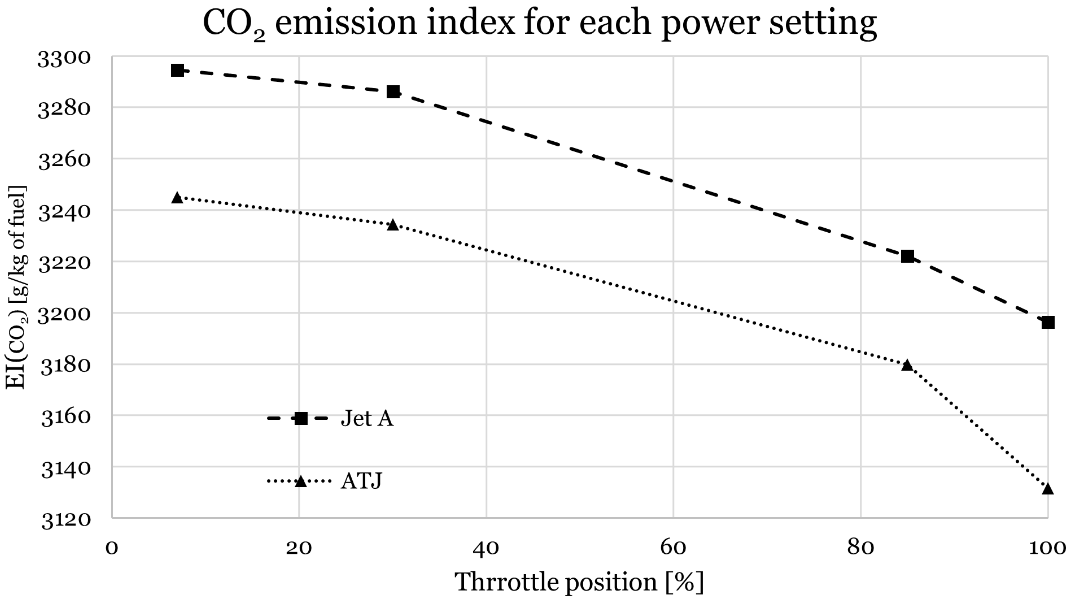

Figure 5.15: Results of CO_2 EI for both fuel combustions for each of the four studied power settings.

Chapter 6

Conclusions and Future Research

6.1 Conclusions

In this master's thesis, a numerical analysis comparing Jet A and ATJ combustion in a CFM56-3 combustor was performed for the four power settings of the ICAO's LTO cycle using the CFD software ANSYS Fluent. This work's main objectives were to correctly model the Jet A fuel combustion inside the combustion chamber and validate the results with available numerical and experimental data. Then, to analyse the pollutant emissions, NO_x, CO and CO_2, produced by the alternative SAF fuel and compare them with the ones resulting from the conventional fuel combustion. Finally, to assess the ATJ fuel's capacity to replace the Jet A fuel in terms of performance parameters, i.e., key parameters inside the chamber, and thus evaluate its drop-in suitability.

In Chapter 1, a brief historical review highlights key efforts made to test and approve the SAF in the aviation industry, while a bibliographical review presents some of the most significant studies regarding the analysis of the emissions, performance and energy conversion of the combustion of alternatives to petroleum-based fuels. After that, Chapter 2 presents fundamental aspects of turbofan engine operation, with a focus on the combustor and its combustion reactions. This way, by providing a clearer understanding of its operating method, the modelling of the combustor was made easier. Chapter 3 discusses the fuels' characteristics and properties and introduces the selected SAF, Gevo's ATJ fuel, used in the simulations for comparison purposes. It was also explained, in this chapter, how difficult it was to find available information regarding the thermodynamic properties of SAF and how this influenced the choice of the alternative fuel.

Chapter 4 presented the most challenging tasks of this study. Here, the methodology followed to obtain the final mesh, boundary conditions, combustion model, turbulence model and the whole problem setup is presented. The importance of all these variables in obtaining satisfactory results was what made it all so demanding. Beyond the inherent difficulty of this type of analysis, the author was initially unfamiliar with the subject, requiring significant time investment to grasp key concepts, especially in combustion thermodynamics, mesh generation, and turbulence and chemistry models. To learn how to handle ANSYS Fluent and Fluent Meshing software was also necessary. Despite these challenges, the experience significantly enhanced the author's knowledge and will be valuable for future endeavours.

Finally, Chapter 5 presents all the results obtained and their consequent discussion. Overall, the outcomes were highly satisfactory. The results obtained for the control simulation, i.e., the Jet A fuel combustion, showed minimal error when analysing the general performance inside the chamber. More specifically, the outlet surface temperature for the full-power condition, compared with the experimental/numerical data from [70], matched perfectly, with an almost negligible error. Additionally, as power varied, the temperature followed the expected trend, and the velocity magnitude vector field was well modelled, accurately capturing the recirculation zone. Regarding the obtained emissions values, which were compared with the experimental data published by ICAO in [48], the results of the NO_x emissions were generally good, however, the same cannot be said from the CO emissions. For the former, the correct variation with power was obtained, i.e., the emissions of NO_x increased with power, as they should. In contrast, CO emissions exhibited an incorrect trend, increasing with power instead of decreasing. This discrepancy could stem from multiple factors, as the study involves numerous variables. However, the author believes the primary causes were the lack of swirl effect modelling in the air swirlers and the absence of fuel atomization modelling at the inlets. Thus, while the results were validated overall, the CO emissions remain an exception, though the model can still be considered satisfactory.

When comparing the two fuels, several observations can be made. First of all, Gevo's ATJ fuel combustion behaviour inside the combustion chamber was very similar to that of conventional fuel. This suggests that for the main studied performance parameters, temperature and velocity, the alternative fuel presented itself as a strong replacement candidate, since for these parameters the values and distributions obtained showed minimal differences. It was even predicted that a possible fuel consumption reduction, obtaining the same performance parameters, can be attained when compared with the Jet A fuel.

In terms of emissions, NO_x results indicated a possible reduction across all power conditions. At full power, a small decrease of 3 grams per kilogram of fuel was predicted, which, when scaled to total fuel consumption over a flight, can make a large difference and help reduce this pollutant emission in the aviation industry. Regarding the CO emissions, and according to simulations, the ATJ fuel combustion may be more polluting. However, since CO predictions for the control case were inaccurate and deemed invalid, this result remains inconclusive. Lastly, CO_2 emissions were also compared between the two fuels, although without experimental data for validation. The findings demonstrated that a potential reduction in this GHG can be attained when using ATJ fuel.

6.2 Future Research

As mentioned several times in the course of this work, combustion is a highly complex process influenced by numerous variables. For that reason, this study could not cover all of these distinct parameters that could improve results. Ergo, future research can build upon this work by focusing on the following aspects:

- Incorporate the modelling of the swirl effect in the air swirlers and fuel atomization in the inlets as it can enhance the mixing inside the chamber and possibly improve emissions results;
- Investigate performance and emissions when using ATJ/Jet A fuel blends (e.g., 25/75, 50/50, and 75/25);
- Conduct a more comprehensive search for the thermodynamic properties of other SAFs and include them in this study;
- Repeat the study with more computationally demanding turbulence models, such as LES or DNS, or adopt a transient approach in an attempt to get better results;
- Combine this study with a complete life cycle assessment of the ATJ fuel to determine its overall advantages over conventional fuels.

Bibliography

[1] M. Klöwer, M. R. Allen, D. S. Lee, S. R. Proud, L. Gallagher, and A. Skowron, "Quantifying aviation's contribution to global warming," *Environmental Research Letters*, vol. 16, 10 2021. 1

[2] M. Prussi, U. Lee, M. Wang, R. Malina, H. Valin, F. Taheripour, C. Velarde, M. D. Staples, L. Lonza, and J. I. Hileman, "CORSIA: The first internationally adopted approach to calculate life-cycle GHG emissions for aviation fuels," *Renewable and Sustainable Energy Reviews*, vol. 150, 10 2021. 1, 2

[3] "Sustainable aviation fuel," [Accessed: March 2, 2024]. [Online]. Available: https://afdc.energy.gov/fuels/sustainable_aviation_fuel.html 1, 2, 4, 53

[4] H. Ritchie, "Climate change and flying: what share of global CO2 emissions come from aviation?" *Our World in Data*, 2020. [Online]. Available: https://ourworldindata.org/co2-emissions-from-aviation 1

[5] D. S. Lee, D. W. Fahey, A. Skowron, M. R. Allen, U. Burkhardt, Q. Chen, S. J. Doherty, S. Freeman, P. M. Forster, J. Fuglestvedt, A. Gettelman, R. R. D. León, L. L. Lim, M. T. Lund, R. J. Millar, B. Owen, J. E. Penner, G. Pitari, M. J. Prather, R. Sausen, and L. J. Wilcox, "The contribution of global aviation to anthropogenic climate forcing for 2000 to 2018," *Atmospheric Environment*, vol. 244, 1 2021. 1

[6] International Air Transport Association, "Net-zero carbon emissions by 2050," 10 2021, [Accessed: March 6, 2024]. [Online]. Available: https://www.iata.org/en/pressroom/pressroom-archive/2021-releases/2021-10-04-03/ 2

[7] A. Bauen, N. Bitossi, L. German, A. Harris, and K. Leow, "Sustainable aviation fuels status, challenges and prospects of drop-in liquid fuels, hydrogen and electrification in aviation," *Johnson Matthey Technology Review*, vol. 64, pp. 263–278, 7 2020. 2, 54, 55

[8] "What are sustainable aviation fuels?" [Accessed: March 12, 2024]. [Online]. Available: https://www.easa.europa.eu/eco/eaer/topics/sustainable-aviation-fuels/what-are-sustainable-aviation-fuels 2

[9] J. M. P. de Oliveira, "CFD analysis of the combustion of bio-derived fuels in the CFM56-3 combustor," Master's thesis, Universidade da Beira Interior, Covilhã, Portugal, 2016. 3, 33, 57, 61, 72, 73, 78, 82, 89

[10] E. Cabrera and J. M. M. de Sousa, "Use of sustainable fuels in aviation—a review," *Energies*, vol. 15, 4 2022. 3, 4, 5, 50, 52, 53

[11] S. Zuckerman, "Toward sustainable aviation fuels," 2015. [Online]. Available: www.climatesolutions.org 4

[12] S. R. Schill, "KLM tests bio-jet fuel with passengers on board," 11 2009, [Accessed: March 22, 2024]. [Online]. Available: https://biodieselmagazine.com/articles/klm-tests-bio-jet-fuel-with-passengers-on-board-3883 4

[13] "Aviation biofuel demonstrations," [Accessed: March 22, 2024]. [Online]. Available: https://en.wikipedia.org/wiki/Aviation_biofuel_demonstrations 4

[14] I. Richards, "United airlines operates commercial flight on 100% saf in 1 engine," 12 2021, [Accessed: March 28, 2024]. [Online]. Available: https://worldofaviation.com/2021/12/united-airlines-operates-commercial-flight-on-100-saf-in-1-engine/ 5

[15] Virgin Atlantic, "Virgin atlantic flies world's first 100% sustainable aviation fuel flight from london heathrow to new york JFK," 11 2023, [Accessed: March 28, 2024]. [Online]. Available: https://corporate.virginatlantic.com/gb/en/media/press-releases/worlds-first-sustainable-aviation-fuel-flight.html 6

[16] K. French, "Recycled fuel performance in the SR-30 gas turbine," in *ASEE Annual Conference Proceedings*, 2003. 6

[17] E. Corporan, M. J. DeWitt, V. Belovich, R. Pawlik, A. C. Lynch, J. R. Gord, and T. R. Meyer, "Emissions characteristics of a turbine engine and research combustor burning a Fischer-Tropsch jet fuel," *Energy and Fuels*, vol. 21, pp. 2615–2626, 9 2007. 6

[18] Z. Habib, R. Parthasarathy, and S. Gollahalli, "Performance and emission characteristics of biofuel in a small-scale gas turbine engine," *Applied Energy*, vol. 87, pp. 1701–1709, 2010. 6

[19] M. T. Timko, S. C. Herndon, E. D. L. R. Blanco, E. C. Wood, Z. Yu, R. C. Miake-Lye, W. B. Knighton, L. Shafer, M. J. Dewitt, and E. Corporan, "Combustion products of petroleum jet fuel, a Fischer-Tropsch synthetic fuel, and a biomass fatty acid methyl ester fuel for a gas turbine engine," *Combustion Science and Technology*, vol. 183, pp. 1039–1068, 10 2011. 7

[20] P. Lobo, D. E. Hagen, and P. D. Whitefield, "Comparison of PM emissions from a commercial jet engine burning conventional, biomass, and Fischer-Tropsch Fuels," *Environmental Science and Technology*, vol. 45, pp. 10 744–10 749, 12 2011. 7

[21] P. Lobo, L. Rye, P. I. Williams, S. Christie, I. Uryga-Bugajska, C. W. Wilson, D. E. Hagen, P. D. Whitefield, S. Blakey, H. Coe, D. Raper, and M. Pourkashanian, "Impact of alternative fuels on emissions characteristics of a gas turbine engine - part 1: Gaseous and particulate matter emissions," *Environmental Science and Technology*, vol. 46, pp. 10 805–10 811, 10 2012. 7

[22] A. R. A. Talib, E. Gires, and M. T. Ahmad, “Performance evaluation of a small-scale turbojet engine running on palm oil biodiesel blends,” *Journal of Fuels*, vol. 2014, pp. 1–9, 7 2014. 8

[23] T. Schripp, F. Herrmann, P. Oßwald, M. Köhler, A. Zschocke, D. Weigelt, M. Mroch, and C. Werner-Spatz, “Particle emissions of two unblended alternative jet fuels in a full scale jet engine,” *Fuel*, vol. 256, 11 2019. 8

[24] T. Schripp, B. E. Anderson, U. Bauder, B. Rauch, J. C. Corbin, G. J. Smallwood, P. Lobo, E. C. Crosbie, M. A. Shook, R. C. Miake-Lye, Z. Yu, A. Freedman, P. D. Whitefield, C. E. Robinson, S. L. Achterberg, M. Köhler, P. Oßwald, T. Grein, D. Sauer, C. Voigt, H. Schlager, and P. LeClercq, “Aircraft engine particulate matter emissions from sustainable aviation fuels: Results from ground-based measurements during the NASA/DLR campaign ECLIF2/ND-MAX,” *Fuel*, vol. 325, 10 2022. 8

[25] Y. Kroyan, M. Wojcieszyk, O. Kaario, and M. Larmi, “Modeling the impact of sustainable aviation fuel properties on end-use performance and emissions in aircraft jet engines,” *Energy*, vol. 255, 9 2022. 8

[26] Rolls-Royce, *The Jet Engine*, 5th ed. Derby, England: Rolls-Royce plc, 1996. 11, 12, 13, 14, 15, 16, 17, 18, 19, 20, 23, 24, 25, 35, 36, 38

[27] M. L. Mathur and R. P. Sharma, *Gas Turbines and Jet and Rocket Propulsion*, 2nd ed. Delhi, India: Standard Publishers Distributors, 2007. 11, 15, 16, 19, 20, 21, 22, 23, 24, 25, 33, 36, 37, 38, 39, 47

[28] “How does a jet engine work?” 5 2021, [Accessed: June 6, 2024]. [Online]. Available: https://www.grc.nasa.gov/www/k-12/UEET/StudentSite/engines.html 11

[29] K. Hünecke, *Jet Engines: Fundamentals of Theory, Design, and Operation*, 6th ed. Osceola, WI, USA: Motorbooks International Publishers and Wholesalers, 2003. 11, 12, 13, 14, 15, 17, 18, 19, 20, 23, 24

[30] “Ideal brayton cycle,” 5 2021, [Accessed: June 12, 2024]. [Online]. Available: https://www.grc.nasa.gov/www/k-12/airplane/brayton.html 12

[31] “Inlets,” 5 2021, [Accessed: June 13, 2024]. [Online]. Available: https://www.grc.nasa.gov/www/k-12/airplane/inlet.html 13, 14

[32] “Compressors,” 5 2021, [Accessed: June 18, 2024]. [Online]. Available: https://www.grc.nasa.gov/www/k-12/airplane/compress.html 14, 15, 16

[33] “Power turbine,” 5 2021, [Accessed: June 21, 2024]. [Online]. Available: https://www.grc.nasa.gov/www/k-12/airplane/powturb.html 18, 19

[34] S. Samuelsen, "Conventional type combustion," in *The Gas Turbine Handbook*. Morgantown, WV, USA: National Energy Technology Laboratory, 2006. 20, 25, 26, 27, 28, 29

[35] A. H. Lefebvre and D. R. Ballal, *Gas Turbine Combustion: Alternative Fuels and Emissions*, 3rd ed. Boca Raton, FL, USA: CRC Press, 2010. 20, 21, 22, 23, 24, 25, 26, 27, 28, 29, 30, 31, 32, 33, 34, 35, 36, 37, 38, 39, 40, 42, 44

[36] H. Cohen, G. F. C. Rogers, and H. I. H. Saravanamuttoo, *Gas Turbine Theory*, 4th ed. Essex, England: Longman Group Limited, 1996. 20, 24, 37, 38, 39, 47, 48

[37] CFM International, "CFM56-3 training manual - general engine data," 10 1995. 29, 30, 34, 39

[38] CFM International, "CFM56-3 training manual - borescope inspection," 9 2003. 29, 30, 31

[39] R. S. Domingues, "CFD analysis of the combustion of hydrogen fuel on a CFM56-3 combustor," Master's thesis, Universidade da Beira Interior, Covilhã, Portugal, 2022. 29, 61, 69, 72, 73, 74, 77, 78, 82, 89

[40] S. R. Turns, *An Introduction To Combustion: Concepts and Applications*, 2nd ed. New York, USA: McGraw-Hill, 2000. 39, 40, 41, 42, 43, 44

[41] A. M. Mellor, *Design of Modern Turbine Combustors*. London, England: Academic Press, 1990. 40, 41

[42] M. Lackner, F. Winter, and A. K. Agarwal, *Handbook of Combustion - Volume 3: Gaseous and Liquid Fuels*. Weinheim, Germany: Wiley-VCH, 2010, vol. 3. 40, 58

[43] K. K. Kuo, *Principles of Combustion*, 2nd ed. Hoboken, NJ, USA: John Wiley & Sons, 2005. 41, 42, 43, 44, 57, 58

[44] N. Peters, "Combustion theory," CEFRC Summer School, Princeton, 2010. 41

[45] R. C. Flagan and J. H. Seinfeld, *Fundamentals of Air Pollution Engineering*. Englewood Cliffs, NJ, USA: Prentice-Hall, Inc, 1988. 42, 43

[46] *Annex 16: Environmental Protection: Volume II - Aircraft Engine Emissions*, 3rd ed. International Civil Aviation Organization, 7 2008, vol. II. 44, 45

[47] ICAO Secretariat, "ICAO standards and recommended practices: Annex 16, volume II." 46

[48] ICAO, "ICAO aircraft engine emission databank (EEDB)," 7 2024. 46, 69, 73, 77, 81, 90, 98

[49] "Alternative jet fuels - a supplement to chevron's aviation fuels technical review," Chevron Corporation, 2006. 49

[50] H. Wei, W. Liu, X. Chen, Q. Yang, J. Li, and H. Chen, “Renewable bio-jet fuel production for aviation: A review,” *Fuel*, vol. 254, 10 2019. 49, 50, 53, 54

[51] S. S. Doliente, A. Narayan, J. F. D. Tapia, N. J. Samsatli, Y. Zhao, and S. Samsatli, “Bio-aviation fuel: A comprehensive review and analysis of the supply chain components,” *Frontiers in Energy Research*, vol. 8, 7 2020. 49, 50, 52, 54, 55

[52] G. Velidi, “Alternative fuels for aviation gas turbine engines: Review on its progress,” in *AIP Conference Proceedings*, vol. 2655. American Institute of Physics Inc., 5 2023. 49

[53] “The best product for military use,” [Accessed: September 24, 2024]. [Online]. Available: https://www.repsol.com/en/products-and-services/aviation/jp-8/index.cshtml 49

[54] “Military jet fuel,” [Accessed: September 24, 2024]. [Online]. Available: https://www.shell.com/business-customers/aviation/aviation-fuel/military-jet-fuel-grades.html 49

[55] O. R. Calderon, L. Tao, Z. Abdullah, K. Moriarty, S. Smolinski, A. Milbrandt, M. Talmadge, A. Bhatt, Y. Zhang, V. Ravi, C. Skangos, E. Tan, and C. Payne, “Sustainable aviation fuel (SAF) state-of-industry report: State of SAF production process,” National Renewable Energy Laboratory, 7 2024. 50

[56] R. Xu, H. Wang, M. Colket, and T. Edwards, “Thermochemical properties of jet fuels,” Stanford University, 7 2015. 52, 53

[57] R. J. Kee, F. M. Rupley, and J. A. Miller, “Chemkin-II: A fortran chemical kinetics package for the analysis of gas-phase chemical kinetics,” Sandia National Lab., Livermore, CA, USA, 9 1989. 53

[58] “National alternative jet fuels test database,” [Accessed: October 21, 2024]. [Online]. Available: https://altjetfuels.illinois.edu/ 53

[59] “Low-carbon, bio-based sustainable aviation fuel,” [Accessed: October 21, 2024]. [Online]. Available: https://gevo.com/product/sustainable-aviation-fuel/ 53

[60] “Sustainable aviation fuel whitepaper,” Gevo, Inc., 2022. 53

[61] “Company information,” [Accessed: October 25, 2024]. [Online]. Available: https://www.ansys.com/company-information 57

[62] “Ansys fluent,” [Accessed: October 25, 2024]. [Online]. Available: https://www.ansys.com/products/fluids/ansys-fluent 57

[63] H. Mongia, S. Krishnaswami, and P. Sreedhar, “Comprehensive gas turbine combustion modeling methodology,” in *International Aerospace CFD Conference*, Paris, France, 6 2007. 58

[64] L. Jiang, “RANS modelling of turbulence in combustors,” in *Turbulence Modelling Approaches*. InTech, 7 2017, ch. 7. 59

[65] *Ansys Fluent Theory Guide*. ANSYS, Inc., 7 2021. 59, 60, 61, 76, 78

[66] *Ansys Fluent User’s Guide*. ANSYS, Inc., 11 2010. 59, 60, 75, 76, 77, 78

[67] A. Bakker, “Lectures on applied computational fluid dynamics,” 2008. [Online]. Available: www.bakker.org. 60

[68] “5 best practices for gas turbine combustion meshing using ansys fluent,” ANSYS, Inc., 2020. 65, 66, 68, 70

[69] J. W. Slater, “Examining spatial (grid) convergence,” 2 2021, [Accessed: January 29, 2025]. [Online]. Available: https://www.grc.nasa.gov/WWW/wind/valid/tutorial/spatconv.html 65

[70] P. M. A. Ribeiro, “Análise de performance da família de motores de avião CFM56,” Master’s thesis, Instituto Superior de Engenharia de Lisboa, Lisboa, Portugal, 2012. 69, 70, 72, 73, 81, 88, 98

[71] “Lecture 7: Mesh quality & advanced topics,” ANSYS, Inc., 2 2015. 70, 71

[72] I. I. A. C. Morão, “The influence of jet fuels on the emission of pollutants,” Master’s thesis, Universidade da Beira Interior, Covilhã, Portugal, 2019. 72

[73] R. Smith and et al., “Advanced low emissions subsonic combustor study - final report,” Cleveland, OH, USA, 12 1998. 73

Appendix A

Thermodynamic Properties of Gevo ATJ in CHEMKIN Format

```
POSF11498         S07/15C  13H  28    0   0 G   298.000  3000.000              1
 0.33643040E+02 0.67928091E-01-0.20546000E-04 0.24969564E-08-0.69632051E-13    2
-0.58361672E+05-0.14804048E+03 0.42177753E+01 0.93084201E-01 0.80710743E-04    3
-0.17453084E-06 0.79970509E-10-0.47017836E+05 0.18436749E+02                   4
```

Appendix B

Results

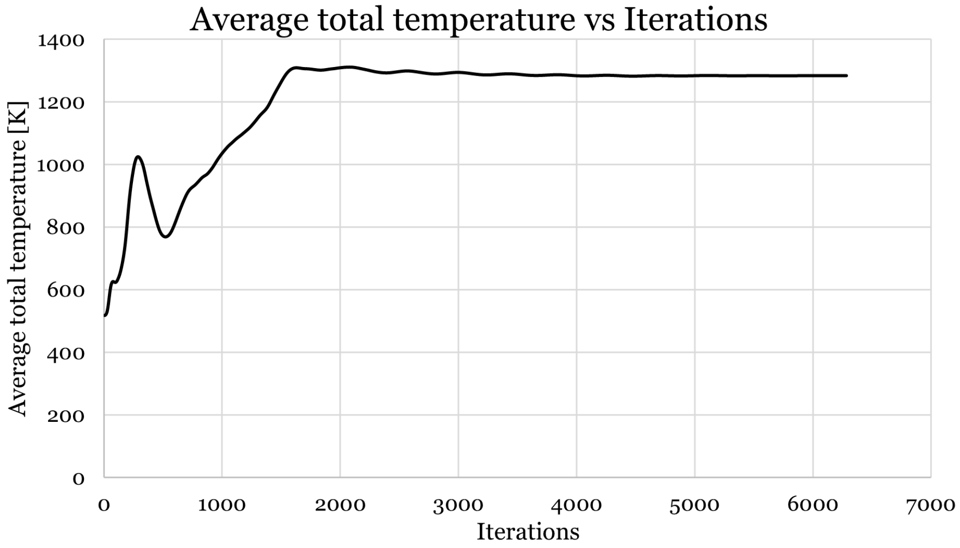

Figure B.1: Plot of the average total temperature in the fluid volume for the ATJ combustion simulation at the 30% power setting.

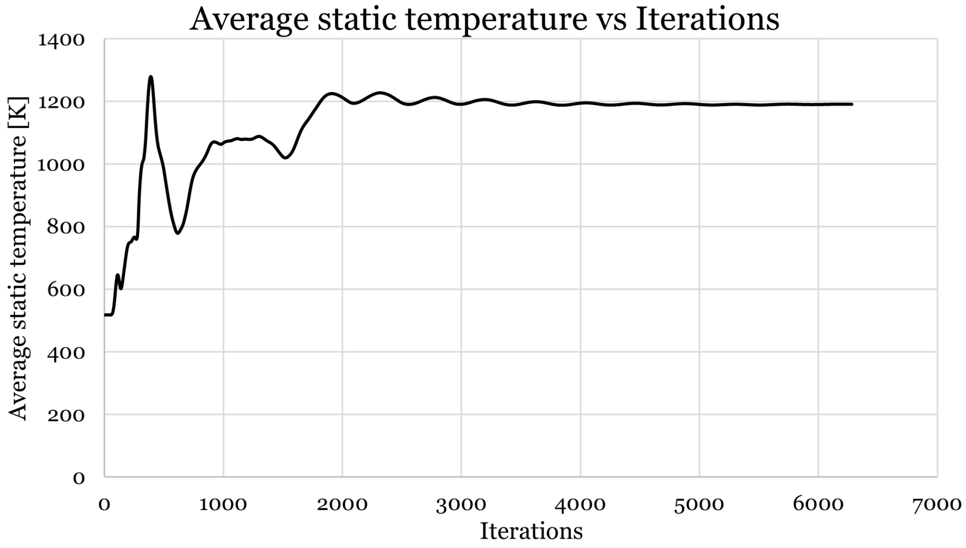

Figure B.2: Plot of the average static temperature in the outlet of the combustion chamber for the ATJ combustion simulation at the 30% power setting.

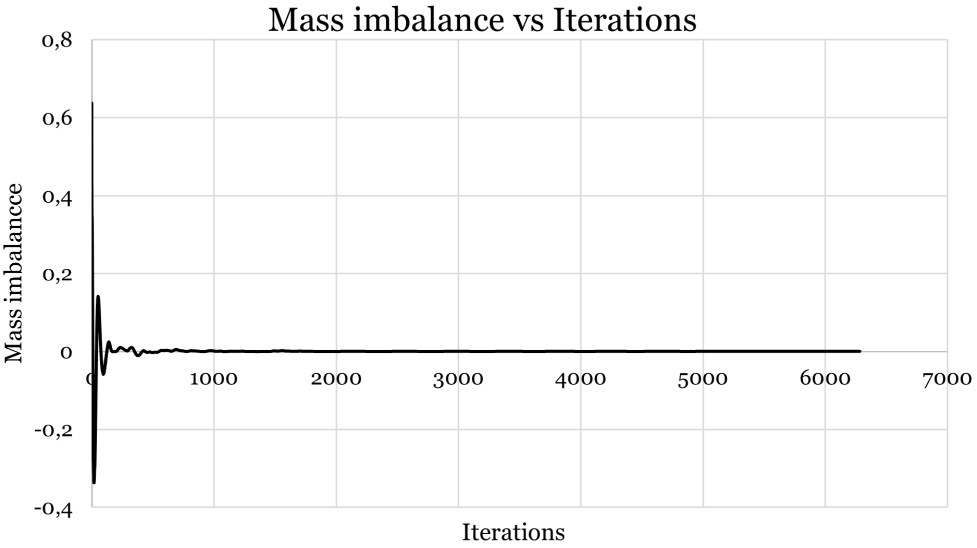

Figure B.3: Plot of the mass imbalance for the ATJ combustion simulation at the 30% power setting.

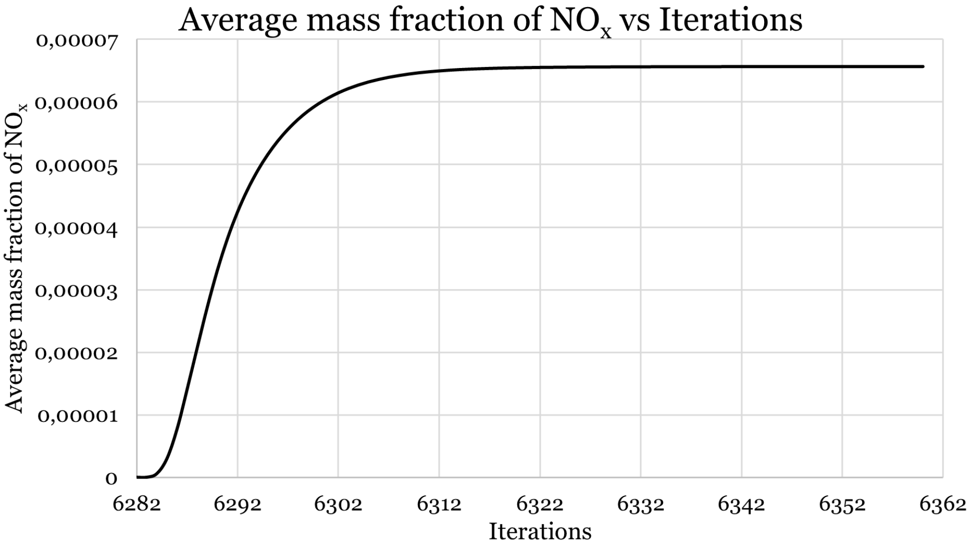

Figure B.4: Plot of the average mass fraction of NO_x in the outlet of the combustion chamber for the ATJ combustion simulation at the 30% power setting.